

AD A 040319

AD 148:
DDC FILE COPY

FINAL TECHNICAL REPORT

12
B.S.

**RAPID-SCAN ANTENNA STUDY FOR
NAVAL SHORT-RANGE SELF-DEFENSE
MISSILE SYSTEM**

EES/GIT Project A-1794

By

J. W. Cofer, Jr., R. M. Goodman, Jr., and L. D. Sikes

Prepared for

**APPLIED PHYSICS LABORATORY
THE JOHNS HOPKINS UNIVERSITY
JOHNS HOPKINS ROAD
LAUREL, MARYLAND 20810**

Under

APL/JHU Subcontract 600444

DDC
JUN 8 1977
C

April 1976

1976



**ENGINEERING EXPERIMENT STATION
Georgia Institute of Technology
Atlanta, Georgia 30332**

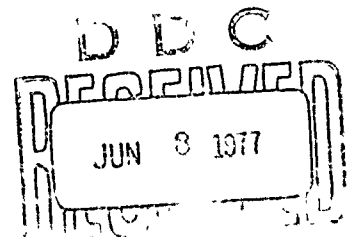
ENGINEERING EXPERIMENT STATION
Georgia Institute of Technology
Atlanta, Georgia 30332

(6) RAPID-SCAN ANTENNA STUDY FOR NAVAL SHORT-RANGE
SELF-DEFENSE MISSILE SYSTEM

(9) Final Technical Report on Nov 75 - Apr 76,
EES/GIT Project A-1794

By
(10) J. W. Cofer, Jr., R. M. Goodman, Jr. and L. D. Sikes

Prepared for
APPLIED PHYSICS LABORATORY
THE JOHNS HOPKINS UNIVERSITY
Johns Hopkins Road
Laurel, Maryland 20310



Under
Prime Contract N00017-72-C-4401

(15) and

APL/JHU Subcontract 600444

(11) April 1976

(12) 148 p.

ACCESSION	
NTIS	White Section <input checked="" type="checkbox"/>
DEC	Bull Section <input type="checkbox"/>
UNANNOUNCED	
JUSTIFICATION	
BY	
DISTRIBUTION/AVAILABILITY CODES	
Dist.	Avail. and of SPECIAL
A	

Approved for public release;
distribution

031 650

mt

ABSTRACT

Under APL/JHU Subcontract 600444, the Engineering Experiment Station at the Georgia Institute of Technology performed a conceptual study of millimeter-wave scanning antennas which might be applicable to the acquisition problem of a naval point defense system. The study covered such related areas as: component availability; increased antenna requirements due to multipath, atmospheric absorption, and rain attenuation; and scan speed and format needed to acquire the targets of interest. Gain requirements were derived on the basis of acceptable signal-to-noise ratios at the desired range using commercially available power sources. Performance degradation due to rainfall was calculated at several frequencies between 9.3 and 95 GHz. 46 GHz was chosen as the operating frequency due to antenna size and signal-to-noise ratio. Several scanning antenna techniques including frequency scanning, electronic phased arrays, multiple beam forming networks, electromechanical techniques and several hybrid approaches were considered. An electromechanical technique utilizing a geodesic lens, line source feed, parabolic cylinder, and nodding planar splash plate was chosen as the optimum candidate due to the factors of component availability, cost, scan speed, and frequency of operation.

ACKNOWLEDGEMENTS

The successful execution of this study program was made possible through the combined efforts of numerous persons at both the Applied Physics Laboratory and the Engineering Experiment Station (EES) at the Georgia Institute of Technology. In particular, the authors gratefully acknowledge the efforts of Messrs. C. A. Young and O. M. Martin of APL for providing program direction, and of the following Georgia Tech personnel: Dr. E. K. Reedy for serving as Division Chief and for contributing to the signal-to-noise ratio calculations; Dr. J. E. Rhodes, Jr. for his inputs concerning the overall nature of the tracking and acquisition systems; Dr. R. D. Hayes for consultation on the atmospheric and precipitation calculations; Mr. R. C. Rogers for actually performing these calculations; Mr. T. S. Craven for his inputs concerning frequency scanning; and Mr. C. E. Summers for handling all multipath calculations. The efforts of Mrs. A. M. Evans are especially appreciated in the typing of the manuscript.

TABLE OF CONTENTS

	<u>Page</u>
I. INTRODUCTION	1
II. COMPONENT SURVEY	5
III. ENVIRONMENTAL FACTORS	13
A. Multipath Analysis	13
B. Atmospheric Attenuation	30
C. Rain and Fog Attenuation	36
IV. SYSTEM CALCULATIONS	43
A. Target Characteristics	43
B. Tracking Considerations	46
1. Track Schemes	46
2. Minimum Track Lock-on Range	48
3. Track System Signal-To-Noise Ratio	52
C. Acquisition Volume	57
1. Acquisition Range	57
2. Acquisition Signal-To-Noise Ratio	58
V. CANDIDATE ANTENNA CONCEPTS	69
A. Frequency Scanning	69
1. Continuous Slotted Circular Waveguide	69
2. Continuous Slotted Rectangular Waveguide	73
3. Discrete Slots In Rectangular Waveguide	77
4. Frequency Scanning System Considerations	79
B. Electronic Phased Arrays	81
C. Multiple Beam Forming Network	90

	<u>Page</u>
V.	
D. Rotman Lens	100
E. Geodesic Luneberg Lens	109
F. Rockwell Ferrite Scanner	118
G. Other Electromechanical Techniques	118
VI. CONCLUSIONS AND RECOMMENDATIONS	123
VII. REFERENCES.	131

LIST OF FIGURES

<u>Figure</u>	<u>Page</u>
1. Typical short-range, self-defense scenario illustrating large target, incoming airborne attack vehicles, and radar coverage sector	2
2. Geometric parameters used in the calculation of multipath interference	14
3. Calculated rf (9.3 GHz) power incident on a target located 50 ft. above the surface of the sea (rms roughness indicated) shown as a function of horizontal range	18
4. Calculated rf (16.5 GHz) power incident on a target located 50 ft. above the surface of the sea (rms roughness indicated) shown as a function of horizontal range	19
5. Calculated rf (23 GHz) power incident on a target located 50 ft. above the surface of the sea (rms roughness indicated) shown as a function of horizontal range	20
6. Calculated rf (35 GHz) power incident on a target located 50 ft. above the surface of the sea (rms roughness indicated) shown as a function of horizontal range	21
7. Calculated rf (46 GHz) power incident on a target located 50 ft. above the surface of the sea (rms roughness indicated) shown as a function of horizontal range	22
8. Calculated rf (70 GHz) power incident on a target located 50 ft. above the surface of the sea (rms roughness indicated) shown as a function of horizontal range	23
9. Calculated rf (95 GHz) power incident on a target located 50 ft. above the surface of the sea (rms roughness indicated) shown as a function of horizontal range	24
10. Calculated rf (9.3 GHz) power incident on a target located 50 ft. above the surface of the sea (rms roughness indicated) shown as a function of horizontal range	25
11. Calculated rf (23 GHz) power incident on a target located 50 ft. above the surface of the sea (rms roughness indicated) shown as a function of horizontal range	26
12. Calculated rf (95 GHz) power incident on a target located 50 ft. above the surface of the sea (rms roughness indicated) shown as a function of horizontal range	27

List of Figures continued

<u>Figure</u>	<u>Page</u>
13. Calculated rf (23 GHz) power incident on a target located 100 ft. above the surface of the sea (rms roughness indicated) shown as a function of horizontal range	28
14. Calculated rf (23 GHz) power incident on a target located 500 ft. above the surface of the sea (rms roughness indicated) shown as a function of horizontal range	29
15. Pressure broadening of the attenuation characteristics of a single water line and a pair of oxygen lines.	32
16. Total atmospheric absorption due to water vapor alone (dashed) and oxygen only (solid)	37
17. Total atmospheric attenuation due to both water and oxygen for several different relative humidities	38
18. Calculated (by Goldstein) attenuation of electromagnetic energy by rain and fog presented as a function of wavelength.	40
19. Typical threat trajectories	44
20. Geometry of target trajectories	45
21. Solid angular window filled with discrete overlapping beams	47
22. Geometry of point defense missile intercepting threat vehicles.	47
23. Calculated required lock-on range as a function of intercept range for the threat velocities and missile warm up times shown	51
24. Four pairs of orthogonally scanning fan beams which collectively cover a 45° by 45° sector.	55
25. Calculated acquisition range required to obtain the indicated pulses per beamwidth (N_p) and scan observations (N_s) as a function of beamwidth for three different target velocities	59
26. Required gain as a function of range to produce a 12 -dB signal-to-noise ratio from a radar operating at 9.3 GHz for the cases of clear day and 4 mm/hr of rain.	62

List of Figures continued

<u>Figure</u>	<u>Page</u>
27. Required gain as a function of range to produce a 12 -dB signal-to-noise ratio from a radar operating at 16.5 GHz for the cases of a clear day and 4 mm/hr of rain.	63
28. Required gain as a function of range to produce a 12 -dB signal-to-noise ratio from a radar operating at 23 GHz for the cases of a clear day and 4 mm/hr of rain.	64
29. Required gain as a function of range to produce a 12 -dB signal-to-noise ratio from a radar operating at 35 GHz for the cases of a clear day and 4 mm/hr of rain.	65
30. Required gain as a function of range to produce a 12 -dB signal-to-noise ratio from a radar operating at 46 GHz for the cases of a clear day and 4 mm/hr of rain.	66
31. Required gain as a function of range to produce a 12 -db signal-to-noise ratio from a radar operating at 70 GHz for the cases of a clear day and 4 mm/hr of rain.	67
32. Required gain as a function of range to produce a 12 -dB signal-to-noise ratio from a radar operating at 95 GHz for the cases of a clear day and 4 mm/hr of rain.	68
33. Conceptual diagram of four frequency scannable slot-type radiators	70
34. Planar array composed of vertical stack of slotted waveguides.	71
35. Calculated beam pointing angle as a function of frequency for a circular waveguide (WC 38) with the continuous axial slots shown	74
36. Calculated beam pointing angles for radiation from rectangular WR-28 and WR-42 waveguide with continuous slot in narrow wall	75
37. Calculated main beam pointing directions for the three different continuously slotted waveguides (zero slot width) shown.	76

List of Figures continued

<u>Figure</u>	<u>Page</u>
38. Calculated mainbeam pointing angle as a function of frequency for an array of resonant (23 GHz) slots in the broadwall of a serpentine waveguide.	78
39. Block diagram of radar system which transmits a number of discrete frequencies with each corresponding to a unique beam pointing angle.	80
40. (a) Array of discrete beam positions and (b) array of open-end waveguides containing irises.	82
41. Corporate power division network	87
42. Five-way power divider	88
43. Seven-way power divider.	88
44. Conceptual diagram of space-fed array.	89
45. Simplified diagram of two-dimensional pencil-beam scanner utilizing electronic scanning in azimuth and mechanical deflection in elevation.	91
46. Multiple beam forming matrix for planar array.	93
47. Simplified conceptual diagram of Butler matrix beam forming network.	94
48. Simplified diagram of technique for interfacing 2^n outputs to a larger number of radiating elements	93
49. Network components for producing cosine aperture illumination	96
50. Simplified diagram of Rotman lens geometry	101
51. Rotman lens with electronic switch network for connecting a single transmitter/receiver to each beam port.	104
52. Rotman lens which forms multiple beams on transmit	106
53. Rotman lens with individual sources for each lens input.	107
54. Simplified diagram of Rotman lens fed by ring switch	108

List of Figures continued

<u>Figure</u>	<u>Page</u>
55. Section through the center of a geodesic lens illustrating three generic input schemes and their designations.	110
56. Top view of a geodesic lens showing the ray paths when the feedhorn is displaced by angle θ from the center of the lens feedsector	112
57. Typical multi-port ring switch used for rapidly scanning a geodesic lens	112
58. Exploded view of rapid scanning antenna system incorporating geodesic lens, line source horn, and cylindrical reflector. .	113
59. Armored personnel carrier with rapid scan geodesic lens antenna system showing two positions of lens boresight in its 360° sector.	114
60. Central section through folded geodesic lens antenna system in 70 - GHz rapid scan radar	115
61. Simplified diagram of Rockwell ferrite scanner.	119
62. Progressive assembly levels for a typical waveguide organ-pipe scanner.	121
63. Three views of two dimensional scanner utilizing electro-mechanical scan in azimuth and frequency scan in elevation. .	122
64. Calculated signal-to-noise ratio at the receiver for a 46 GHz radar illuminating a 1 square meter target at the range indicated	126
65. Recommended scanning antenna concept	129

LIST OF TABLES

<u>Table</u>	<u>Page</u>
I. Transition Frequencies for Oxygen Absorption.	33
II. Water Vapor Absorption Frequencies and Associated Data. . . .	33
III. Calculated Atmospheric Attenuation for 50% Relative Humidity and a Number of Typical Frequencies.	36
IV. Comparison of Theoretical and Measured Rainfall Attenuation as a Function of Frequency.	42
V. Time History of Elevation Location of Target in Vertical Climb and Raster Scanning Pencil Beam	49
VI. Calculated Signal-to-Noise Ratio at 23 GHz for Antenna Gain of 29.3 dB	54
VII. Calculated Signal-to-Noise Ratio at 46 GHz for Antenna Gains of 32.3 dB and 35.3 dB.	56
VIII. System Parameters used in Calculation of Antenna Gain Requirements.	61
IX. Calculated Aperture Dimensions for a Two Dimensional Scanner as a Function of Frequency, Beamwidth, and Gain . . .	117

I. INTRODUCTION

Under Navy Prime Contract N00017-72-C-4401, the Applied Physics Laboratory (APL) of The Johns Hopkins University was tasked to perform conceptual design studies for a short-range, self-defense, missile system for use on naval vessels. The proposed system was to use a radar sensor for acquisition and tracking of threat airborne vehicles which might approach the naval vessel as shown in Figure 1. A missile would then be fired from the vessel and guided to intercept the threat. Operation at millimeter wavelength frequencies having "appropriate" electromagnetic absorption has been suggested as a measure of protection against standoff jammers.

Under APL/JHU Subcontract 600444, the Engineering Experiment Station (EES) at the Georgia Institute of Technology has provided direct support of this effort with particular emphasis on the system's scanning antennas. Specifically, EES has conducted design studies leading to the specification of a generic antenna type which could perform the acquisition function and then relay the information to an associated tracking system.

As stated above, a frequency must be chosen which has appropriate absorption characteristics. That is, the atmospheric attenuation should be sufficient to neutralize the effect of long-range, stand-off jammers while allowing a detectable radar return signal over the desired acquisition volume. Initially, 23 GHz was suggested as the frequency of operation since this corresponds to the lowest water vapor absorption frequency (see Figures 16 and 17 in Section III.B). This frequency has an attendant one way propagation loss on the order of 0.2 dB/km which will allow radar sensing while affording some jammer protection. An alternate frequency which received attention was the next highest frequency, above the 23 GHz peak, which had the same attenuation value or about 46 GHz. Choosing this higher frequency will allow either smaller antenna dimensions for a given gain or higher gains for a given aperture size. Later in the study program, it became apparent that rainfall attenuation seriously degraded performance at both 23 and 46 GHz; therefore, it was decided to compare the performance of several typical systems having frequencies

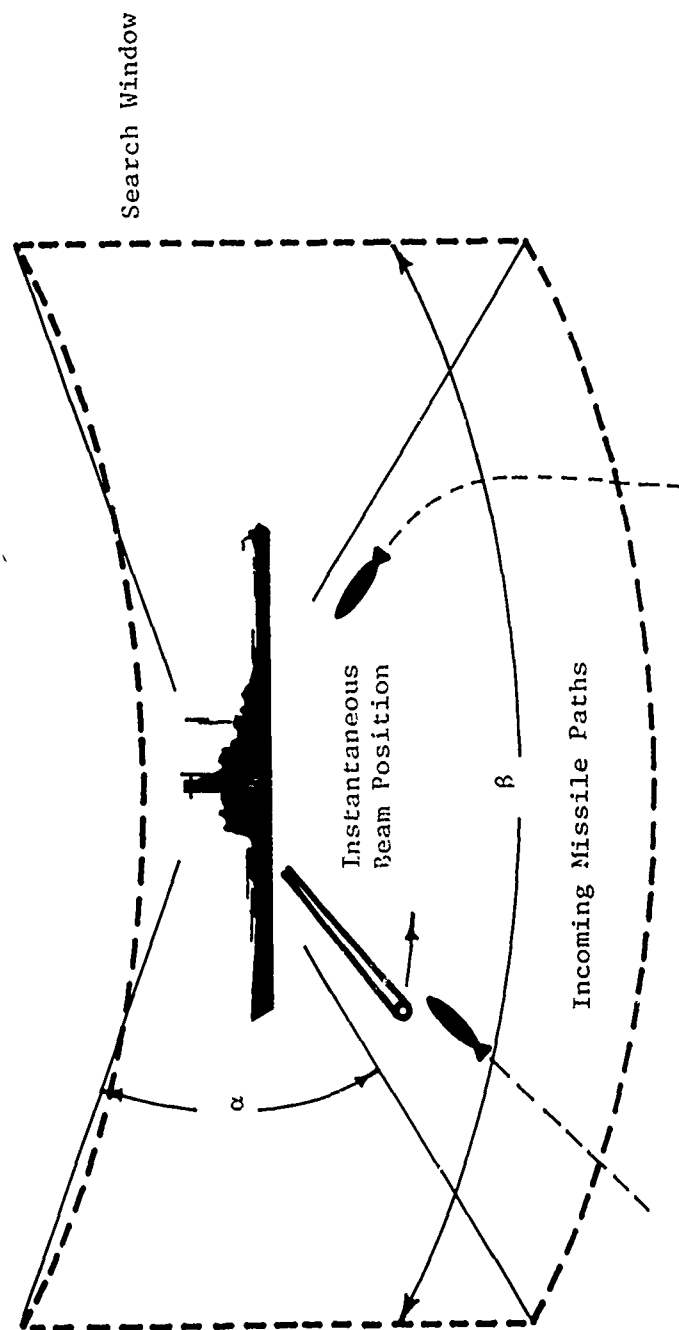


Figure 1. Typical short-range, self-defense scenario illustrating large target, incoming airborne attack vehicles, and radar coverage sector.

between 10 and 95 GHz. It will be noted, however, that most of the study was concerned with the two initial frequencies 23 and 46 GHz.

The performance of a radar system depends not only on the chosen frequency (and its attendant absorption loss) but on such other obvious parameters as available rf power, component losses, multipath and weather effects, beam shape, and scan format. Consequently, attention was given to several of these related factors before an antenna configuration was derived. The results of a brief component survey are contained in Section II. This survey includes several component types for 23 and 46 GHz and available high-power sources for 10, 16.5, 23, 35, 46, 70 and 95 GHz. Models for calculating the effects of such environmental factors as multipath, atmospheric absorption, and rainfall are presented along with several sample calculations in Section III. Since such important antenna parameters as beamwidth, sector width, scan rate, and scan format depend directly on the particular target of interest and the system application, Section IV is devoted to the characterization of the target and the mission. Both tracking and acquisition are treated in that section. Section V includes detailed descriptions of numerous candidate antenna schemes along with a summary of their relative merits and applicability to this problem. Among the candidates discussed are frequency scanners, phased arrays, multiple beam networks, electromechanical scanners, and various combinations of these techniques. Recommendations as to acquisition and tracking system formats and an antenna concept are presented in the last section.

II. MILLIMETER RADAR COMPONENT SURVEY

At least two distinctly different messages can be detected in the current statements and funding trends of certain governmental agencies: (1) a radar (or other) system can be developed most economically by tying the desired performance and therefore application directly to available components and (2) the funding of programs and the expression of interest in a particular little used portion of the spectrum will stimulate American industry to develop affordable components in that region. Both of these approaches have substance depending on whether a specific item of hardware is needed subject to limited funds or whether a long range capability in a particular band is desired. One important question which must be answered when pursuing the second approach above is "Are components scarce at a particular frequency because of a limited market or because of technological barriers."

The approach taken on this particular study was somewhere between the two approaches listed. One would certainly hope that a usable radar system could be developed to accompany any antenna concept resulting from this study program; however, it would be regrettable to eliminate a particular frequency (such as the 23-GHz water line) from consideration strictly because key components were available at nearby frequencies but not at that particular one.

Much of the early radar work found that several portions of the RF spectrum were not useful due to their high attenuation of RF energy. Since radar's beginning it seems that many involved in radar systems design have also tried to avoid confrontation with these energy absorbing portion of the spectrum. Consequently, component availability is severely limited at the several frequencies of interest.

Several high power sources are available at frequencies somewhat close to those desired. However, the manufacturers of these components have indicated that the existing designs may be either redesigned or scaled to the frequencies that we require. For instance a high power magnetron is available at 37 GHz and may be scaled up to 46 GHz for a nominal charge of approximately \$8,000. However, a company going through a complete tube redesign or research and development effort

involving from six to nine months can charge \$50,000 to \$100,000 or even more. Hence, those companies who are able to scale current tube designs will be listed and others will not.

Other active components such as solid state sources, mixers and switches are readily obtainable from several companies. These companies indicate that if any specification is required which is not currently listed for presently available models, redesign can be accomplished for an amount which is quite small in relation to component costs.

Passive components are available from several companies with each company offering quite a broad selection. Many passive components have not been listed because their availability is not limited. Those which are described are mentioned either because of their limited use, peculiar characteristics or because it was thought that their characteristics would have questionable performance applicability. Their appearance in the list along with specific performance data should answer any application questions.

In general, components will be listed which most commonly appear in radar systems. With each component mentioned will appear a list of its characteristics. A price will be given if available. Many of the prices listed were price estimates based on current rate for engineering, current material prices, quantity and the state of the electronics market. In some cases costs were in question; this was usually the case where design would have to be performed.

NOTE: The following component survey was performed by Georgia Tech personnel during the months of December 1975 and January 1976. All data and prices listed were obtained from either written quotations, published catalogs or telephone conversations. Although the surveyors made an earnest attempt to include several typical suppliers, it is recognized that the list of vendors surveyed is not complete, and it is emphasized that no attempt has been made to exclude any vendor. Above all, it is emphasized that the inclusion of any product in no way represents an endorsement of such product by either the United States Government, the Applied Physics Laboratory, or the Georgia Institute of Technology.

<u>Component</u>	<u>Characteristics</u>	<u>Price</u>
<u>Solid State Sources</u>		
<u>Gunn Oscillators</u>		
Hughes Aircraft	f = 23 GHz, full band Mechanically tuned, 150 mW	\$ 735
	Varactor Tuned, 50 mW	920
Sonoma	f = 23 GHz, full band Mechanically tuned, 100 mW	1300
	250 mW	1800
	f = 46 GHz, full band Mechanically tuned, 100 mW	2000
TRG	f = 23 GHz, BW = \pm 500 MHz Mechanically tuned, 50 mW	295
	f = 46 GHz, BW = \pm 500 MHz Mechanically tuned, 50 mW	1150
<u>*Impatt Oscillators</u>		
Hughes (Torrance)	f = 46 GHz, BW = \pm 2.5 GHz Mechanically tuned, 100 mW	2900
	50 mW	1900
<u>Mixers</u>		
(Balanced W/I.F. amp)		
Hughes	B.W. = 3 GHz I.F. = 160 MHz, self biased NF = 6.5 dB Sensitivity = -85 dBm Drive required = 3 mW f = 23 GHz	2950
	f = 46 GHz	3950
Spacekom, Inc.	BW = 2 GHz I.F. = 160 MHz NF = 6.5 dB f = 23 GHz	2200
	f = 46 GHz	3700
Westinghouse	BW = 50-75 MHz for 100 nsec. pulse width I.F. freq. = 160 MHz f = 23 GHz, NF \leq 6.5 dB f = 46 GHz, NF \leq 7 dB	**

*Typically, Impatt Oscillators are quite noisy and are not usually found in millimeter wavelength systems.

** Not available off-the-shelf but well within the realm of their technology. In fact, they appear very capable.

<u>Component</u>	<u>Characteristics</u>	<u>Price</u>
<u>Magnetrons</u>		
Litton	f = 24 GHz, model L4154	\$ 990
	Peak power = 65 kW, pulse length = 1 μ sec (May be scaled to 23 GHz)	
	f = 34.8 GHz model L4064A	1750
	Peak power = 125 kW, pulse length = 1 μ sec (May be scaled to 46 GHz with a decrease in peak power; price for scaling = \$7,000 to \$10,000)	
	f = 34.7 to 34.93 GHz, model L4516	2770
	Peak power = 110 kW, pulse length = 1 μ sec (May be scaled to 46 GHz with a decrease in peak power; scaling costs = \$7,000 to \$10,000)	
Varian	f = 23.8 to 24.27 GHz	8000
	Peak power = 40 kW, pulse length = 0.5 μ sec (May be scaled down to 23 GHz)	
<u>TWT's (High Power)</u>		
Hughes	f = 15.5 - 17.5 GHz, scaling to 23 GHz50,000
	Peak power (50% duty) = 13 kW, BW = 100 MHz Gain = 45-50 dB	
Watkins-Johnson	f = 23 GHz, Cathode pulsing	24,000
	Peak power (10% duty) = 10 kW, BW = 100 MHz Gain = 40-45 dB	
Siemens	f = 38 GHz, Scaling to 46 GHz	Not available
	Average power = 600 W Relatively high peak powers available but exact figures are not available	
<u>Klystrons</u>		
Varian	Low power	
	f = 23 GHz	
	22V10 - 150 mW	820
	24V10A - 200 mW	820
	24V11 - 600 mW	1140
	f = 46 GHz	
	45V10 - 85 MW	1410
	45V12 - 275 mW	1960
	High power	
	f = 23 GHz20,000
	Peak power (10% duty) = 10 kW Cathode pulsing	

<u>Component</u>	<u>Characteristics</u>	<u>Price</u>
<u>*TR Tubes</u>		
Varian (Bev.)	f = 23 GHz Power handling: Peak power = 40 kW Average power = 40 W Able to handle pulse length of 0.02 μ sec Insertion loss 1 dB	\$ 3000
<u>High Speed Switches</u> (Receiver Isolation)		
Baytron Co.	f = 46 GHz, BW = 1 GHz Isolation \geq 25 dB Insertion Loss \leq 0.8 dB VSWR \leq 1.2 Switch time = 3 μ sec	1000
Hughes Aircraft	f = 23 GHz, full band Isolation \geq 25 dB Insertion loss \leq 1 dB VSWR \leq 1.2 Switch time = 50 μ sec (f = 46 GHz, full band, \$1175)	1075
Sonoma Engineering and Research, Inc.	f = 23 GHz, BW = 2 GHz (46 GHz, BW = 2 GHz) Isolation \geq 35 dB Insertion Loss \leq 1 dB Switch time = 0.25 μ sec	1000
<u>Ferrite Phase Shifters</u>		
Electromagnetic Sciences	f = 23 GHz Bit switch time = 0.1 μ sec Insertion loss \leq 1 dB f = 46 GHz Long bit phase switching Bit switch time = 2 μ sec Insertion loss \leq 1.5 dB	100 each (large quantities) 125 each (large quantities)
Sonoma Engineering and Research, Inc.	f = 23 & 46 GHz Bit switch time = 1/4 μ sec Insertion, Loss \leq 1 dB Wideband Dimension: 1/4" long x W.G. flange size Switch power: 5 V @ 1 watt/unit 5% regulation gives 5% phase shift accuracy	100 each (large quantities)

*Practical TR tubes are not available at 46 GHz; insertion loss and noise becomes a problem at this frequency.

<u>Component</u>	<u>Characteristics</u>	<u>Price</u>
<u>Ferrite Phase Shifters</u> - Continued		
Raytheon	f = 23 GHz Less than 1 μ sec switch time Any - increment RMS - error < 5 $^{\circ}$ (non-reciprocal) " " < 10 $^{\circ}$ (reciprocal) Insertion loss < 1 dB Peak Power \sim 500 mW (for f = 46 GHz, Insertion loss \leq 1.5 dB)	\$ 200 each (large quantities)
<u>Couplers</u>		
Baytron Co.	f = 46 GHz, broadwall (high power) Coupling of 6, 10, 20, 30, 40 dB Directivity \geq 40 dB Coupling variation = 0.60 dB Peak power handling = 5 kW VSWR = 1.10 (mainline)	400
Microlab/FXR	f = 23 GHz, broadwall Coupling of 10, 20 dB Directivity > 40 dB Coupling variation = 0.4dB Peak power handling = 22 kW VSWR = 1.05 (mainline)	425
<u>Circulators</u>		
TRG	f = 23 GHz, BW = 15% Isolation \geq 18 dB Insertion loss \leq 0.6 dB VSWR \leq 1.3	475
	f = 46 GHz, BW = 10% Isolation \geq 20 dB Insertion loss \leq 0.8 dB VSWR \leq 1.4	675
<u>Isolators</u>		
TRG	f = 23 GHz, BW = 10% Isolation \geq 20 dB Insertion loss \leq 0.6dB VSWR \leq 1.3, low power	550
	f = 46 GHz, BW = 8% Isolation \geq 15 dB Insertion loss \leq 0.7 dB VSWR \leq 1.3, low power	600
	f = 46 GHz, BW = 4% Isolation \geq 18 dB Insertion loss \leq 0.8dB VSWR \leq 1.3 Peak power handling \leq 25 kW average power \leq 8 W	.00

<u>Component</u>	<u>Characteristics</u>	<u>Price</u>
<u>Isolators - Continued</u>		
Baytron	f = 46 GHz, bandwidth = ± 1 GHz Isolation ≥ 20 dB Insertion loss ≤ 0.6 dB VSWR ≤ 1.2	\$ 450
<u>Rotary Joints</u>		
Diamond Antenna & Microwave Corp.	f = 23 GHz, full band (WR-42) L-Shaped, 350 R.P.M. VSWR ≤ 1.5 Insertion loss ≤ 0.5 dB max. Peak power = 30 kW Average power = 50 W	720
	f = 46 GHz, full band (WR-22) L-shape, 350 R.P.M. VSWR ≤ 1.5 Insertion loss ≤ 0.4 dB Peak power = 25 kW Average power = 50 W	3600
Kelvin Mfg. Co.	f = 23 GHz, full band (WR-42) L-shaped, 50 R.P.M. VSWR ≤ 1.5 Insertion loss ≤ 0.7 dB Peak power = 20 kW Average power = 50 W	995
Struthers Electric	f = 23 GHz, bandwidth = ± 2 GHz (WR-42) L-shaped, 300 R.P.M. VSWR ≤ 1.5 Insertion loss ≤ 0.2 dB Peak power = 50 kW Average power = 60 W	625

Initially, this study effort dealt strictly with the frequencies 23 and 46 GHz. Toward the end of this effort, it became desirable to compare signal-to-noise calculations using realistic peak powers for a number of other frequencies. These peak powers are listed below along with one magnetron capable of generating it at a given frequency.

<u>Frequency (GHz)</u>	<u>Peak Power (kW)</u>	<u>Tube</u>	<u>Maximum Duty Cycle</u>
9.3	250	Typical	.001
16.5	100	Litton 7208	.0008
16.5	135	Litton 7208 B	.001
35	75-100	Ferranti VF55	.001
70	10	Litton L4547	.0005
95	8	Amperex DX 287	.001

III. ENVIRONMENTAL FACTORS

The performance of a radar system can be degraded from its ideal design level by the presence of various environmental factors. The most common of these factors are multipath, atmospheric absorption, and weather effects. These topics are addressed in this section.

A. Multipath Analysis

The radar detection problem is always complicated somewhat when the target of interest approaches very closely to an extended surface having electrical properties different from the medium containing the radar wave. Among such surfaces are the earth and the sea. The effect can assume one or both of two forms: (1) loss of target visibility due to significant radar return (clutter) from the surface, and (2) variation (either increase or decrease) in effective gain due to the interference pattern from an apparent image target below the surface. The image effect is actually the result of the recombination of two waves which follow two different paths, one direct and one reflected from the surface, between the radar and the target. The first effect listed above is not of primary importance to this application, since the target motion is so great with respect to the clutter that the clutter can be discriminated against in the Doppler domain.

The second effect, multipath, can be of significant importance, however, since the sea can be a good reflector at grazing angles, and the targets of interest can spend a large portion of their flight time very near the surface. The purpose of this section is to document multipath calculations which were performed not only for the two frequencies of primary interest, 23 and 46 GHz, but also for other representative ones such as 9.3, 16.5, 35, 70, and 95 GHz. The geometric factors involved in these calculations are shown in Figure 2. The equations used to calculate these multipath variations are presented below.

The electric field intensity at the target is given by

$$E_t = E(\gamma_1) + E(\beta_1) D \Gamma \exp \left[j \frac{-2\pi\Delta}{\lambda} - \frac{4\pi\Delta h \sin\psi}{\lambda} \right] . \quad (1)$$

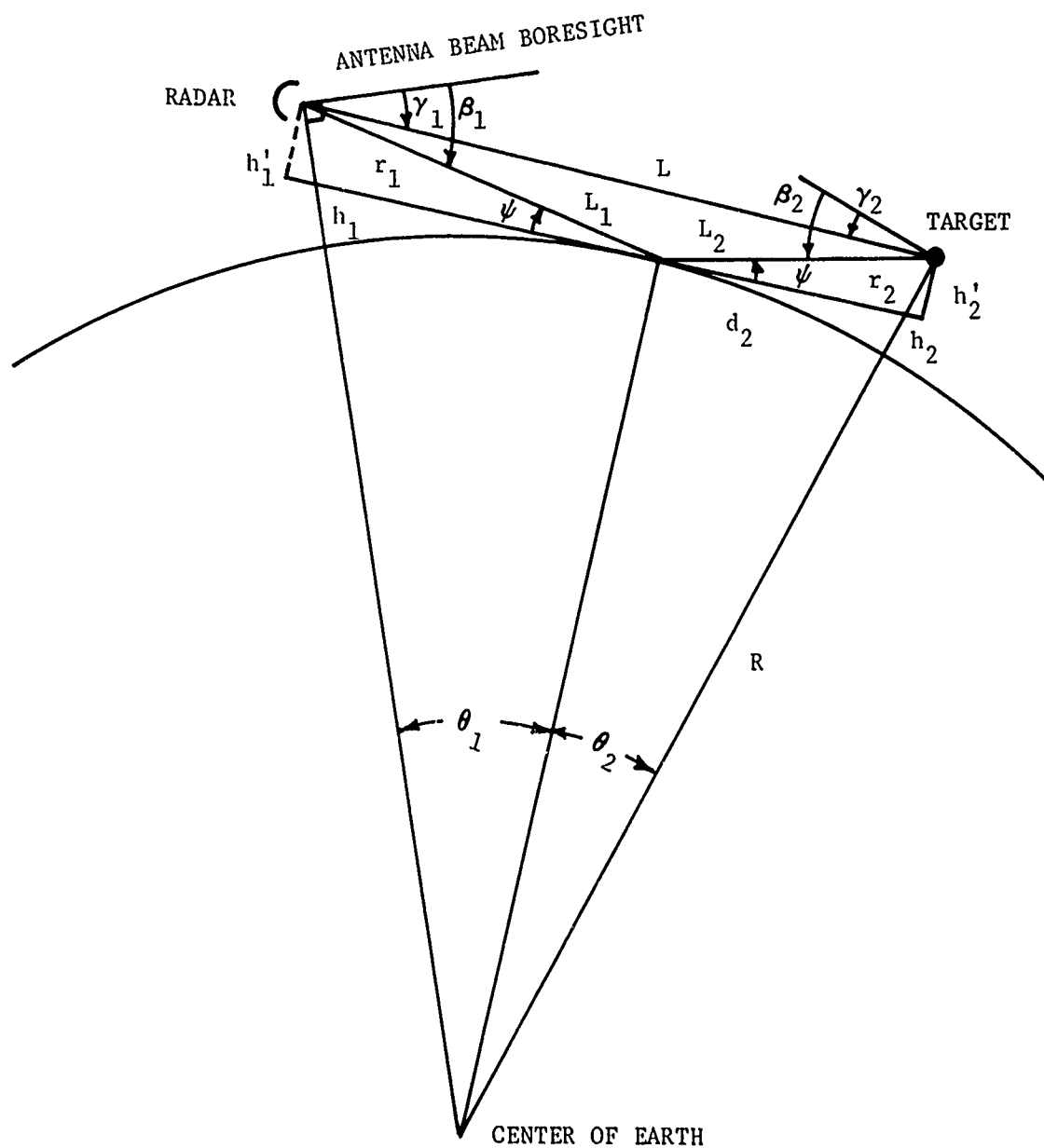


Figure 2. Geometric parameters used in the calculation of multipath interference.

Γ is the surface reflection coefficient calculated from

$$\Gamma = \frac{\sin \psi - [\epsilon - \cos^2 \psi]^{1/2}}{\sin \psi + [\epsilon - \cos^2 \psi]^{1/2}} \quad (2)$$

for horizontal polarization, and

$$\Gamma = \frac{\epsilon \sin \psi - [\epsilon - \cos^2 \psi]^{1/2}}{\epsilon \sin \psi + [\epsilon - \cos^2 \psi]^{1/2}} \quad (3)$$

for vertical polarization, where ϵ is the complex dielectric constant

$$\epsilon = \epsilon_1 - j\epsilon_2 \quad (4)$$

The other symbols are defined below.

$E(\alpha)$ = angular dependent field intensity pattern of the radar

γ_1, β_1 = angle with respect to the center of the radar beam of the target ray and the indirect ray, respectively,

D = surface divergence factor,

$$= \left[1 + \frac{2d_1 d_2}{Rd \sin \psi} \right]^{-\frac{1}{2}} \quad (6)$$

R = earth's radius,

$$\Delta = L - (L_1 + L_2),$$

$$L = \left[(R + h_1)^2 + (R + h_2)^2 - 2(R + h_1)(R + h_2) \cos \left(\frac{d}{R} \right) \right]^{1/2} \quad (7)$$

$$d = d_1 + d_2 \quad (8)$$

$$L_1 = \left[r_1^2 + (h_1')^2 \right]^{1/2} \quad (9)$$

$$L_2 = \left[r_2^2 + (h_2')^2 \right]^{1/2} \quad (10)$$

$$h_1' = (R + h_1) \cos \theta_1 - R \quad (11)$$

$$h_2' = (R + h_2) \cos \theta_2 - R \quad (12)$$

$$r_1 = (R + h_1) \sin \theta_1 \quad (13)$$

$$r_2 = (R + h_2) \sin \theta_2 \quad (14)$$

$$\theta_1 = d_1/R, \quad (15)$$

$$\theta_2 = d_2/R, \quad (16)$$

$$\psi = \arctan \left[(h'_1 + h'_2)/r \right], \quad (17)$$

$$r = r_1 + r_2, \quad (18)$$

$$\beta_1 = \theta_1 + \psi, \quad (19)$$

$$\beta_2 = \theta_2 + \psi, \quad (20)$$

$$\gamma_1 = \arcsin \left[\frac{2(h_2 - h_1) R + h_2^2 - h_1^2 - L^2}{2L(R + h_1)} \right], \quad (21)$$

$$\gamma_2 = -\arcsin \left[\frac{2(h_2 - h_1) R + h_2^2 - h_1^2 + L^2}{2L(R + h_1)} \right], \quad (22)$$

for $h_1 \geq h_2$:

$$d_1 = \frac{d}{2} - p \cos\left(\frac{\phi + \pi}{2}\right), \quad (23)$$

$$d_2 = d - d_1, \quad (24)$$

$$p = \frac{2}{\sqrt{3}} \left[R(h_1 + h_2) + \left(\frac{d}{2}\right)^2 \right]^{1/2}, \quad (25)$$

$$\phi = \arccos \left[\frac{2Rd(h_2 - h_1)}{p^3} \right], \quad (26)$$

for $h_2 \geq h_1$:

$$d_2 = \frac{d}{2} - p \cos\left(\frac{\phi + \pi}{2}\right), \quad (27)$$

$$d_1 = d - d_2, \quad (28)$$

$$p = \frac{2}{\sqrt{3}} \left[R(h_1 + h_2) + \left(\frac{d}{2}\right)^2 \right]^{1/2}, \quad (29)$$

$$\phi = \arccos \left[\frac{2Rd (h_1 - h_2)}{p^3} \right] \quad (30)$$

Equation 1 was evaluated for the special case of a target closing radially on the radar with the peak of the main beam always on the target (i.e., $\gamma_1 = 0$) as a function of range d for several frequencies and the following set of parameters:

Antenna height (h_1) = 30 feet

Target height (h_2) = 50 feet

Frequency = 9.3, 16.5, 23, 35, 46, 70, 95 GHz

RMS wave height (Δh) = 1 foot

ϵ (of sea water) = $80 - j 774$.

An antenna pattern having a beamwidth of 1° and 23 -dB sidelobes was chosen as typical for the radar. This pattern may be described mathematically as

$$E(\alpha) = \frac{2a}{\pi} \frac{\cos \left(\frac{u}{2} \right)}{1 - \left(\frac{2u}{\pi} \right)}, \quad (31)$$

where,

$$u = \frac{\pi a}{\lambda} \sin \alpha, \quad (32)$$

and a is the aperture dimension.

The squared magnitude of the horizontal and vertical components of the field given by Equation 1 is plotted for the above inputs in Figures 3 through 9. In these plots, gain and range dependence has been normalized so that the variations shown are variations with respect to the signal which would be incident in the absence of multipath. To observe the effect of sea state, the equation was evaluated again at 9.3, 23, and 95 GHz (see Figures 10,11,12) for a wave height of two feet. The power nulls are shown to move further out in range as the target height above the ocean is increased to 100 feet and 500 feet as illustrated in Figures 13 and 14. Also, the peak-to-peak variation decreases as the wave-height-to-wavelength ratio increases (i.e., the reflections are more diffuse).

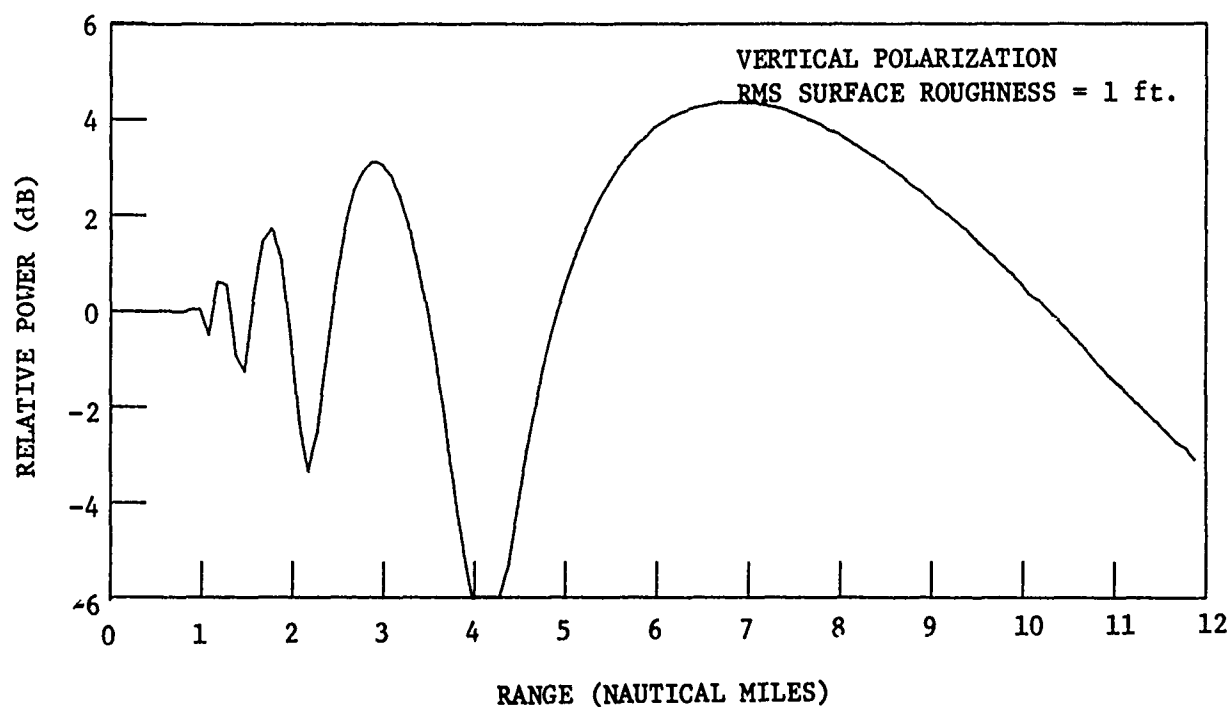
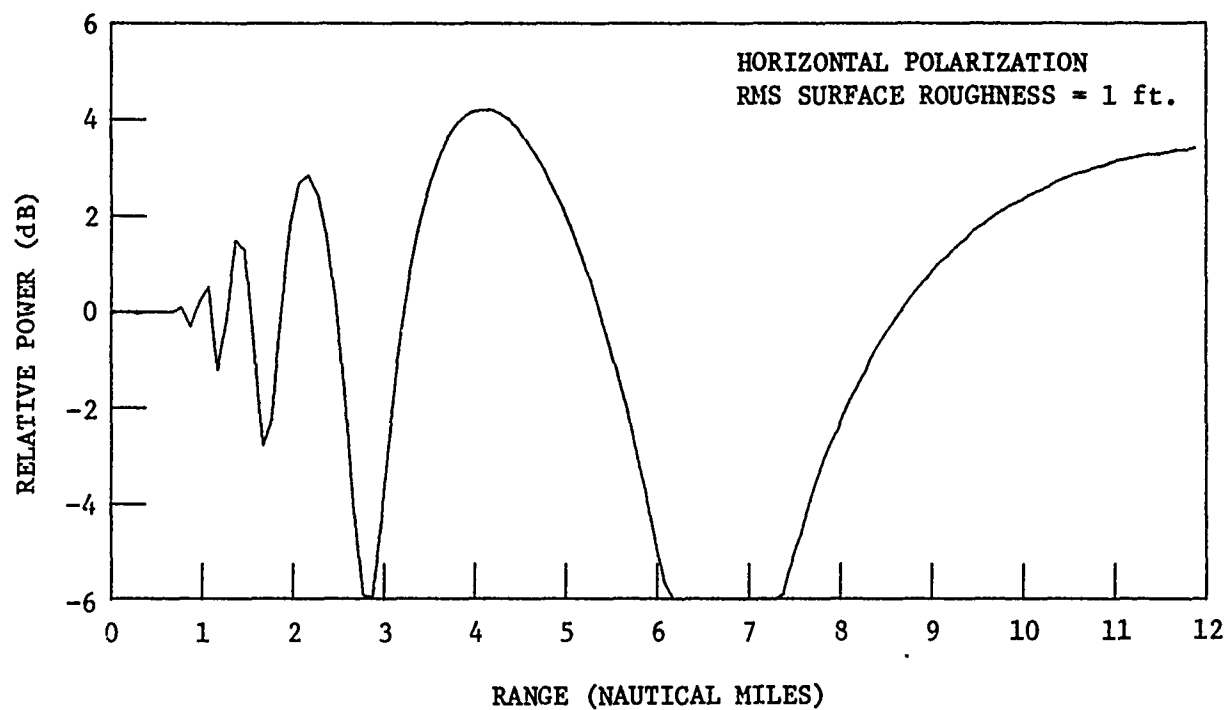


Figure 3. Calculated rf (9.3 GHz) power incident on a target located 50 ft. above the surface of the sea (rms roughness indicated) shown as a function of horizontal range. Radar beam model chosen has 1.0° beamwidth and 23 dB sidelobes. Radar located 30 feet above water.

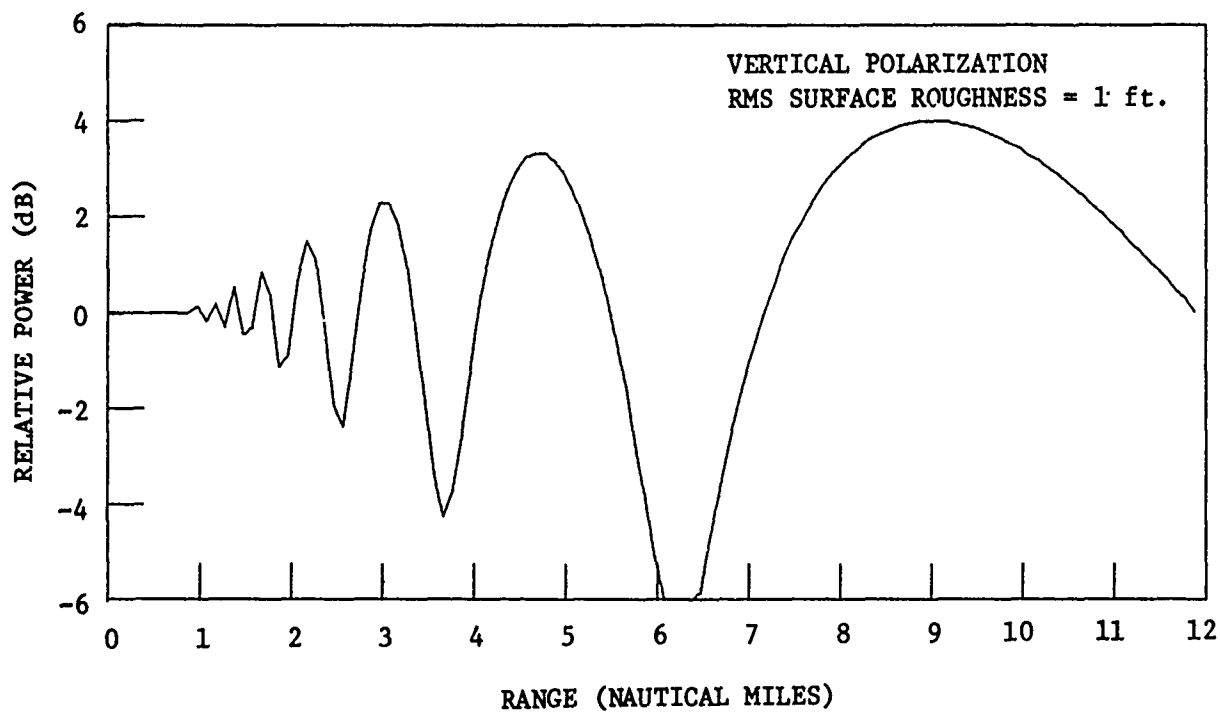
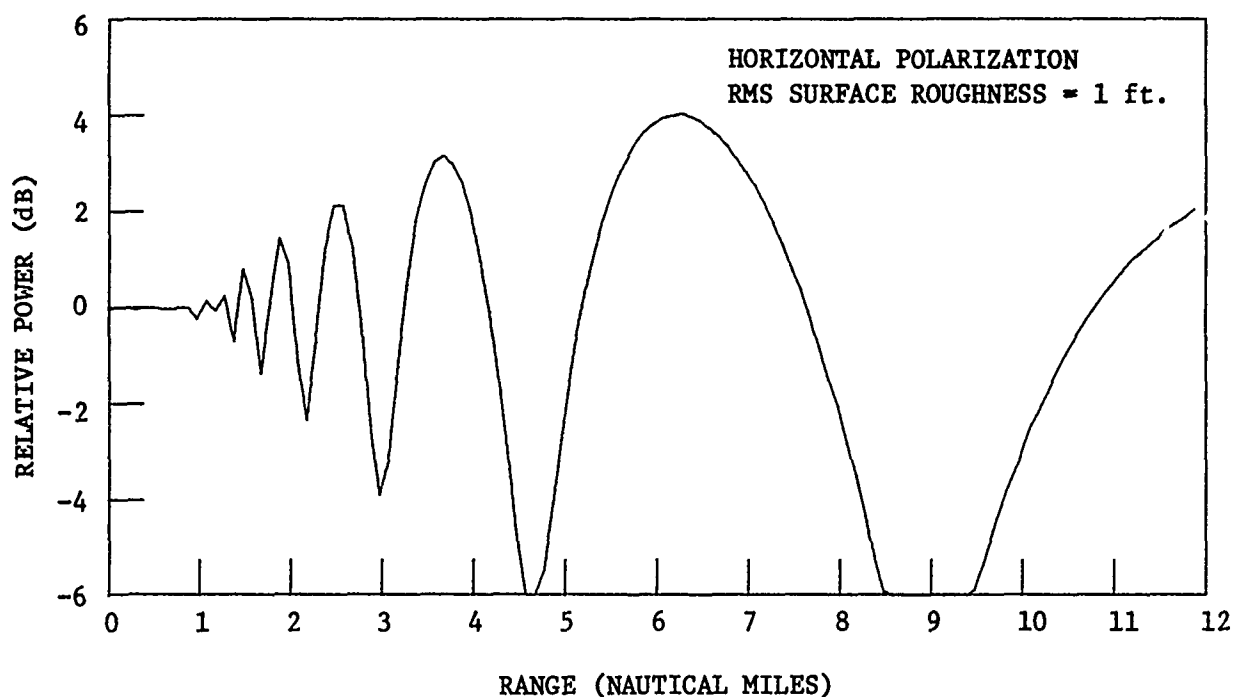


Figure 4. Calculated rf (16.5 GHz) power incident on a target located 50 ft. above the surface of the sea (rms roughness indicated) shown as a function of horizontal range. Radar beam model chosen has 1.0° beamwidth and 23 dB sidelobes. Radar located 30 feet above water.

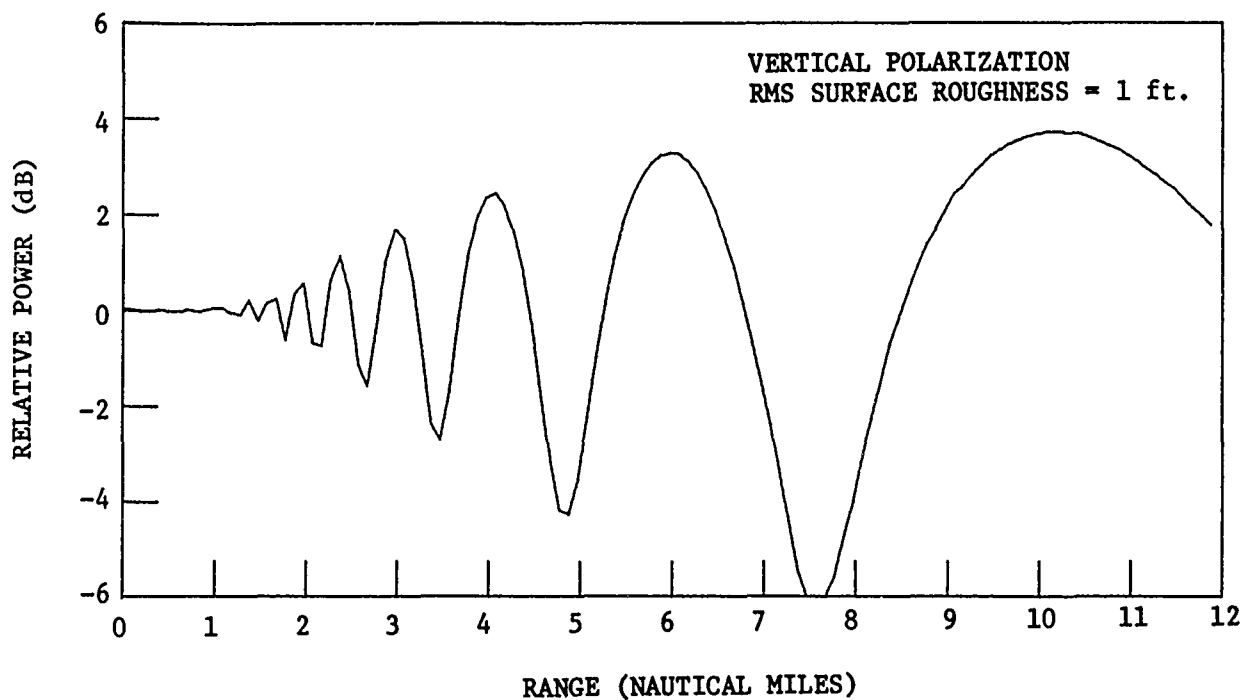
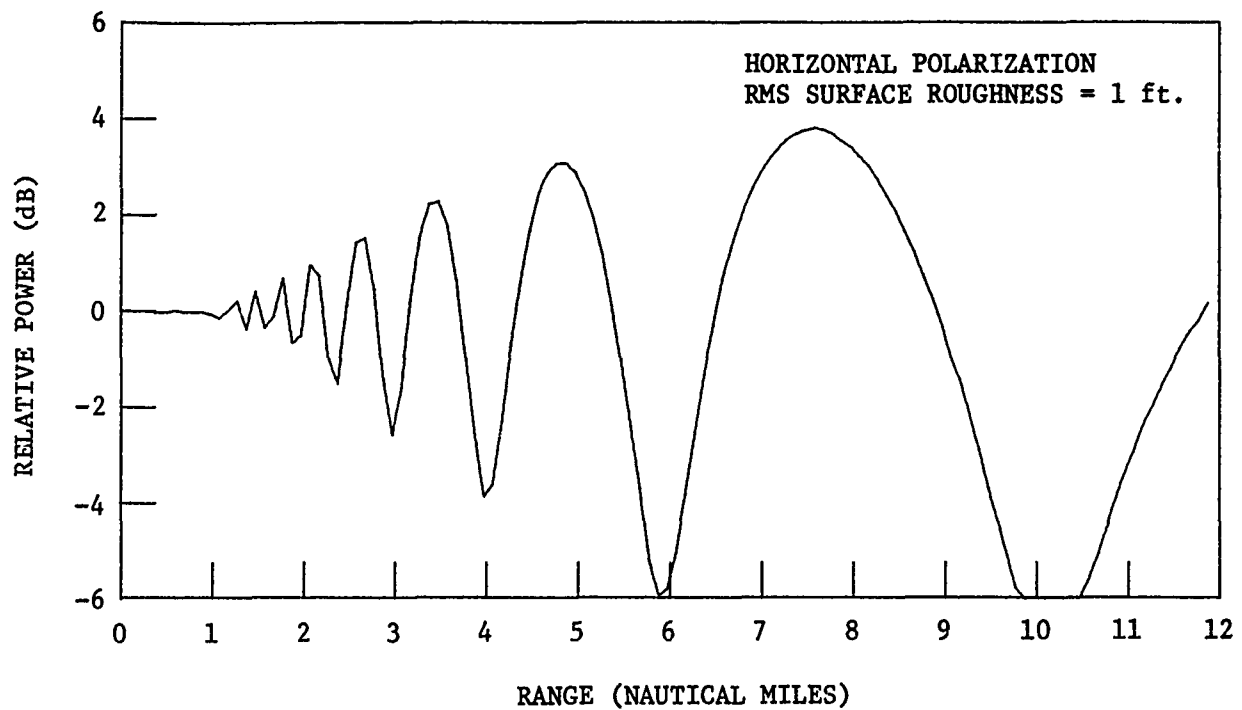


Figure 5. Calculated rf (23 GHz) power incident on a target located 50 ft. above the surface of the sea (rms roughness indicated) shown as a function of horizontal range. Radar beam model chosen has 1.0° beamwidth and 23 dB sidelobes. Radar located 30 feet above water.

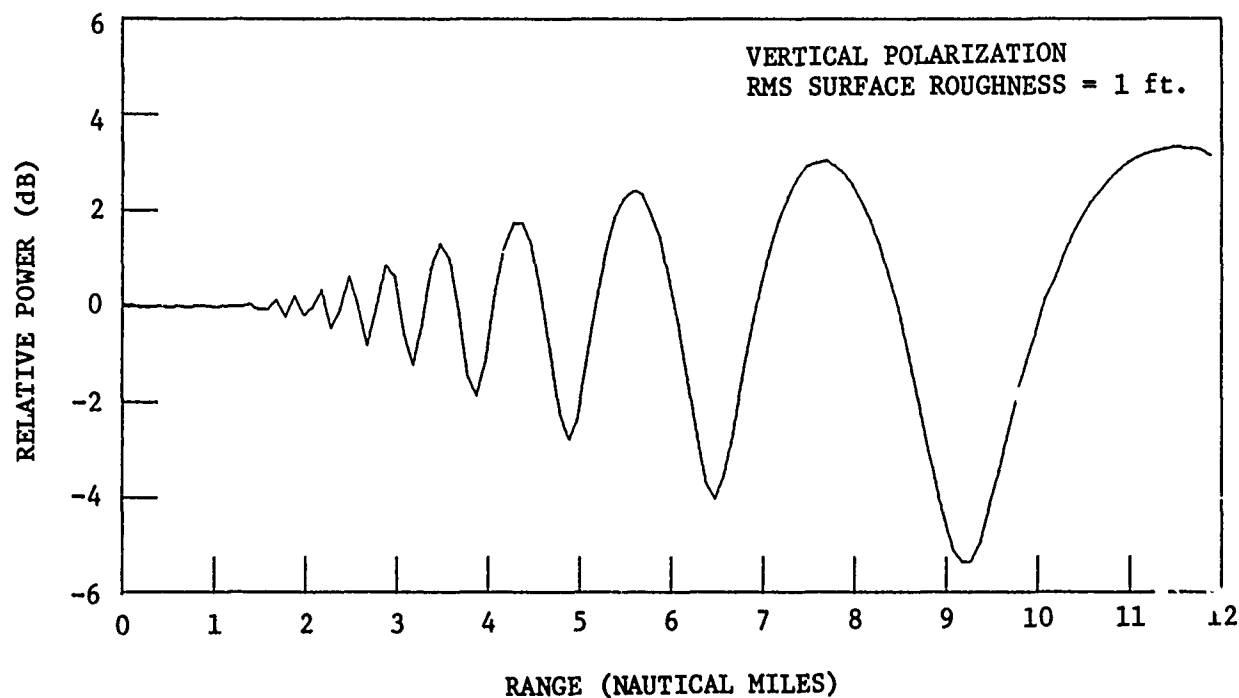
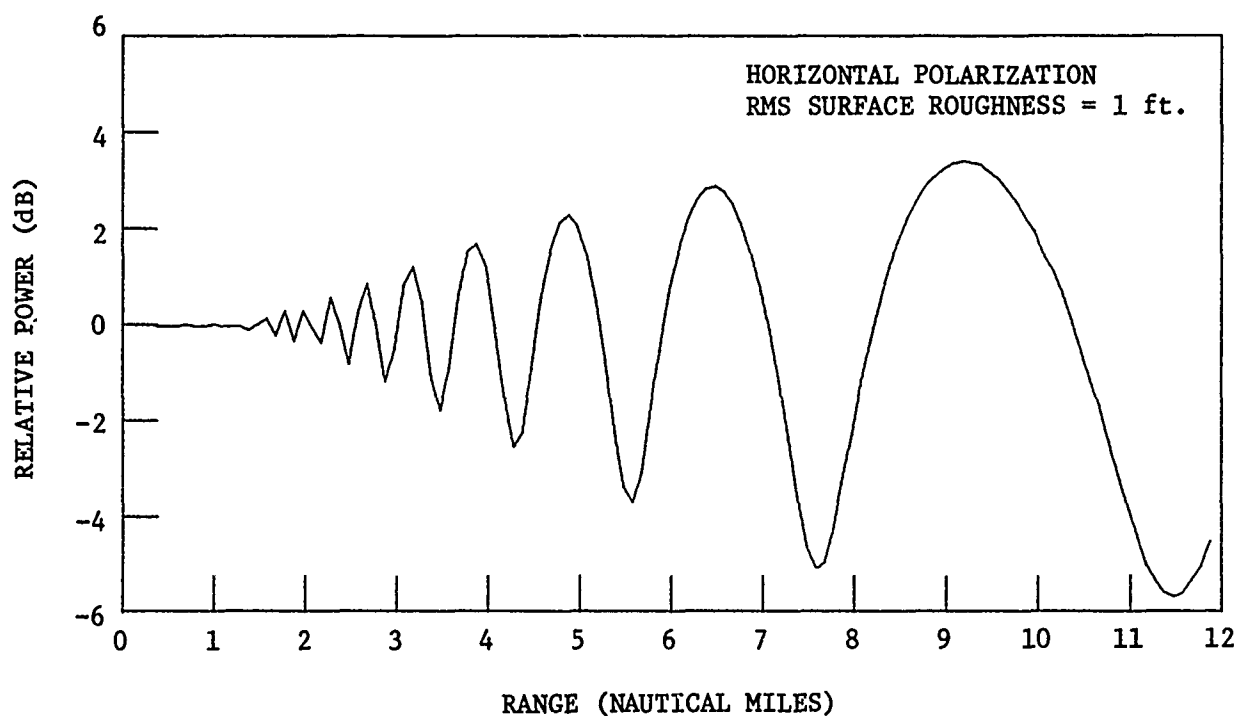


Figure 6. Calculated rf (35 GHz) power incident on a target located 50 ft. above the surface of the sea (rms roughness indicated) shown as a function of horizontal range. Radar beam model chosen has 1.0° beamwidth and 23 dB sidelobes. Radar located 30 feet above water.

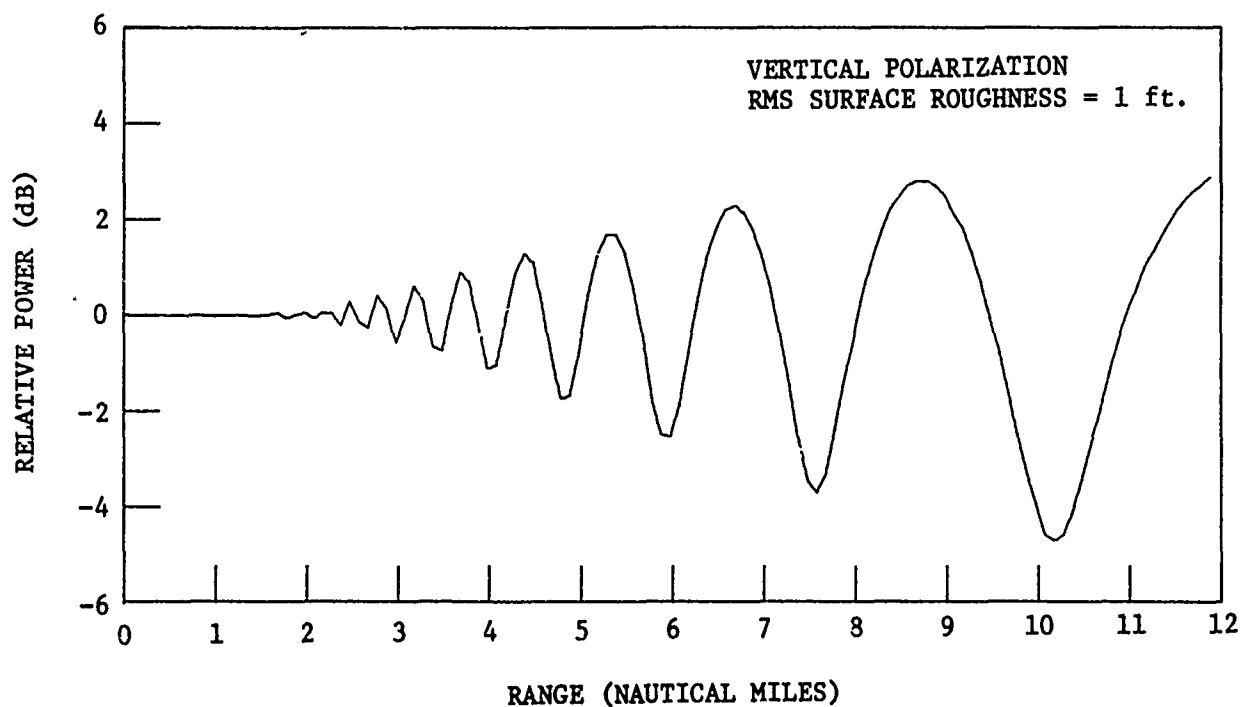
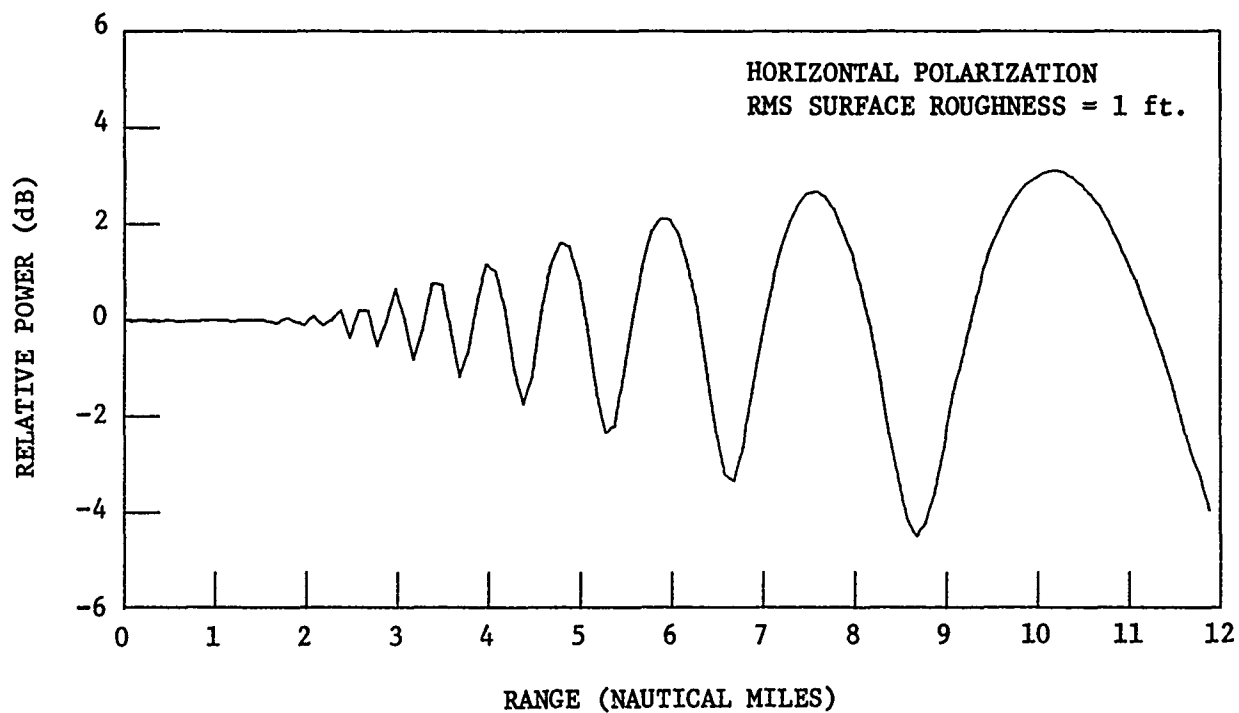


Figure 7. Calculated rf (46 GHz) power incident on a target located 50 ft. above the surface of the sea (rms roughness indicated) shown as a function of horizontal range. Radar beam model chosen has 1.0° beamwidth and 23 dB sidelobes. Radar located 30 feet above water.

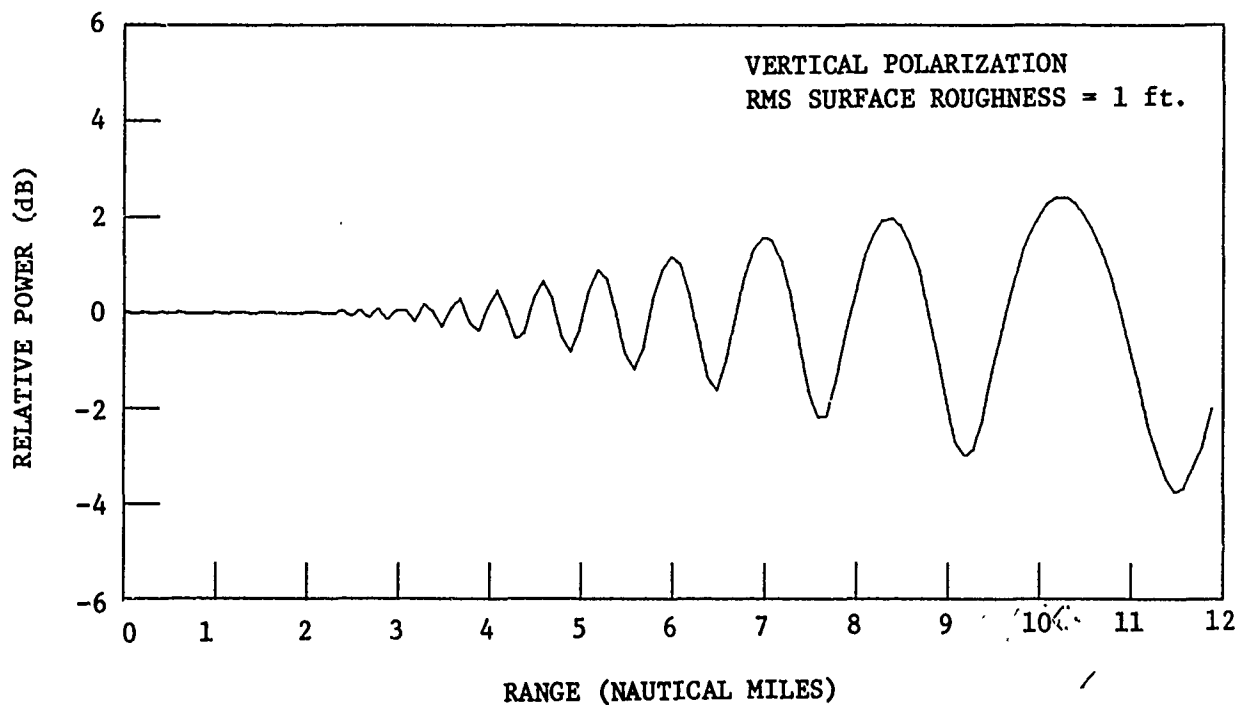
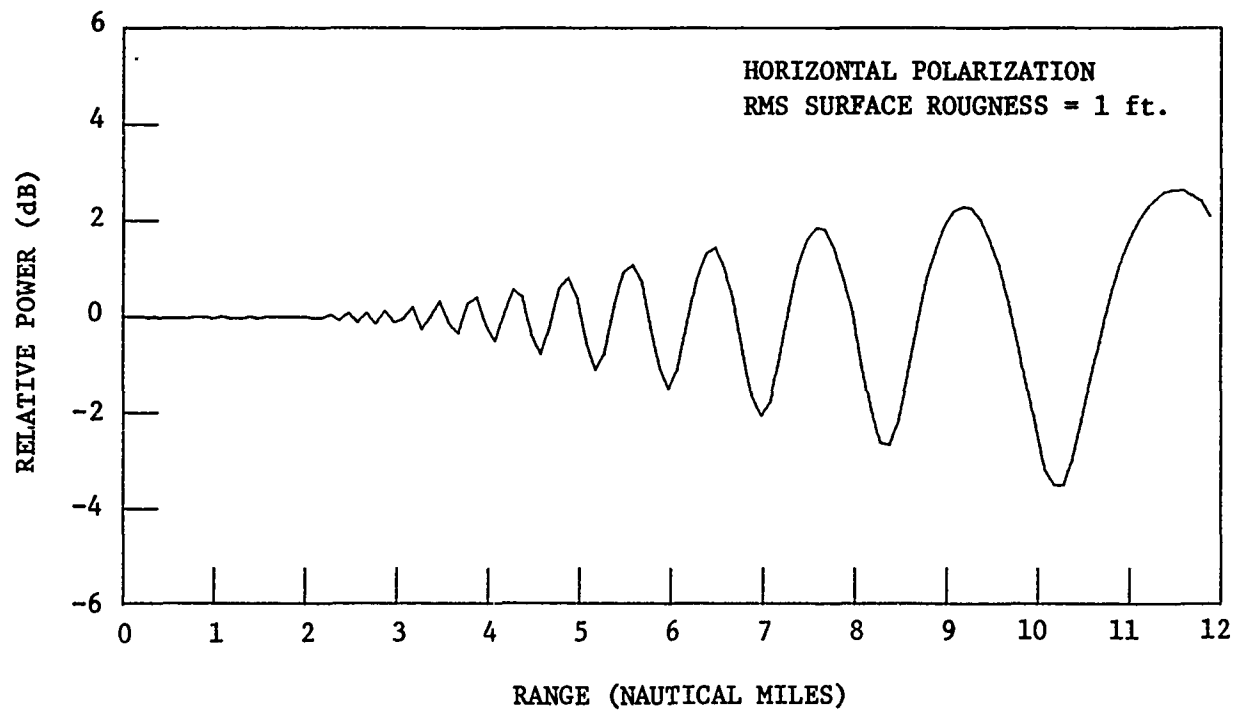


Figure 8. Calculated rf (70 GHz) power incident on a target located 50 ft. above the surface of the sea (rms roughness indicated) shown as a function of horizontal range. Radar beam model chosen has 1.0° beamwidth and 23 dB sidelobes. Radar located 30 feet above water.

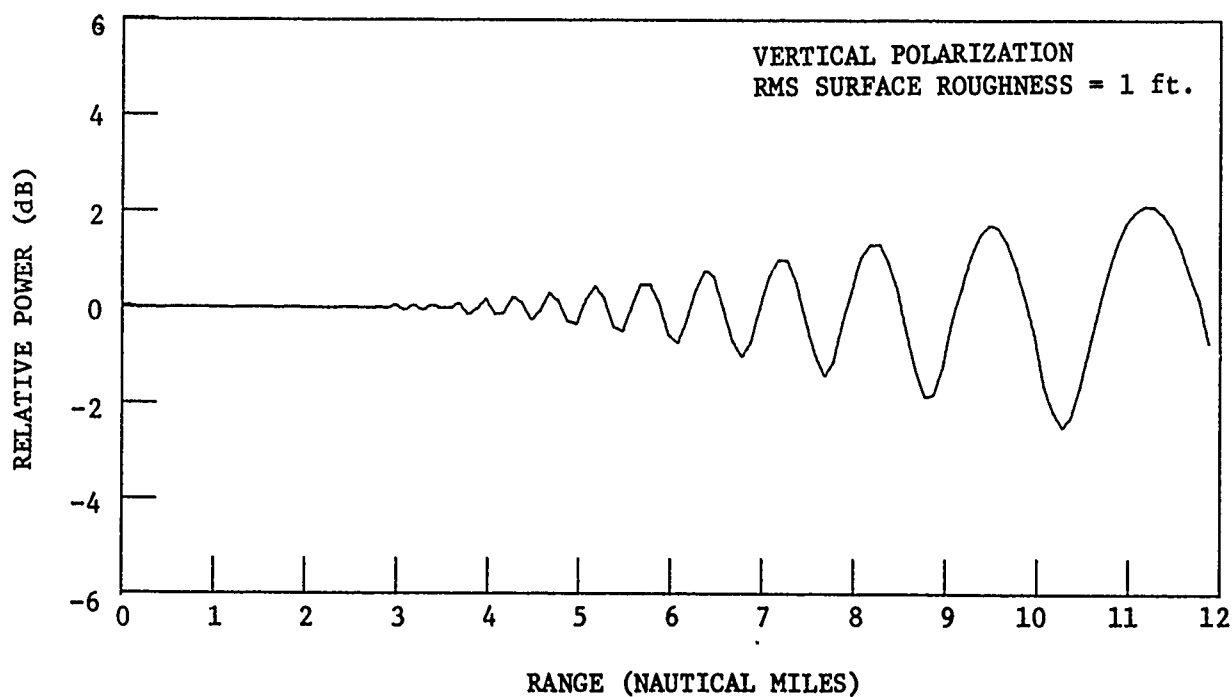
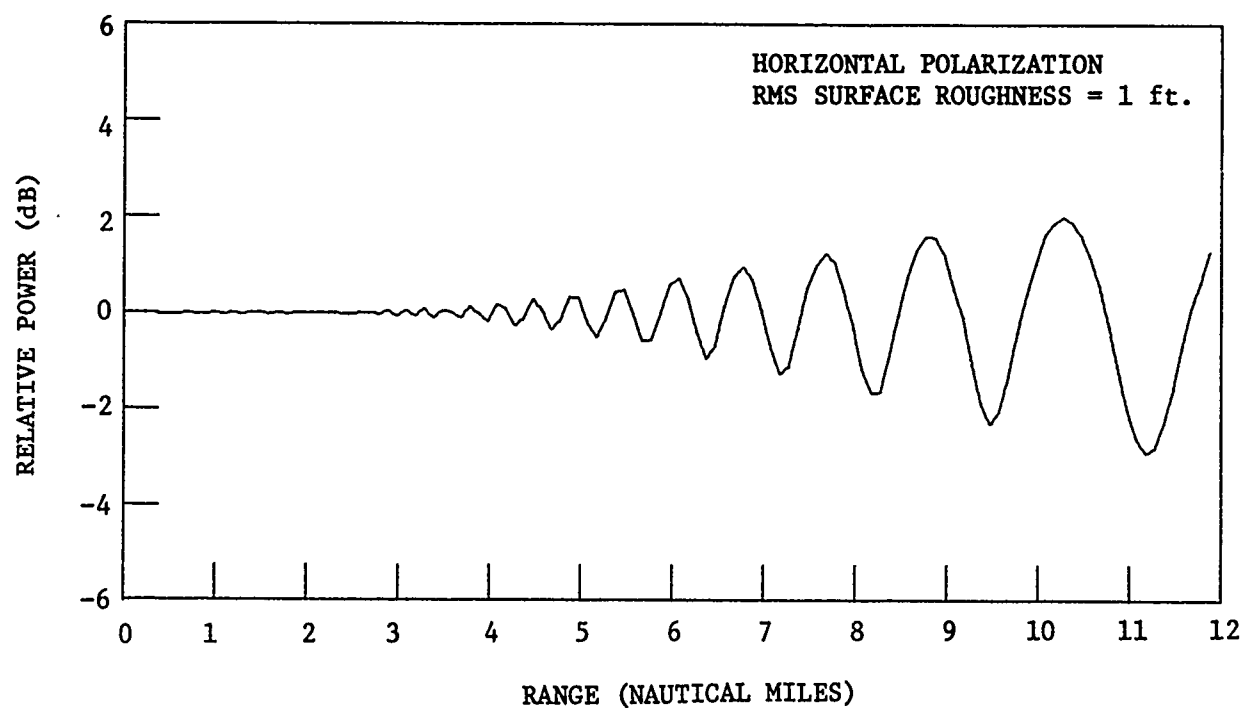


Figure 9. Calculated rf (95 GHz) power incident on a target located 50 ft. above the surface of the sea (rms roughness indicated) shown as a function of horizontal range. Radar beam model chosen has 1.0° beamwidth and 23 dB sidelobes. Radar located 30 feet above water.

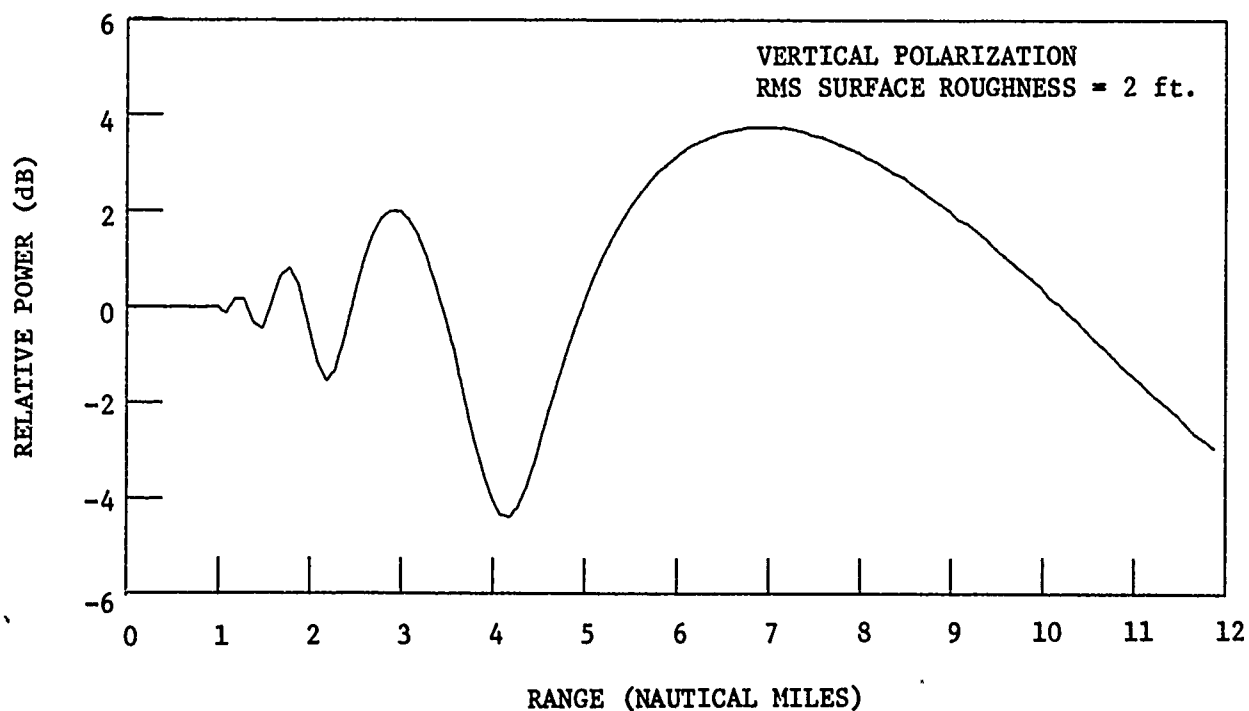
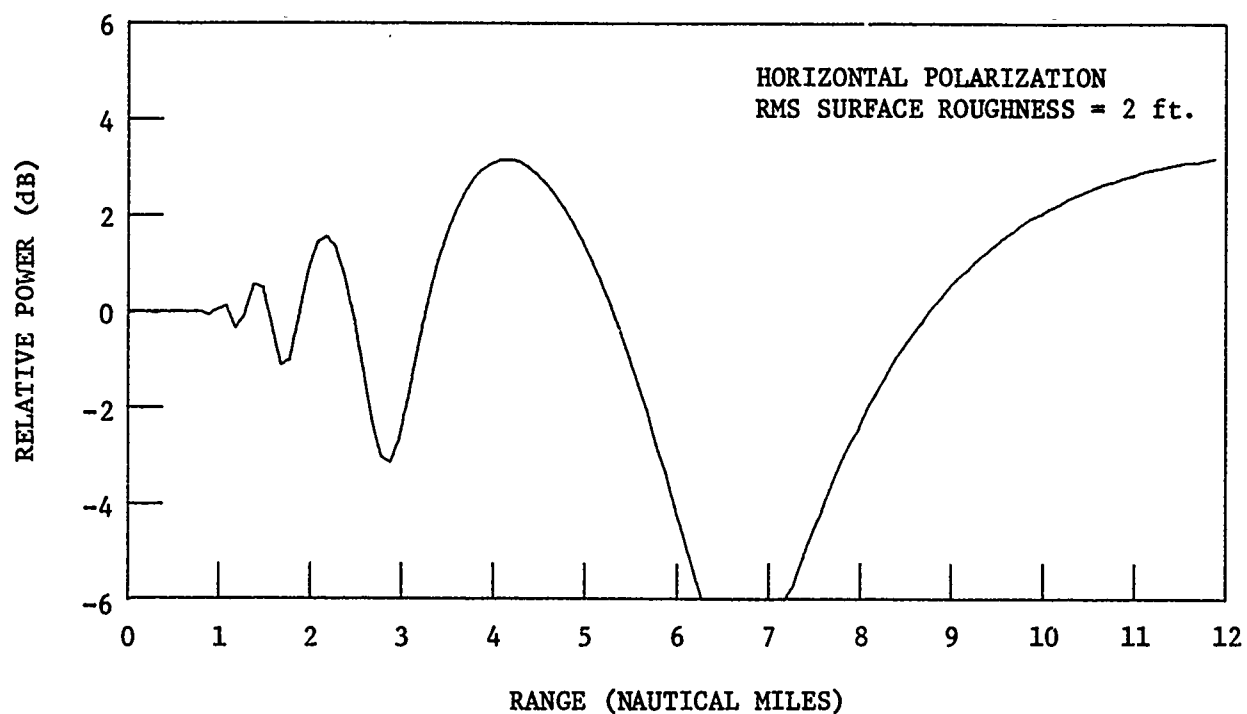


Figure 10. Calculated rf (9.3 GHz) power incident on a target located 50 ft. above the surface of the sea (rms roughness indicated) shown as a function of horizontal range. Radar beam model chosen has 1.0° beamwidth and 23 dB sidelobes. Radar located 30 feet above water.

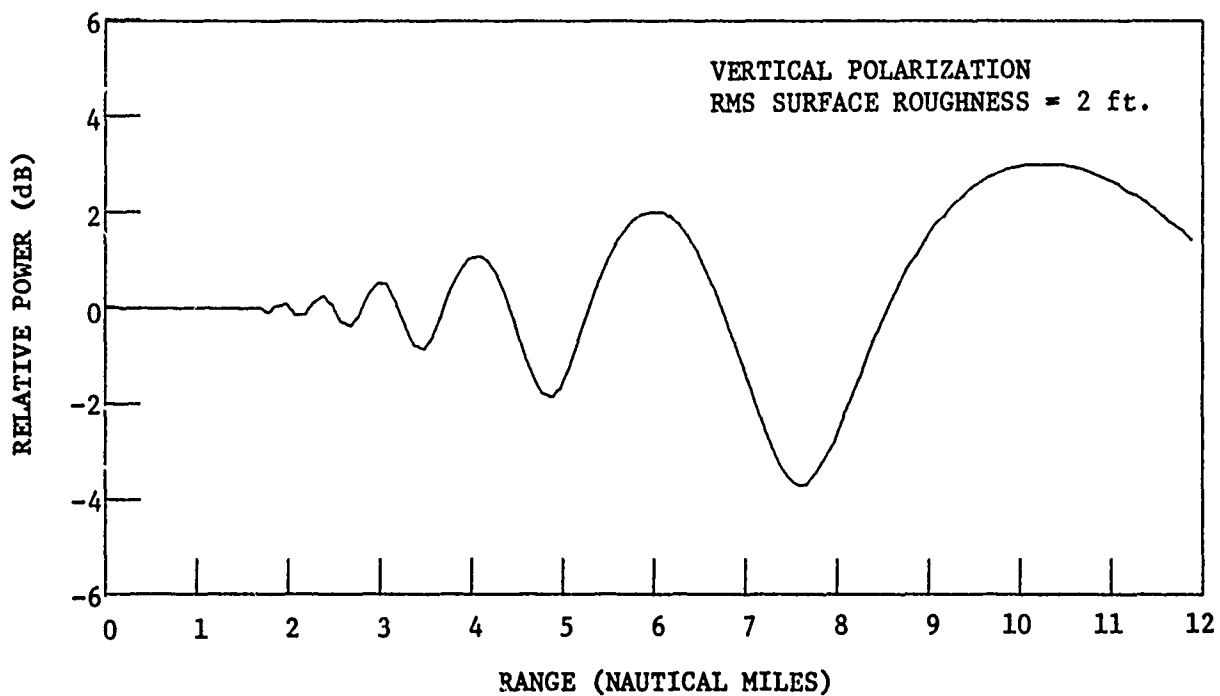
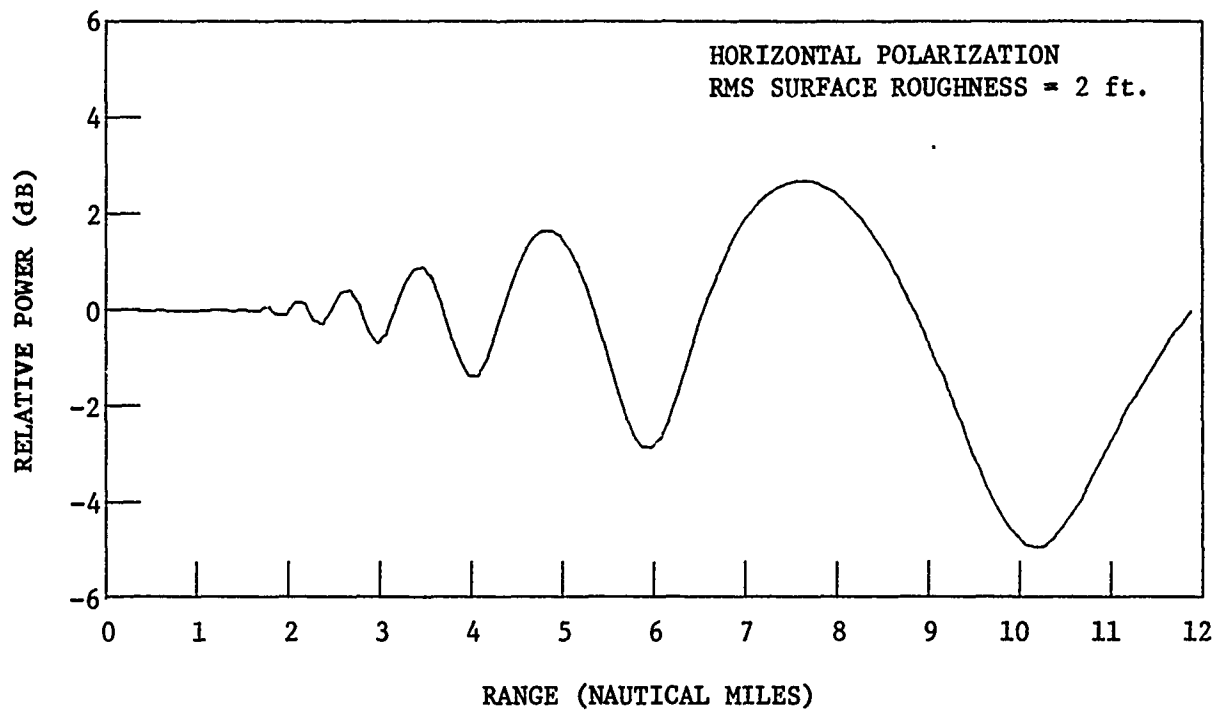


Figure 11. Calculated rf (23 GHz) power incident on a target located 50 ft. above the surface of the sea (rms roughness indicated) shown as a function of horizontal range. Radar beam model chosen has 1.0° beamwidth and 23 dB sidelobes. Radar located 30 feet above water.

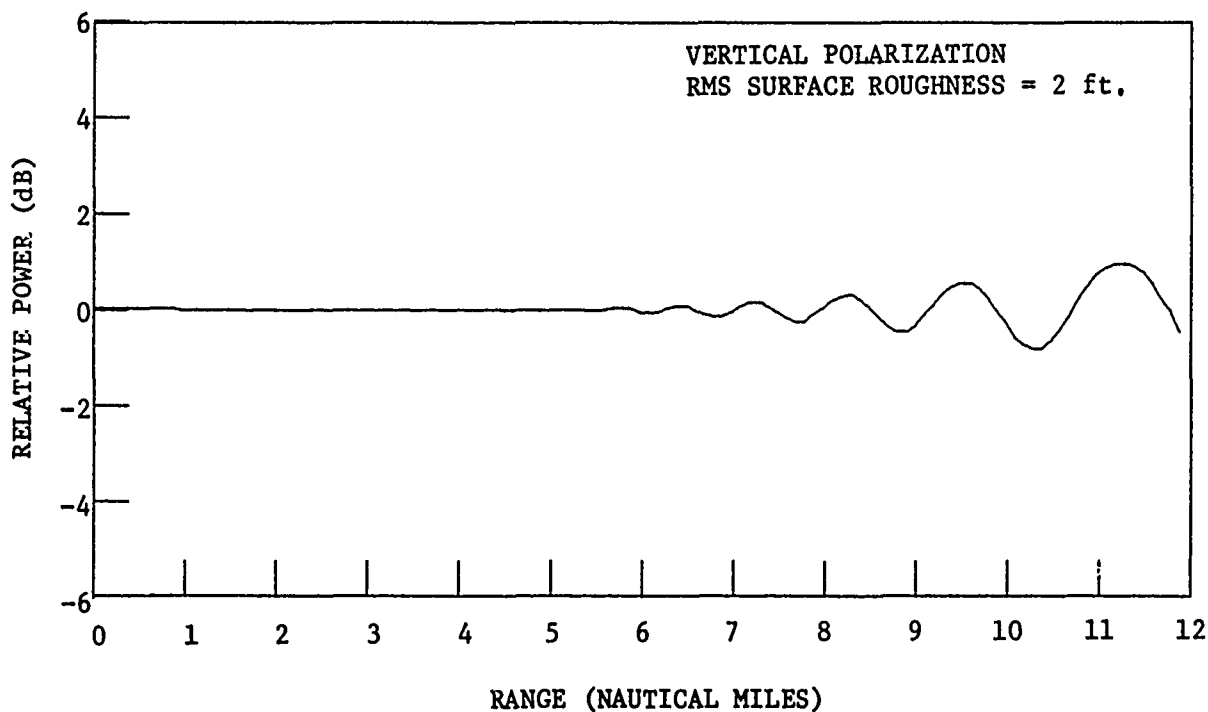
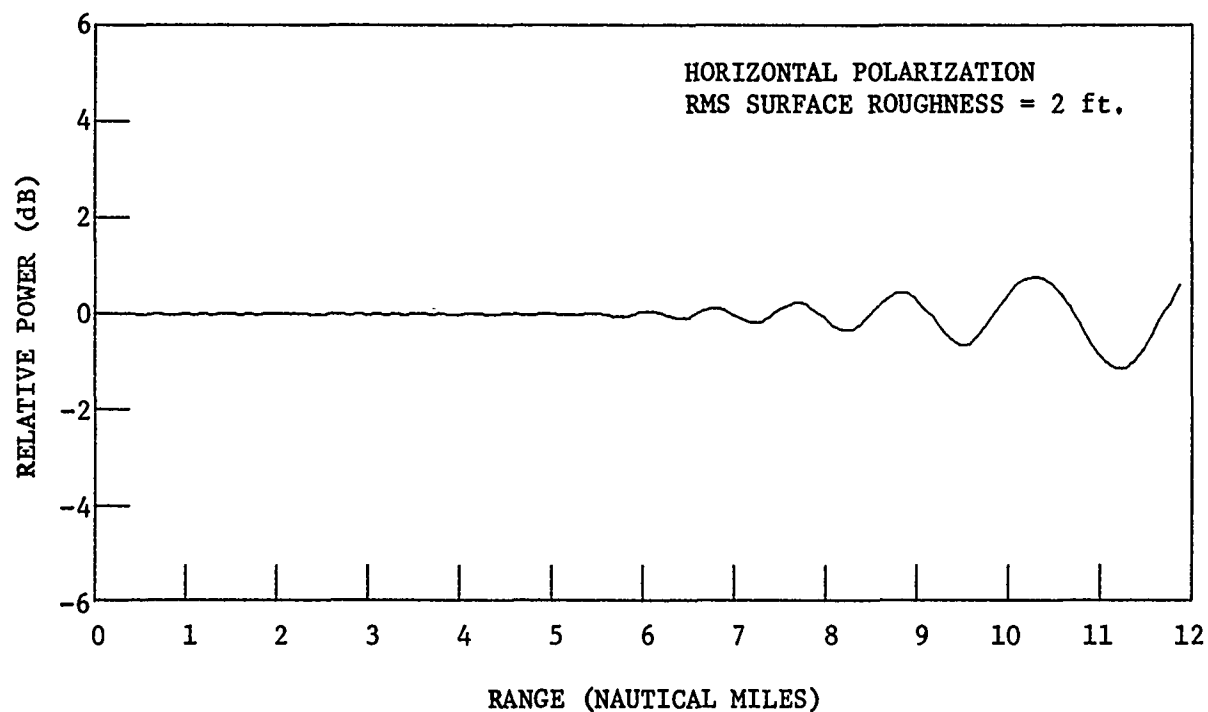


Figure 12. Calculated rf (95 GHz) power incident on a target located 50 ft. above the surface of the sea (rms roughness indicated) shown as a function of horizontal range. Radar beam model chosen has 1.0° beamwidth and 23 dB sidelobes. Radar located 30 feet above water.

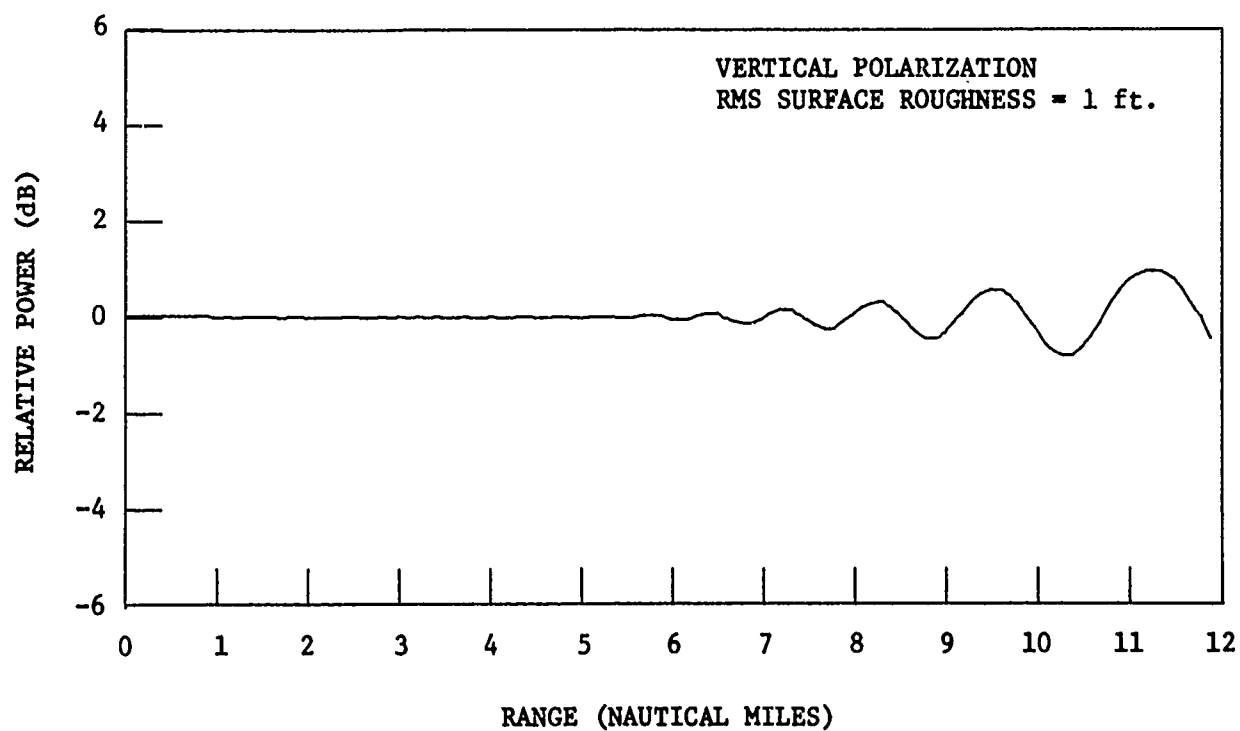
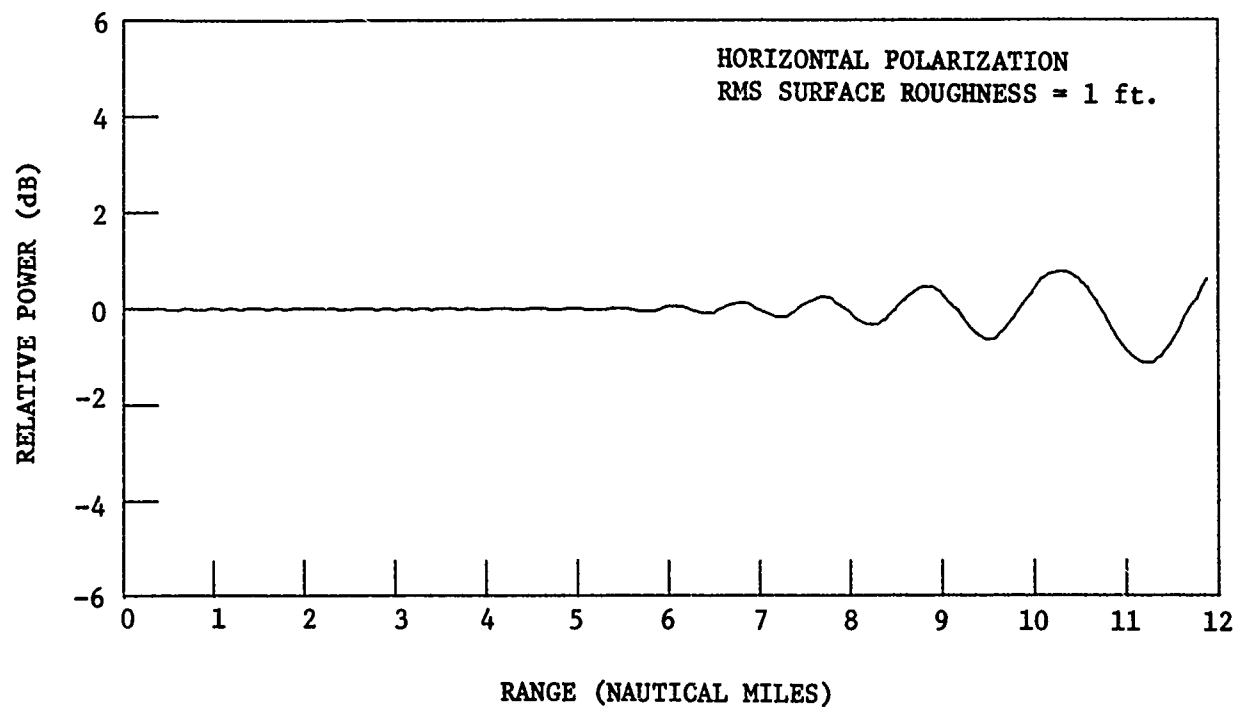


Figure 13. Calculated rf (23 GHz) power incident on a target located 100 ft. above the surface of the sea (rms roughness indicated) shown as a function of horizontal range. Radar beam model chosen has 1.0° beamwidth and 23 dB sidelobes. Radar located 30 feet above water.

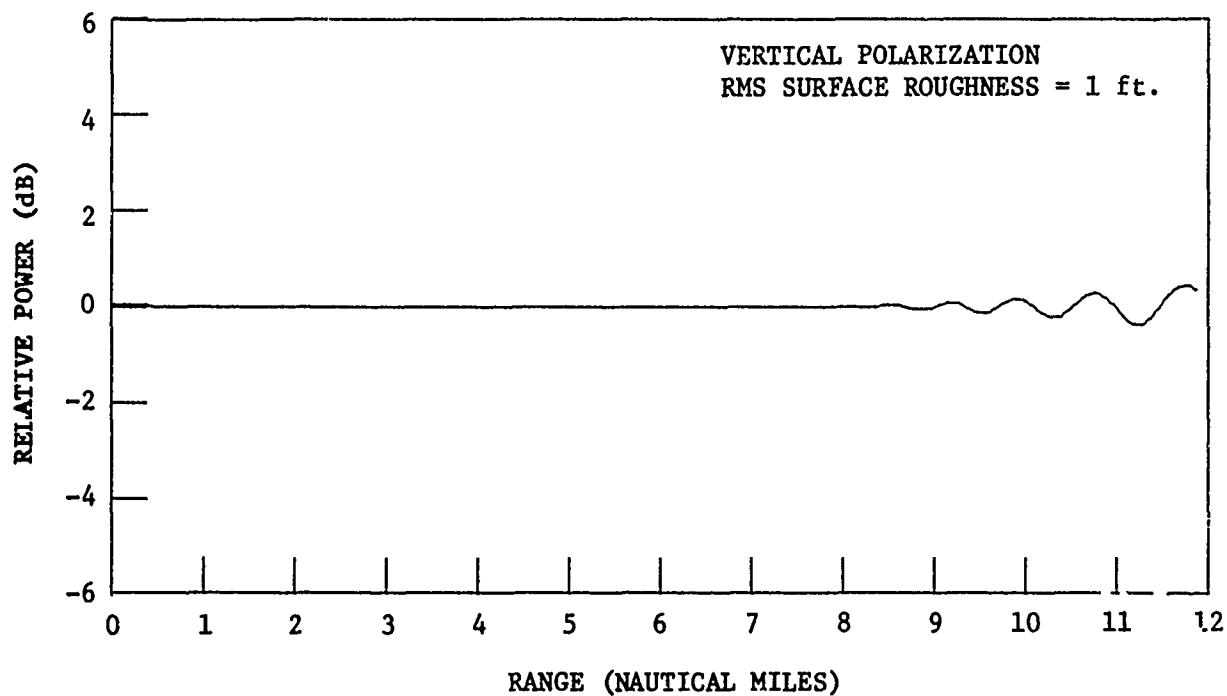
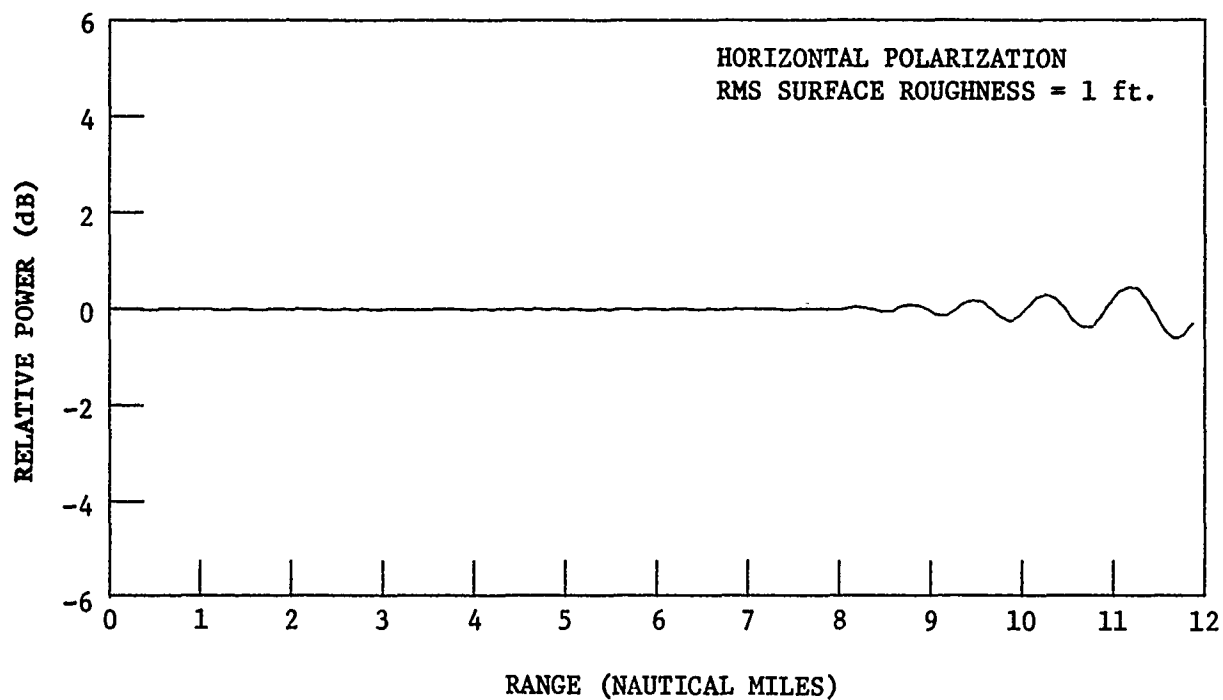


Figure 14. Calculated rf (23 GHz) power incident on a target located 500 ft. above the surface of the sea (rms roughness indicated) shown as a function of horizontal range. Radar beam model chosen has 1.0° beamwidth and 23 dB sidelobes. Radar located 30 feet above water.

B. Atmospheric Attenuation

Water vapor and oxygen are the major causes of atmospheric absorption in the 1.0 to 100 GHz portion of the electromagnetic spectrum. If oxygen or water molecules are isolated, then absorption will occur only at certain frequencies ν because of transitions between bound rotational states. Due to the uncertainty principle there is a small $\Delta\nu$ associated with ν but this is negligible for the case considered here. Other molecular spectra line broadening effects result from collisions between molecules and from Doppler shifts caused by molecular velocities. Of the three causes for line broadening mentioned above, the most prevalent at standard temperature and pressure is that caused by collision between molecules. This is better known as pressure broadening since $\Delta\nu$ is a function of pressure. There is some disagreement among investigators as to the determination of $\Delta\nu$. An equation used to determine the line width for twenty-six oxygen lines grouped around 60 GHz and a single line at 118 GHz is [1]

$$\Delta\nu = 198 P/T \text{ (MHz)} \quad (33)$$

where T is the temperature in $^{\circ}\text{K}$.

The equation most often used for theoretical calculations is the Van Vleck-Weisskopf equation. Hayes [2] used the following form of this equation which is adjusted to good approximation for oxygen and uncondensed water vapor in the region $\nu_{ij} \pm 2\Delta\nu$.

$$\gamma(\nu) = \frac{K\nu^2 p}{T^2} e^{-W/kT} \left[\frac{\Delta\nu}{(\nu_{ij} - \nu)^2 + (\Delta\nu)^2} + \frac{\Delta\nu}{(\nu_{ij} + \nu)^2 + (\Delta\nu)^2} \right] \text{ in dB/km} \quad (34)$$

where

$\gamma(\nu)$ = Van Vleck-Weisskopf absorption coefficient,

K = molecular constant (see Hayes [2], p. 117)

p = partial gas pressure,

T = absolute temperature,

W = energy associated with changes from level i to level j ,

k = Boltzmann's constant,

ν = source frequency,

ν_{ij} = characteristic frequency associated with the energy level change, and

$\Delta\nu$ = linewidth (half-power half-width) of the resonant spectral line.

Figure 15(a) demonstrates the attenuation due to one water absorption line or single line pressure broadening, while Figure 15(b) illustrates the off-peak attenuation due to a closely spaced pair of oxygen lines near 60 GHz. As can be seen from Figure 15, the skirts of a pressure broadened line will contribute to absorption at frequencies considerably above and below $\nu \pm \Delta\nu/2$. For a given temperature and pressure the absorption from each pressure-broadened line at a particular frequency can be summed to give the total absorption at that frequency. If $\gamma(\nu)$ is calculated in the 1 to 100 GHz region then all lines inside and some outside this region must be considered. The shape of this curve is then determined by a particular choice of T and P. In the atmosphere, the values of these parameters will depend on altitude and prevailing weather conditions. For oxygen, the choice of P depends only on altitude, but the choice p for water vapor is dependent on the humidity at that altitude.

Calculations in this report are based on the oxygen and water lines listed in Tables I [3] and II [4], respectively. Attenuation in the 1 to 100 GHz region for oxygen and water vapor were calculated separately using two different forms of the Van-Vleck Weisskopf equation. The results were then summed to produce a plot of total atmospheric attenuation as a function of frequency using $T = 291^\circ\text{K}$, $P = 760$ mm Hg, and relative humidities of 1%, 25%, 50%, 75%, and 100%.

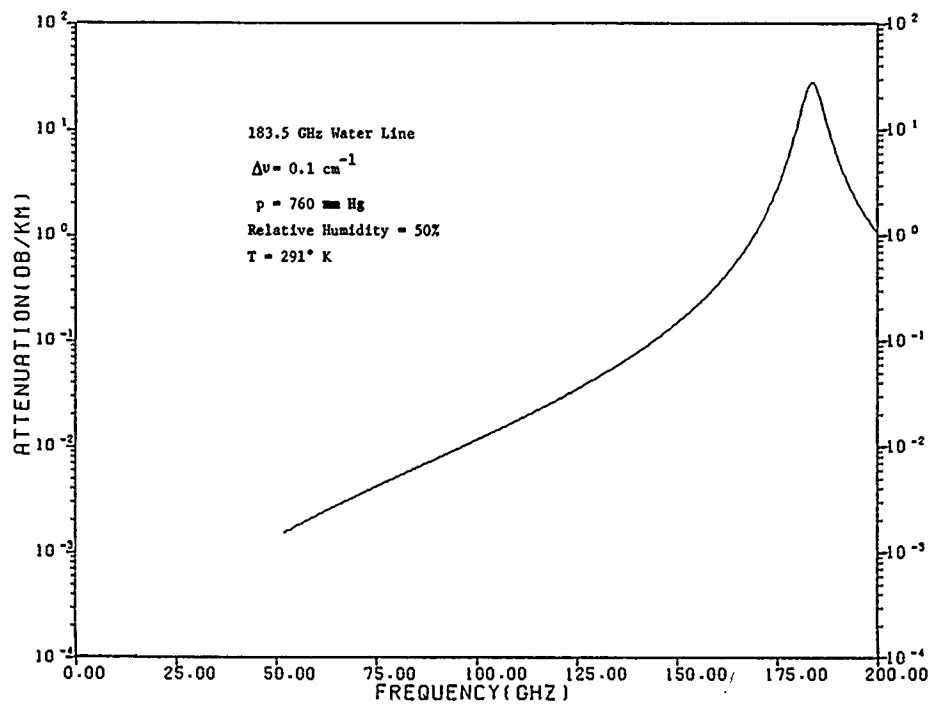
Water vapor calculations were based on a paper by H. H. Theissing and P. J. Caplan [4]. The following form of the Van-Vleck Weisskopf equation was used. $\gamma(\bar{\nu})$ for $(\bar{\nu} = \nu/c)$ off a resonance peak is given by

$$\gamma(\bar{\nu}) = F_1 \sum_p \gamma_o(\bar{\nu}, \bar{\nu}_p) \epsilon_{op}^{(T_o/T_1)-1}, \quad (35)$$

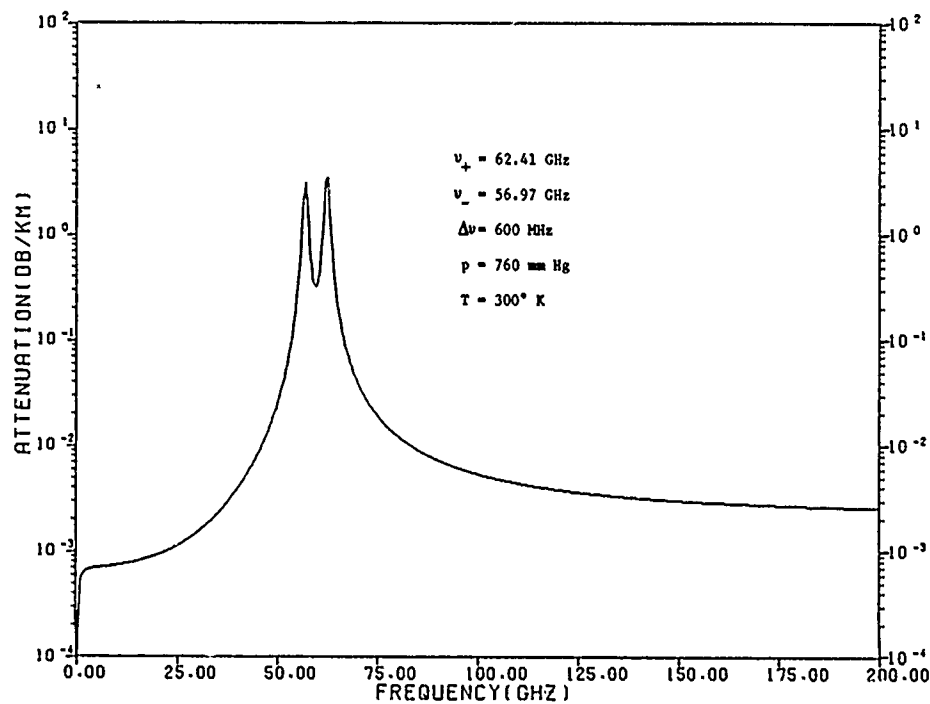
and $\gamma(\bar{\nu})$ for $\bar{\nu}$ on a peak is given by

$$\begin{aligned} \gamma(\bar{\nu}) = F_2 \gamma_{op} \epsilon_{op}^{(T_o/T_1)-1} \\ + F_1 \sum'_p \gamma_o(\bar{\nu}, \bar{\nu}_p) \epsilon_{op}^{(T_o/T_1)-1} \end{aligned} \quad (36)$$

where the prime on the summation indicates that the peak at which $\bar{\nu}$



(a) SINGLE WATER LINE



(b) PAIR OF OXYGEN LINES

Figure 15. Pressure broadening of the attenuation characteristics of a single water line and a pair of oxygen lines.

TABLE I
TRANSITION FREQUENCIES FOR OXYGEN ABSORPTION

N	ν_{N+} (MHz)	ν_{N-} (MHz)
1	56,264.7	118,750.7
3	58,446.9	62,486.7
5	59,591.5	60,306.1
7	60,435.5	59,164.0
9	61,151.3	58,323.6
11	61,800.9	57,612.1
13	62,411.9	56,967.8
15	62,998.5	56,363.1
17	63,568.7	55,783.6
19	64,127.6	55,221.5
21	64,678.2	54,671.6
23	65,222.7	54,130.9
25	65,762.6	53,597.3

TABLE II
WATER VAPOR ABSORPTION FREQUENCIES AND ASSOCIATED DATA

Frequency (GHz)	ϵ_{op}	γ_{op} (dB/km)
22.2	0.110	0.14
183.6	0.510	27.6
325.8	0.210	31.5
380.1	0.350	297
449.4	0.244	308
557.4	0.889	19,600
753.3	0.708	13,200
987.9	0.833	9,710
1097.7	0.509	63,500
1113.9	1.0	19,650
1164.0	0.424	69,400

occurs is excluded and

$$\begin{aligned} F_1 &= \rho P T_0^4 (1 + k\rho/\rho_0) / \rho_0 P_0 T_0^4 (1 + k) \\ &= 1.23 \cdot 10^6 \rho P (1 + 0.0016 \rho) / T^4 \end{aligned} \quad (37)$$

$$F_2 = F_1 (T/T_0) (P_0/P)^2 \quad (38)$$

$$\begin{aligned} \gamma_o(\bar{v}, \bar{v}_p) &= (n_+ + n_-)_o \bar{v}^2 \gamma_{op} / \bar{v}_p^2, \\ (n_{\pm})_o &= \left\{ 1 + \left[\frac{\bar{v} \pm \bar{v}_p}{\Delta \bar{v}_o} \right]^2 \right\}^{-1}. \end{aligned} \quad (39)$$

The symbols in the above water absorption equations are defined below,

$$\epsilon_{op} = \exp \left[- \frac{W_p}{0.695 T_0} \right],$$

W_p = lower energy term of line v_p in cm^{-1} ,

k = constant = 0.012,

P = atmospheric pressure at the height being considered in mm Hg,

P_0 = 760 mm Hg,

(γ_{op}) = absorption peak values of each water line used in dB/km,

ρ = partial water vapor pressure in mm Hg at altitude being considered,

ρ_0 = 7.6 mm Hg,

T = temperature in $^{\circ}\text{K}$ at altitude being considered,

T_0 = ground level temperature

v = frequency in Hz,

$\bar{v} = v/c$ in cm^{-1} (wave number per cm),

v_p = absorption line frequency,

$\bar{v}_p = v_p/c$ in cm^{-1} ,

$\Delta \bar{v}_o = \Delta v_o/c$ in cm^{-1} .

Equations 35 and 36 were evaluated for water vapor attenuation caused by the water lines of Table II, and the result is shown as the dashed line of Figure 16.

Oxygen line attenuation calculation was based on a paper by M. L. Meeks [3] wherein the absorption coefficient is given as

$$\gamma(v, P, T) = C_1 P T^{-3} v^2 \sum \left\{ F_{N+} \mu_{N+}^2 + F_{N-} \mu_{N-}^2 + F_O \mu_{NO}^2 \right\} A_N, \quad (40)$$

where,

$$C_1 = 2.6742 \text{ for } \gamma(\text{in dB/km}) \quad (41)$$

$$C_1 = 0.61576 \text{ for } \gamma(\text{in nepers/km}) \quad (42)$$

$$F_{N\pm} = \frac{\Delta v}{(v_{N\pm} - v)^2 + \Delta v^2} + \frac{\Delta v}{(v_{N\pm} + v)^2 + \Delta v^2}, \quad (43)$$

$$F_O = \frac{\Delta v}{v^2 + \Delta v^2}, \quad (44)$$

$$\mu_{N+}^2 = \frac{N(2N+3)}{N+1}, \quad \mu_{N-}^2 = \frac{(N+1)(2N-1)}{N}, \quad (45)$$

$$\mu_{NO}^2 = \frac{2(N^2 + N + 1)(2N + 1)}{N(N + 1)}, \quad (46)$$

$$A_N = \exp \left[-C_2 N(N + 1)/T \right] \quad (47)$$

$$C_2 = 2.0684 \quad (48)$$

$$\Delta v = \alpha P \left[0.21 + 0.78\beta \right] (300/T)^{0.85}. \quad (49)$$

The symbols used in the above equations are defined below.

γ = absorption coefficient (in this case for oxygen) in dB/km,
 v = frequency in GHz,

- ν_{N+} = transition frequencies corresponding to $N + 1$ and $N - 1$
 energy state transitions
 P = atmospheric pressure in mm Hg at altitude being considered
 T = temperature in $^{\circ}\text{K}$ at altitude being considered
 N = odd rotational quantum numbers
 $\Delta\nu$ = line-broadening parameter = 600 MHz

Equation 40 was evaluated for the oxygen lines listed in Table I and the results are shown as the solid curve in Figure 16. Equations 35, 36 and 40 were then summed to find the total atmospheric attenuation in the region 1-100 GHz due to the absorption lines listed in Tables I and II. This absorption is plotted in dB/km for relative humidities of 1%, 25%, 50%, 75%, and 100% in Figure 17. The present calculations were carried out for atmospheric conditions at sea level. If it is desired to perform the calculations at higher altitudes then the atmosphere must be divided into a number of discrete layers, with each layer having its associated temperature, pressure and humidity. The attenuations for a typical humidity (50%) and several frequencies of interest are tabulated in Table III below.

TABLE III
CALCULATED ATMOSPHERIC ATTENUATION FOR 50%
RELATIVE HUMIDITY AND A NUMBER OF TYPICAL FREQUENCIES

<u>Frequency (GHz)</u>	<u>Attenuation (dB/km)</u>
10	0.01
16	0.028
23	0.160
35	0.050
46	0.120
70	0.380
95	0.140

C. Rain and Fog Attenuation

As shown in the previous section, rf energy is absorbed by moisture content in the atmosphere. Additionally, energy is attenuated and scattered by precipitation such as rain, snow and hail. Thick fog can also have a significant attenuation effect.

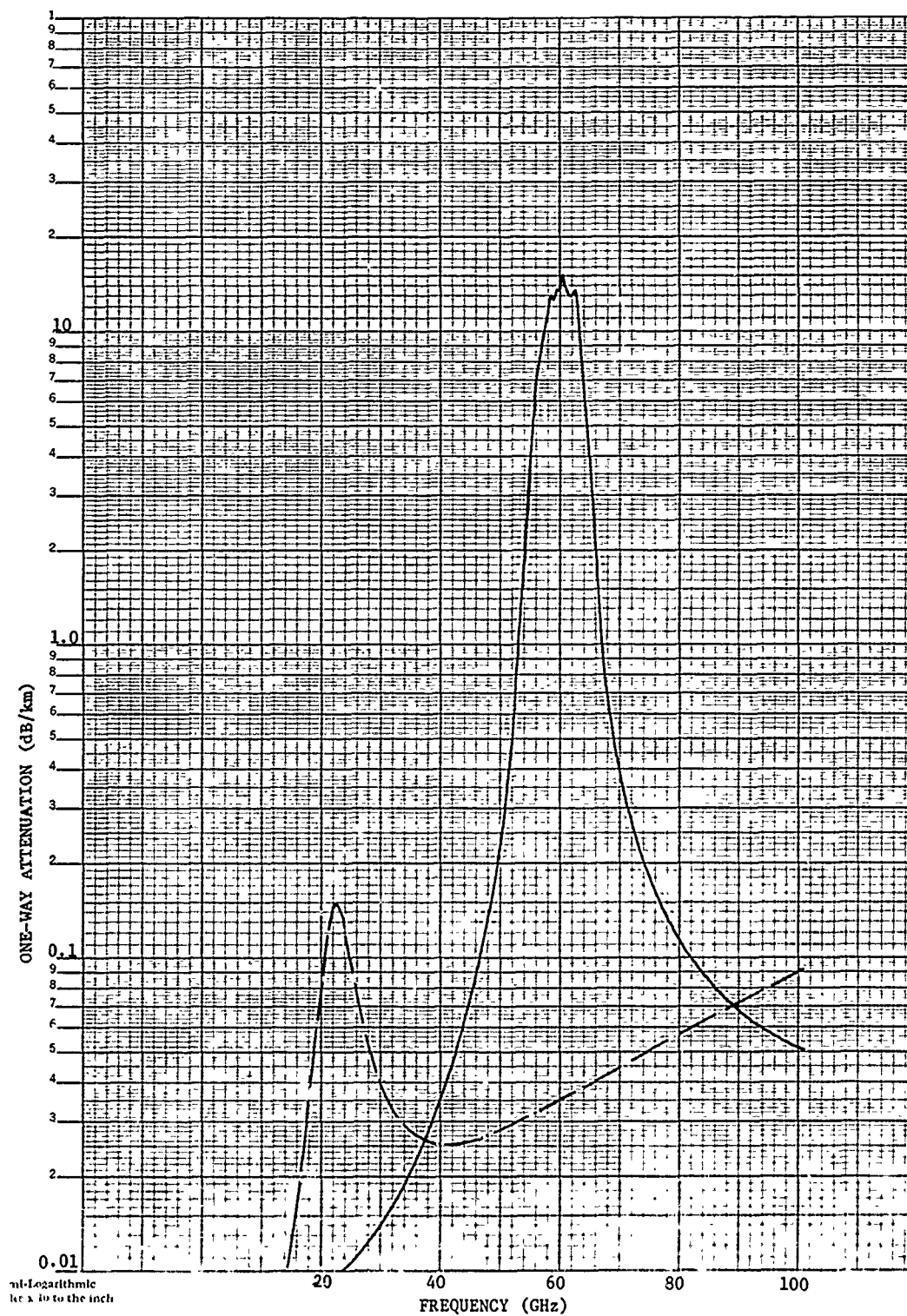


Figure 16. Total atmospheric absorption due to water vapor alone (dashed) and oxygen only (solid).

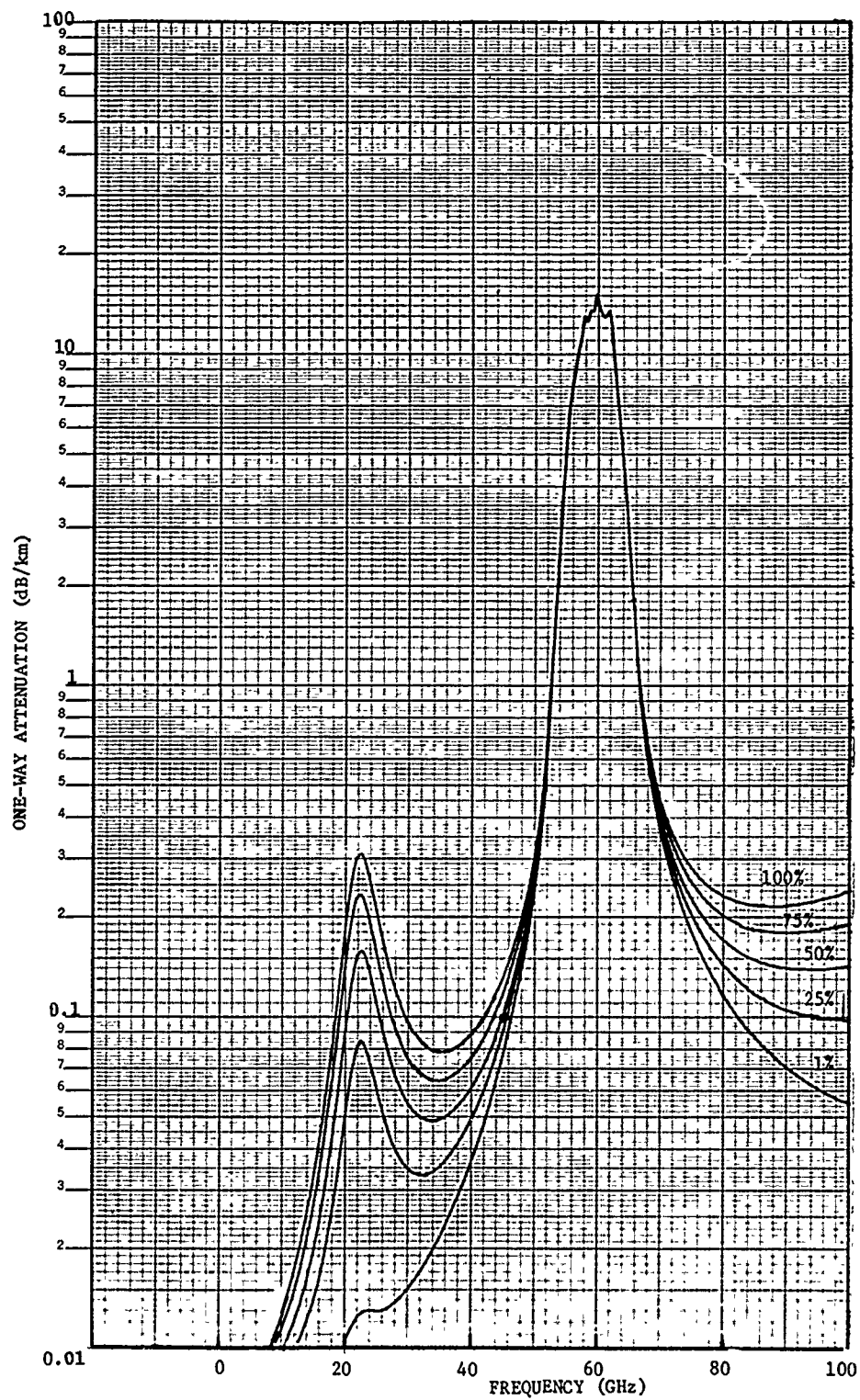


Figure 17. Total atmospheric attenuation due to both water and oxygen for several different relative humidities.

A survey by Dudzinsky [5] indicates that it is probably only at shorter wavelengths in the millimeter region that the attenuation by falling snow (particularly wet snow) and hail might be expected to be comparable to that produced by moderate rain having an equivalent liquid water precipitation rate. Thus, for frequencies below about 100 GHz, the attenuation caused by snow and hail can generally be expected to be significantly less than the rainfall attenuation for most regions of the earth and can therefore be neglected.

Dudzinsky [5] also states that typical fogs have small water content and, therefore, cause negligible attenuation when compared to rain. In those rare instances of extremely dense fog, the resulting attenuation is comparable to that produced by moderate rain (2.5 to 5.0 mm/hr).

In order that the effect of rainfall be accounted for in a uniform manner across the millimeter-wave region, a particular theoretical model was chosen. This model, which was originally developed by Ryde and Ryde [6] and included in Goldstein's [7] writings on atmospheric attenuation, is illustrated in graphic form in Figure 18. In this figure, the one-way attenuation is given in dB/km as a function of wavelength for a number of typical rain rates and fog densities.

Due to a recent broad survey [12] of this phenomenon by EES personnel, it was recognized that a large amount of rainfall attenuation data has been recorded since those early writings; consequently, the theoretical numbers can be compared with measured ones. Personnel of the Martin Marietta Company have developed the following simple mathematical relationship [8] for approximating the Goldstein curves,

$$\alpha(R,f) = .628 \times 10^{-6} \left[\frac{f}{1 + f/17} \right]^{5.37} R^m$$

where

$$m = 1.182 - (4.622 \times 10^{-3}) f^{1.018}.$$

R is the rain rate in mm/hr. and f is the frequency in GHz. This equation was evaluated for a 4 mm/hr. rain rate and several frequencies of interest

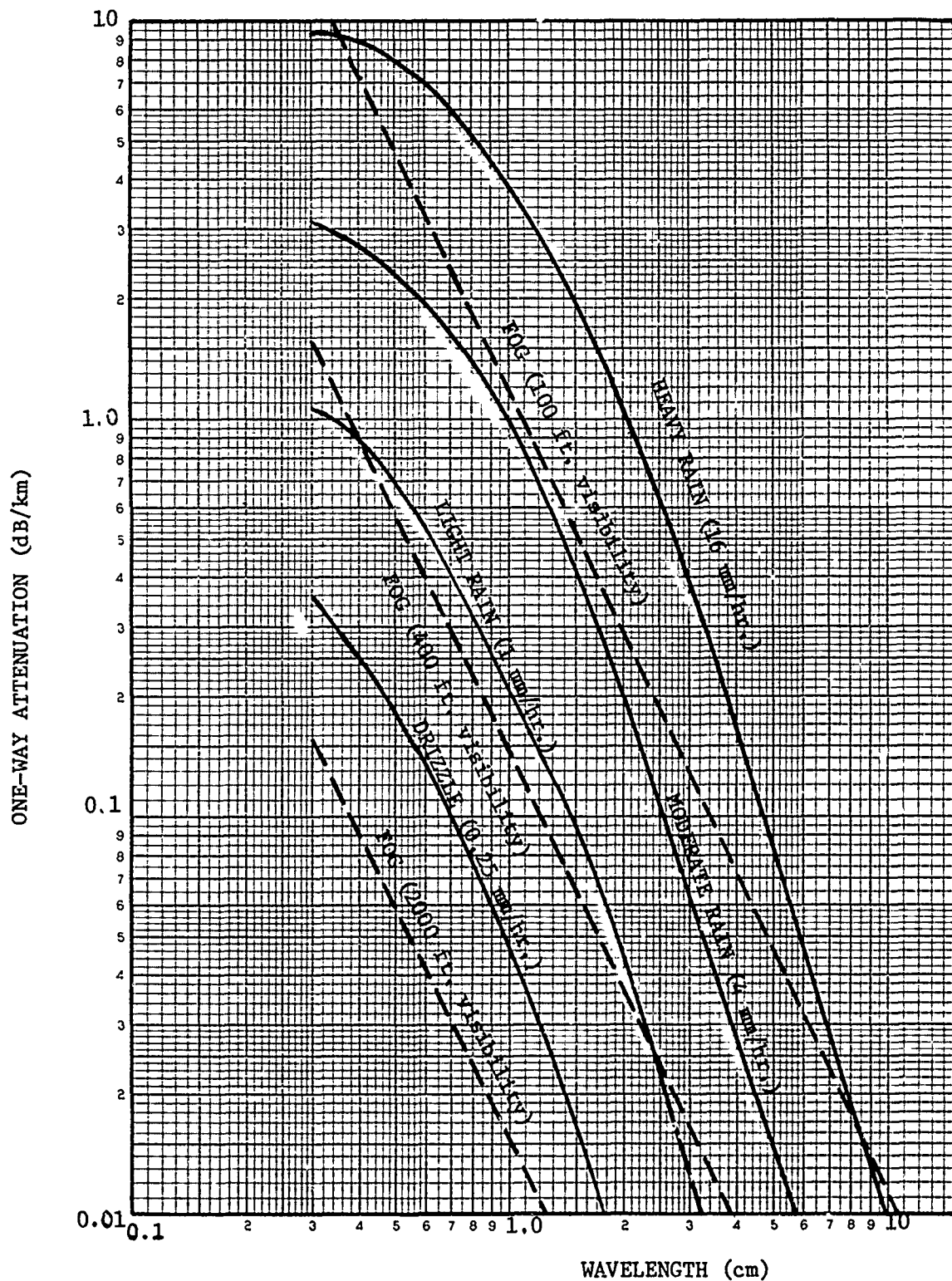


Figure 18. Calculated (by Goldstein) attenuation of electromagnetic energy by rain and fog presented as a function of wavelength.

and the results are listed in Table IV. De Bettencourt [9] has compiled a large amount of measured data and has developed an empirical table for determining attenuation over a broad range of frequencies and rain rates. De Bettencourt's values for 5 mm/hr. rain and several frequencies of interest are tabulated in Table IV. Norden [10] fitted the following equation to the measured data of several researchers.

$$\alpha = KR^P \text{ dB/km.}$$

$$\begin{aligned}\alpha(15 \text{ GHz}) &= 0.039 R^{1.108} \\ \alpha(35 \text{ GHz}) &= 0.240 R^{1.0177} \\ \alpha(70 \text{ GHz}) &= 0.750 R^{.8062} \\ \alpha(90 \text{ GHz}) &= 0.980 R^{.7412}\end{aligned}$$

These equations were evaluated for a rain rate of 4 mm/hr. and listed in Table IV. Richard and Kammerer [11] have also developed empirical relations for the smaller wavelength region. These equations are given below and their values at 4 mm/hr. are tabulated in Table IV.

$$\begin{aligned}\alpha(70 \text{ GHz}) &= 0.24 R^{1.05} \\ \alpha(95 \text{ GHz}) &= 0.52 R^{.86}\end{aligned}$$

It can be noted from Table IV that the theoretical attenuation constants are slightly higher than the measured values but are nevertheless representative of the variations with frequency and rain rate. Consequently, the Goldstein curves were used in signal-to-noise calculations throughout this report.

TABLE IV.

COMPARISON OF THEORETICAL AND MEASURED RAINFALL
ATTENUATION AS A FUNCTION OF FREQUENCY

Frequency (GHz)	One-Way Attenuation (dB/km)				
	Goldstein [7]	Martin Marietta Model [8]	de Bettencourt* Empirical Data [9]	Norden Model [10]	Richard and Kammerer [11]
9.3	0.051	0.046	.142 (10 GHz)		
16.5	0.25	0.253	.337 (15 GHz)	0.181 (15 GHz)	
23	0.58	0.574	.581 (20 GHz)		
35	1.27	1.23	1.14 (30 GHz)	1.11	
46	1.80	1.76			
70	2.60	2.51	2.85 (60 GHz)	2.29	1.03
95	3.10	2.79	4.56 (100 GHz)	2.73 (90 GHz)	1.71

* 5 mm/hr. rain rate

IV. SYSTEM CALCULATIONS

A. Target Characteristics

The targets of interest on this study may be considered to follow three distinct paths when flying against the radar (see Figure 19).

Type A targets (path I in Figure 19) fly at a very low constant altitude (possibly as low as ten feet over the water) from launch to impact. For a typical radar position on a ship, this trajectory remains below 0° elevation angle during the entire flight. This target can have a velocity as high as 1200 ft./sec.

Type B targets (paths II and III) approach the ship at elevation angles below 1° , exhibit a rapid vertical climb at a range between two and three nautical miles, and dive for the ship from elevation angles as high as 45° . Target velocities for this type are in the range 850 to 900 ft./sec.

Type C targets (path IV) are air launched and may be considered to approach the ship radially with an elevation angle between 0° and 20° . This threat may have velocities as high as 2200 ft./sec.

Although the present study is concerned primarily with the acquisition mode, the requirements on acquisition are geared directly to the tracking capabilities and requirements. Consequently, the tracking scenario will be addressed first. Based on the trajectories described above, an elevation section of the threat volume may be drawn as shown in Figure 20(a). The transition region where elevation coverage requirements change from 1° to 45° is shown at 3 nautical miles. This range should be slightly larger if it is taken to be the hand-off point between acquisition and tracking systems, since it is undesirable to hand off in regions of high target angular acceleration.

The tracker must be capable of keeping the target within view, even during the vertical climb, from the time track is established until intercept. Also in the case of multiple targets, it may be necessary for one tracker to track two separate targets that are widely separated in angle. For these reasons, it is desirable to know the target angular velocity rates. The physical distance S (see Figure 20(b)) that the target moves when traversing on angle θ at a range R is

$$S = R\theta. \quad (50)$$

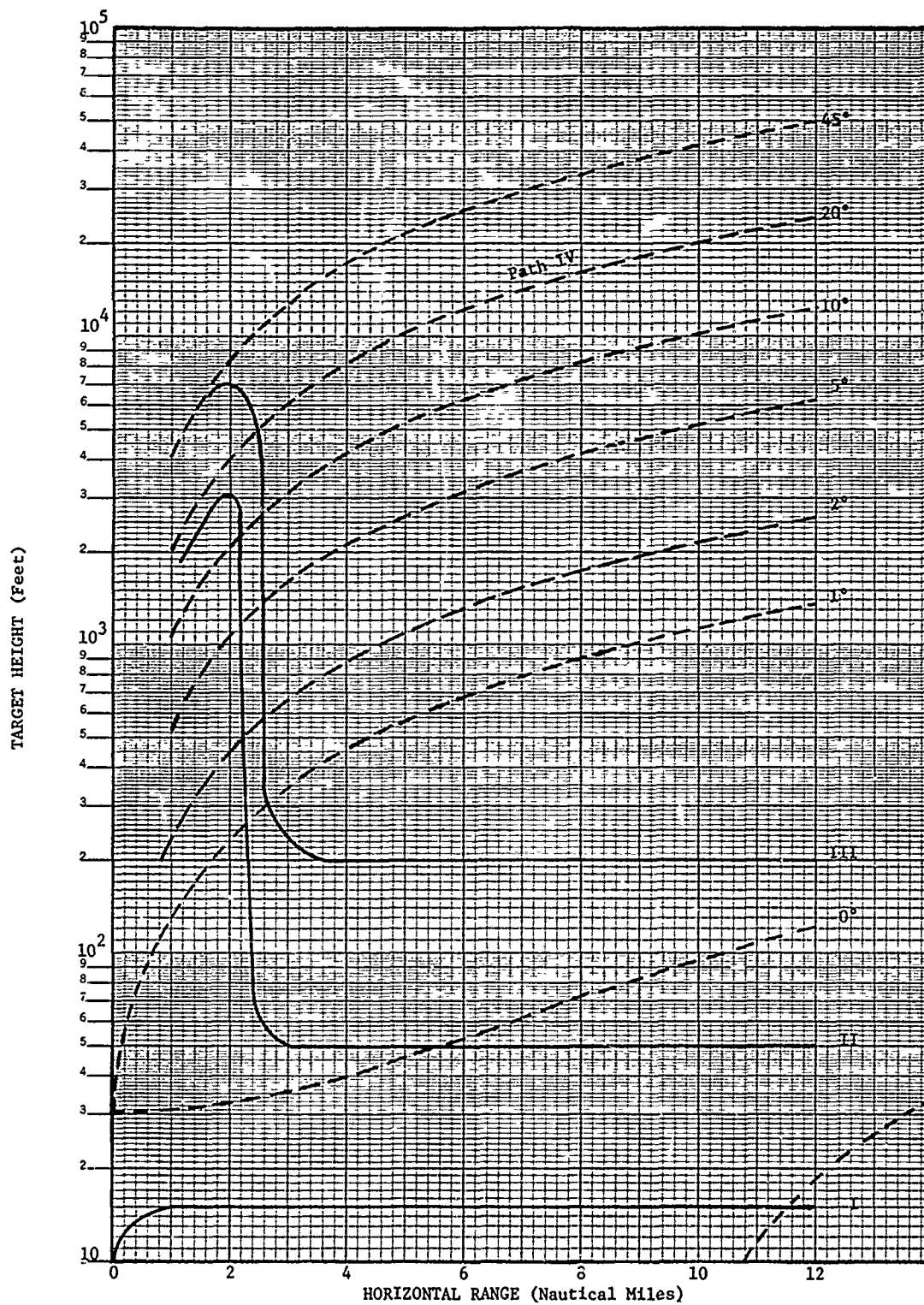
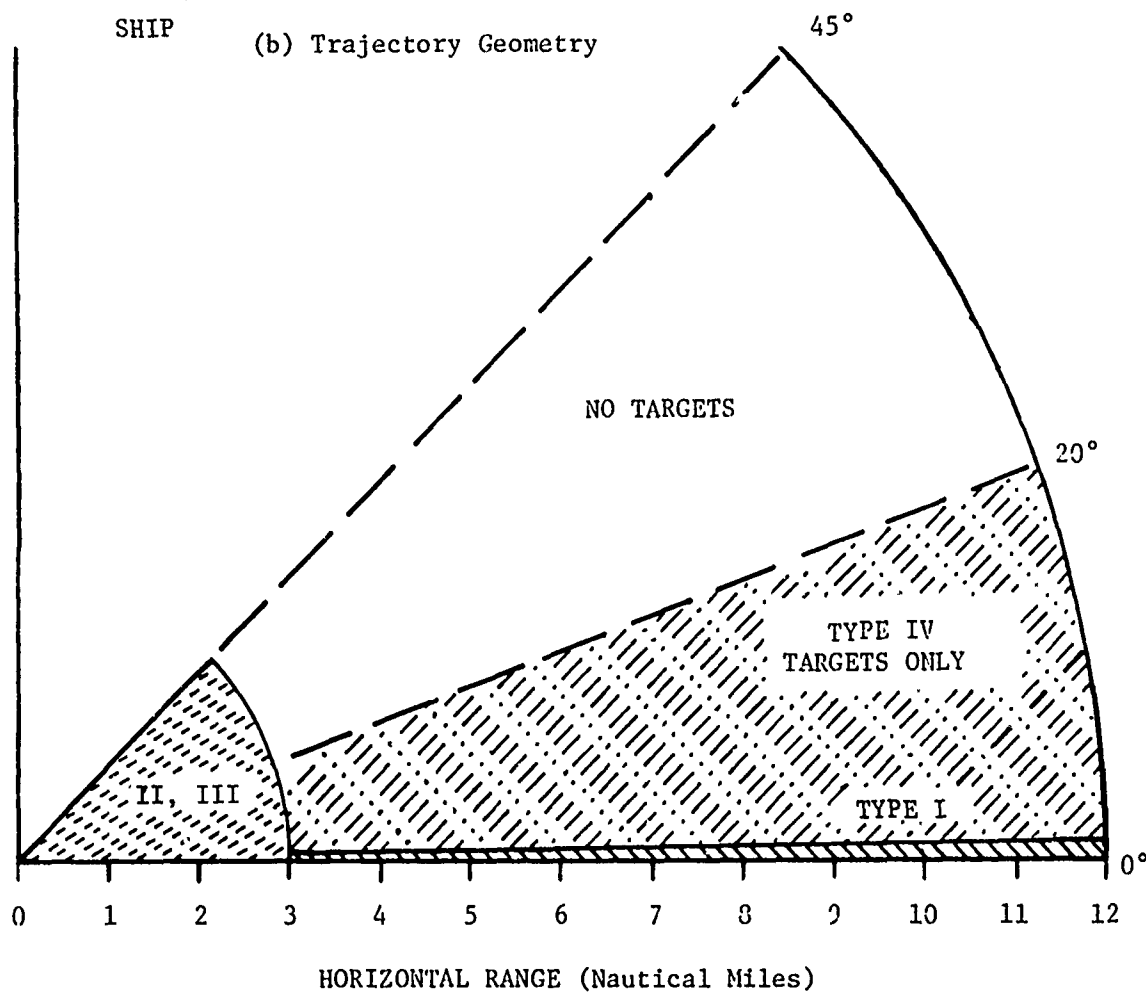
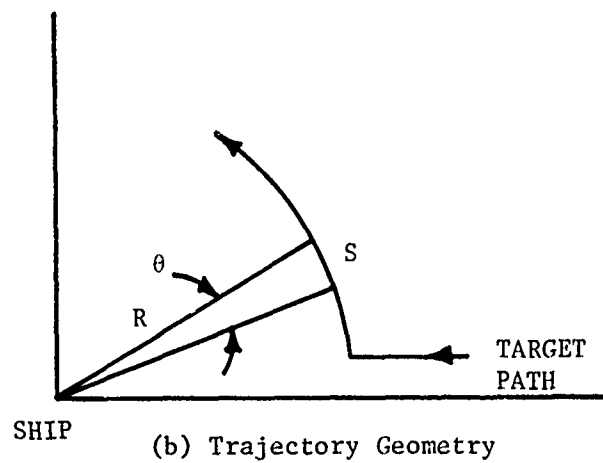


Figure 19. Typical threat trajectories.



(a) Section Through Treat Volume

Figure 20. Geometry of target trajectories.

The angular velocity of the target is then

$$V = \dot{S} = R\dot{\Theta} \quad (51)$$

Then,

$$\dot{\Theta} = \frac{V}{R} \quad (52)$$

A target velocity of 1200 ft./sec. at a range of 2.5 nautical miles (15,190 feet) corresponds to an angular velocity of

$$\dot{\Theta} = \frac{1200}{15,190} = .079 \text{ rad/sec} = 4.53^\circ/\text{sec}. \quad (53)$$

B. Tracking Considerations

1. Track Schemes

One tracking concept which has been considered is the raster scanning of a pencil beam across the 45° by 45° sector. This could be accomplished either by (1) continuously moving the beam in azimuth at one elevation level then shifting to another elevation and repeating the process, or by (2) sequentially moving the beam through the discrete positions shown in Figure 21. If the beams in this figure cross at their 3-dB points, then β is the half-power beamwidth and will be taken to be the value (1.11°) calculated by APL for this application.

N is then the number of beams per line where a line is defined as any of the horizontal rows shown.

$$N\beta = 45^\circ \quad (54)$$

$$N = \left[45^\circ / 1.11^\circ \right] + 1 = 41 \quad (55)$$

The number of beams in any vertical column is also equal to N; therefore, the total number of beams required to fill the window is

$$N^2 = 1681 \quad (56)$$

If a maximum unambiguous range of 5 nmi. is deemed sufficient* then a PRF of 15 kHz may be used. This corresponds to a time-between-pulses

* See calculations in next section.

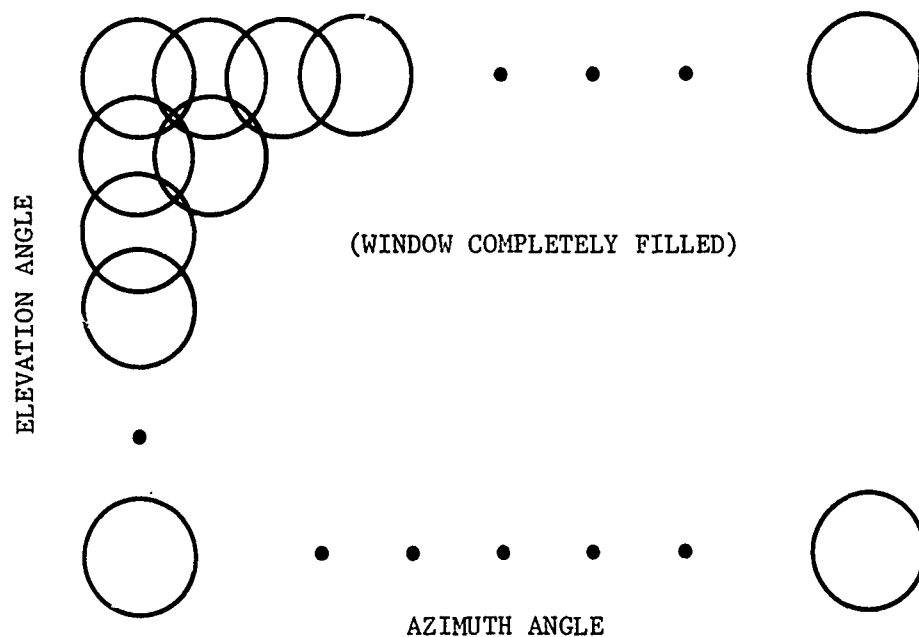


Figure 21. Solid angular window filled with discrete overlapping beams.

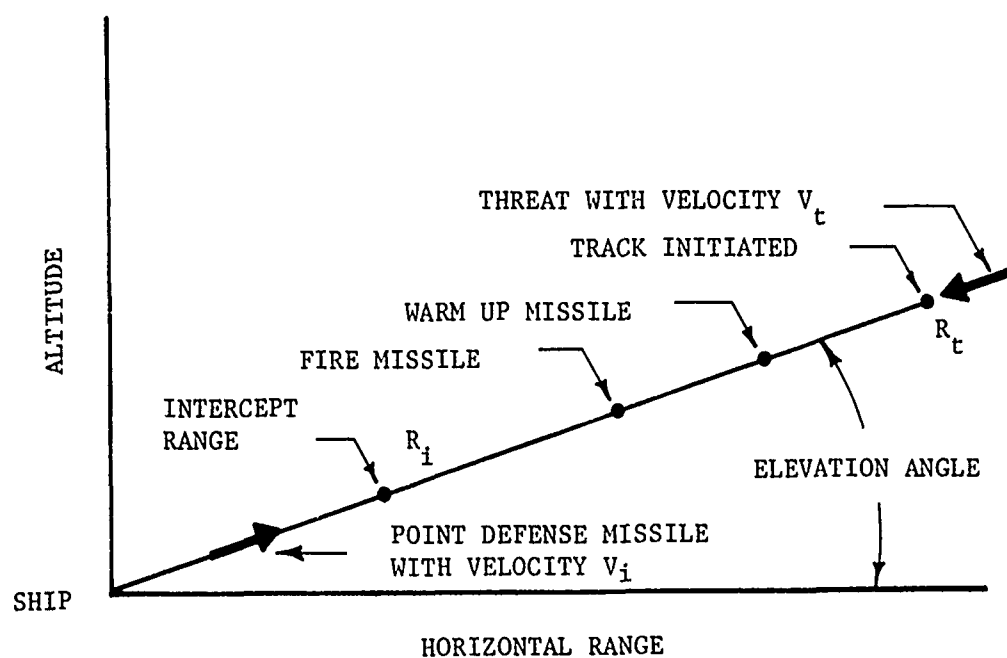


Figure 22. Geometry of point defense missile intercepting threat vehicle.

of 67 microseconds or a total beam-on-target (5 pulses) time of 333 microseconds. The total time to scan the window is then

$$T_s = N^2 \Delta t \quad (57)$$

where Δt is the beam time at each position or 333 microseconds.

$$T_s = (1681) (333 \times 10^{-6}) = .56 \text{ sec.} \quad (58)$$

It is interesting at this point to investigate the number of track points obtained from a raster scan tracker having the parameters derived above. If the target rises at $4.53^\circ/\text{sec.}$ (sec. Equation (53)), then it will require 9.93 sec. to climb to the full 45° elevation angle. The worst case situation occurs when the target begins its climb immediately after the raster beam begins to ascend. Table V gives a time history of the location of both target and beam thereafter, and it is seen that 17 detections are obtained.

It is felt that a track-while-scan system utilizing two orthogonally scanning fan beams would be the best choice if the lower gain of the fans can be tolerated. Attention will be given to this factor in a later calculation.

2. Minimum Track Lock-on Range

From the onset it was known that available peak powers and environmental attenuation created severe limitations on detection ranges; consequently, it is desirable to minimize the range at which acquisition and track must be established. It is the purpose of this section to determine the minimum range at which a definite track must be established in order to intercept the incoming target (see Figure 22) before it hits. The following parameters of interest are defined here.

R_t = Range to track lock-on

R_i = Intercept range (missile from ship hits target)

V_t = Target velocity

V_i = Interceptor missile velocity

t_o = Missile warm-up time

t_i = Missile flight time

t_1 = Track time before missile is fired from ship.

TABLE V

TIME HISTORY OF ELEVATION LOCATION OF
TARGET IN VERTICAL CLIMB AND RASTER
SCANNING PENCIL BEAM

<u>Time (Seconds)</u>	<u>Beam Angle (°)</u>	<u>Target Angle (°)</u>
0	0 ⁺	0 ⁻
.28	22.5	1.27
.56	45,0	2.54
.84	22.5	3.81 — Detection (1)
1.12	45,0	5.07
1.4	22.5	6.34 — Detection (2)
1.68	45,0	7.61
1.96	22.5	8.88 — Detection (3)
2.24	45,0	10.15
2.52	22.5	11.42 — Detection (4)
2.8	45,0	12.68
3.08	22.5	13.95 — Detection (5)
3.36	45,0	15.22
3.64	22.5	16.49 — Detection (6)
3.92	45,0	17.76
4.2	22.5	19.03 — Detection (7)
4.48	45,0	20.29
4.76	22.5	21.56 — Detection (8)
5.04	45,0	22.83
5.32	22.5	24.1
5.60	45,0	25.37 — Detection (9)
5.88	22.5	26.64
6.16	45,0	27.9 — Detection (10)
6.44	22.5	29.17
6.72	45,0	30.44 — Detection (11)
7.0	22.5	31.71
7.28	45,0	32.98 — Detection (12)
7.56	22.5	34.25
7.84	45,0	35.52 — Detection (13)
8.12	22.5	36.78
8.4	45,0	38.05 — Detection (14)
8.68	22.5	39.32
8.96	45,0	40.59 — Detection (15)
9.24	22.5	41.86
9.52	45,0	43.13 — Detection (16)
9.8	22.5	44.39
10.08	45,0	45.66 — Detection (17)

The following sequence of steps yields the desired relation between initial track time and intercept range.

- (1) Track is initially established at R_t .
- (2) Radar tracks target for t_1 seconds. Two seconds is probably adequate (20 track points at 10 scans/sec.)
- (3) Positive track (decision made that a missile should be fired) is identified at $R_t - t_1 V_t$
- (4) Missile warms up for t_o seconds while track continues.
- (5) Missile is fired. Target is then located at $R_t - V_t(t_1 + t_o)$.
- (6) Missile flies for t_i seconds and hits target at range R_i where $R_i = V_i t_i$.
- (7) Target and missile are both at

$$R_i = R_t - V_t(t_1 + t_o + t_i) \quad (59)$$

$$R_i = R_t - V_t(t_1 + t_o + R_i/V_i), \text{ or} \quad (60)$$

$$R_t = R_i (1 + V_t/V_i) + V_t(t_1 + t_o) \quad (61)$$

V_i may always be assumed to be 2000 ft./sec. and V_t may be either 2200 or 1200 ft./sec. depending on the class of threat present. Equation (61) is plotted in Figure 23 for each of these velocity values and also for the case of 5 seconds warm-up and no warm up (i.e., warm-up is initiated during acquisition). These four possibilities are designated as Cases 1 through 4.

Case (1) $V_t = 2200, t_o = 5$

Case (2) $V_t = 2200, t_o = 0$

Case (3) $V_t = 1200, t_o = 5$

Case (4) $V_t = 1200, t_o = 0$

It may be noted from Figure 23 that the worst case (three-mile intercept range) in terms of track range occurs at approximately 8.9 nautical miles for the fastest target and a missile warm-up (5 sec.) after track is established. If a hit range (away from ship) of 1 nmi. is satisfactory to system designers, then a worst case track range of 4.7 nmi. is required. If the missile can be warmed up during acquisition, then a track range of 2.1 nmi would be acceptable. Due to the diverse

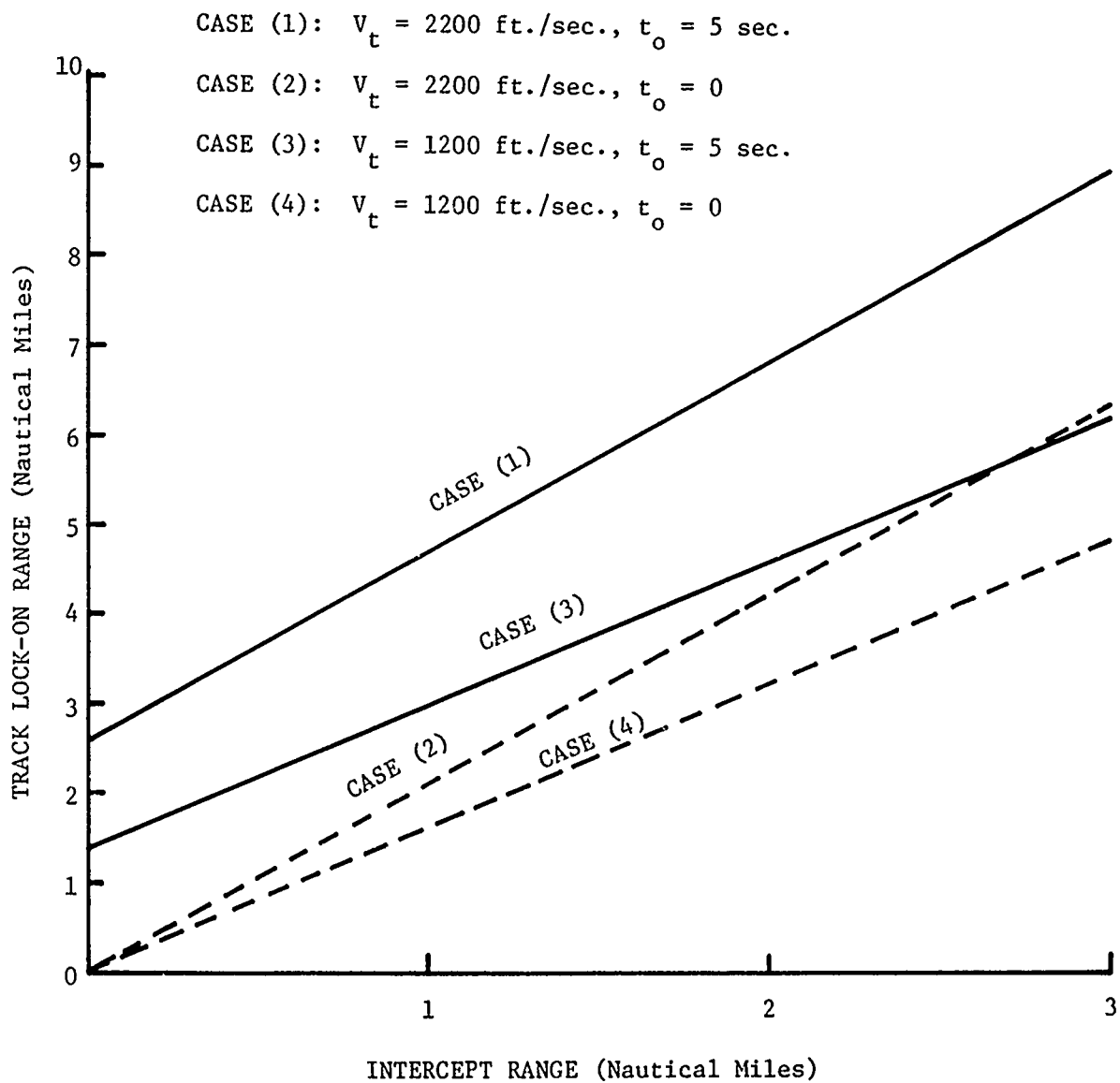


Figure 23. Calculated required lock-on range as a function of intercept range for the threat velocities and missile warm up times shown.

possibilities which may occur in the target's path between 0 and 2.5 nmi. of range, it is recommended that track be established at least before the target is within three miles of the ship.

3. Track System Signal-To-Noise Ratios

It is of interest at this point to investigate the signal-to-noise ratio which results from a track-while-scan system consisting of two orthogonally swept fan beams. This ratio may be calculated from the following equation.

$$S/N = 10 \log \left[\frac{P_t G^2 \lambda^2 \sigma n E(n)}{(4\pi)^3 KTB R^4} \right] - N_f - L - L_a \quad (62)$$

where,

- P_t = Transmitter power = 65 kW at 23 GHz
= 125 kW at 46 GHz
- λ = Wavelength = .013 meter at 23 GHz
= .0065 meter at 46 GHz
- G = Antenna one-way gain
- σ = Target radar cross section = 1 sq. m.
- n = Number of pulses integrated = 6
- $E(n)$ = Efficiency of integrator = 0.8
- k = Boltzman's constant
- T = Absolute temperature
- kT = -204 dB
- N_f = Receiver noise figure = 10 dB
- L = Two-way microwave components losses = 9 dB
- L_a = Atmospheric losses = $2\alpha R$
- α = 0.2 dB/km for both frequencies
- $(4\pi)^3$ = 33 dB
- B = System bandwidth = $1.2/\tau$ = 67.8 dB where
- τ = 0.2 μ sec.

This Equation may be rewritten (in dB) as

$$S/N = P_t + 2G + 2\lambda + 0 + 6.8 - 33 + 204 - 67.8 - 10 - 9 - R^4 - 2\alpha R, \quad (63)$$

$$S/N = P_t + 2G + 2\lambda - R^4 - 2\alpha R + 91 \quad (64)$$

Choosing a frequency then eliminates two of the variables.

$$\underline{f = 23 \text{ GHz}}$$

$$S/N = 2G - R^4 - 2\alpha R + 101.3 \text{ dB} \quad (65)$$

$$\underline{f = 46 \text{ GHz}}$$

$$S/N = 2G - R^4 - 2\alpha R + 98.2 \text{ dB} \quad (66)$$

The major factor which remains unspecified is the gain. The procedures for calculating gain from either the aperture illumination or the pattern shape are non-trivial; however, a good rule of thumb which yields approximate answers is given below.

$$\text{Gain} = 30,000/\Theta \Phi \quad (67)$$

where Θ and Φ are the half-power beamwidths. Another equally expedient relation is that which relates beamwidth to aperture dimension D.

$$B = 65\lambda/D \quad (68)$$

It is known from APL calculations [13] that a beamwidth on the order of 1° is needed. It is also obvious that the signal-to-noise ratio is inversely proportional to the beamwidth; however, energy on target and maximum allowable aperture dimensions restrain one from designing for arbitrary S/N. For example, an aperture dimension on the order of 42 inches is felt to be a maximum. This value yields a beamwidth of $.79^\circ$ from Equation (68) at 23 GHz.

It is very desirable from an antenna standpoint to be able to cover the required $45^\circ \times 45^\circ$ window with a single pair of orthogonal fans. This means that each fan ($0.79^\circ \times 45^\circ$) would sweep the entire window, one each moving in the horizontal and vertical planes. Equation (67) predicts a gain of

$$G = \frac{30,000}{45 \times 0.79} = 843.9 \text{ (29.3 dB)} \quad (69)$$

Several values of S/N are calculated from Equation (65) using this gain and a number of ranges and are listed in Table VI below.

TABLE VI
CALCULATED SIGNAL-TO-NOISE RATIO AT
23 GHz FOR ANTENNA GAIN OF 29.3 dB

<u>Range (nmi)</u>	<u>S/N (dB)</u>
1	28.6
2	15.8
3	8.0
4	2.3
5	-2.3
6	-6.2
7	-9.6
8	-12.7
9	-15.4

Table VI shows that this system provides acceptable S/N only for ranges less than about 2.5 nmi. Figure 23 shows that this is totally unacceptable for Case (1) situations (fastest target and warm-up after track lock on) since this value of detection range corresponds to zero intercept range. If warm-up can be accomplished during acquisition (Case (2) in Figure 23), then the 2.5 nmi detection range corresponds to an intercept at 1.2 nmi. Due to the nature of the target's movement in the ranges 2-3 nmi., it is felt that this system is unacceptable. If the required window is covered by four pairs of fan beams each $22.5^\circ \times 0.79^\circ$ (see Figure 24) with each scanning a $22.5^\circ \times 22.5^\circ$ window, then the gain of each beam will go up by 3 dB and the S/N values of Table VI will increase by 6 dB. This means that the S/N value is marginal at 4 nmi and completely satisfactory at 3 nmi. The 3 nmi. detection range corresponds to intercept ranges of 0.2 and 1.43 nmi for warm-up during (Case (1)) and before (Case (3)) track, respectively. Consequently, the need for missile warm-up during acquisition is apparent.

One is then behooved to fix the aperture dimension at its maximum, go to the higher frequency (46 GHz), and take advantage of the narrower beamwidths and higher gains. However, before doing so, it is advisable to determine the minimum beamwidth allowable so that a sufficient number of pulses (assume 5) are placed on each target. If a maximum unambiguous

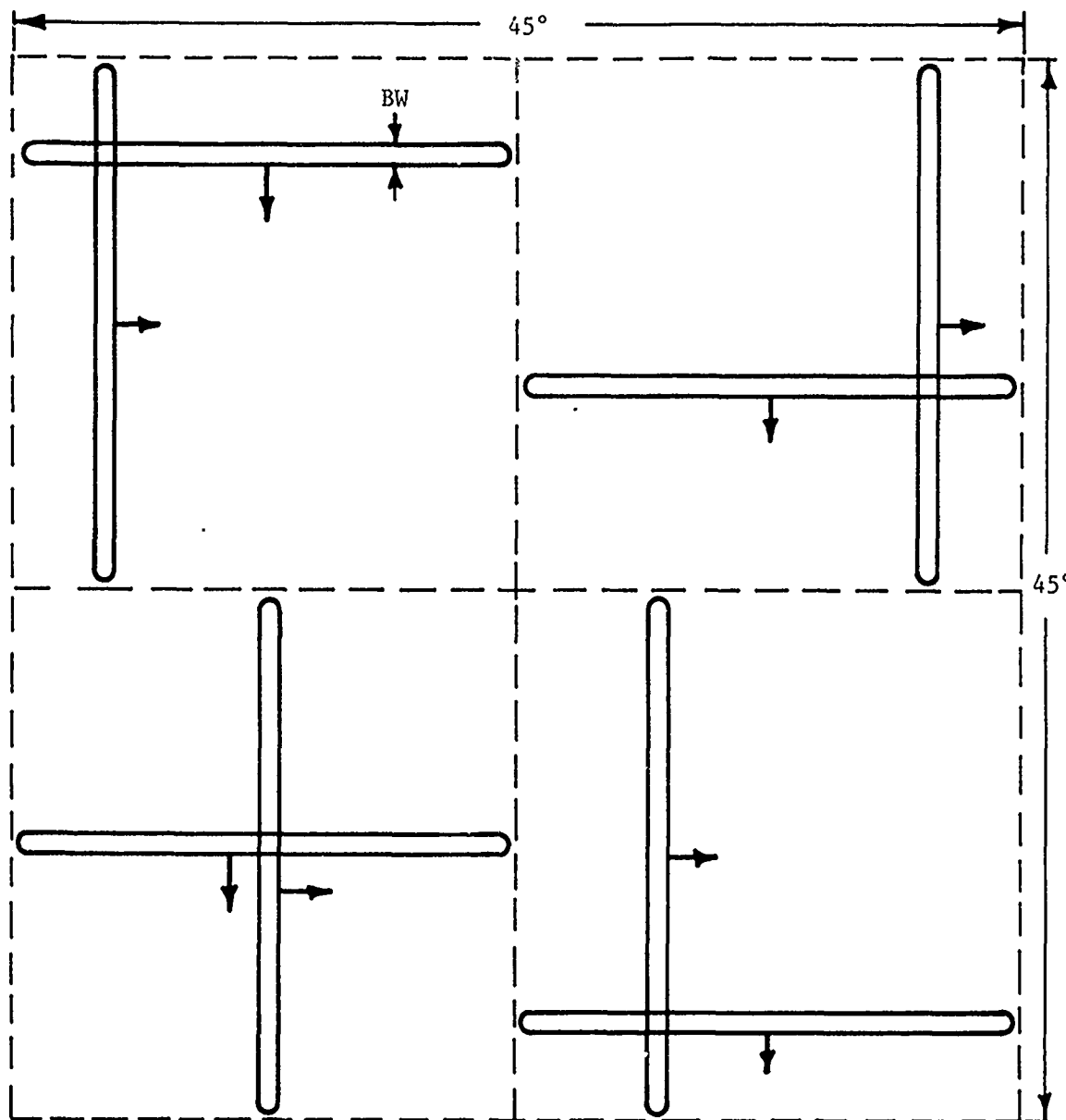


Figure 24. Four pairs of orthogonally scanning fan beams which collectively cover a 45° by 45° sector. Beams are energized sequentially (i.e., one beam moves from top to bottom, then other beam moves from left to right). The different pairs are independent and their sectors may overlap.

range of 5 nmi. is deemed sufficient, then a PRF of 15 kHz may be used. This corresponds to a time-between-pulses of 67 microseconds or a total beam-on-target (5 pulses) time of 333 μ sec. The number of beamwidths B in a sector W is given by

$$N = W/B \quad (70)$$

The total time to scan the sector is then

$$333 W/B \times 10^{-6} = 1/\text{scan rate} \quad (71)$$

or

$$B = 333(W) (\text{scan rate}) 10^{-6}. \quad (72)$$

The largest beamwidth requirement occurs when $W = 45^\circ$, and a scan rate of 10 per second is probably typical. These values yield a minimum beamwidth of

$$B = 0.15^\circ \quad (73)$$

Using Equation (68), a 42-inch aperture produces a $.39^\circ$ beam at 46 GHz which is well above the minimum value of Equation (73). This beamwidth produces gains of 32.3 dB and 35.3 dB for fan beams which cover windows of $45^\circ \times 45^\circ$ and $22.5^\circ \times 22.5^\circ$, respectively. These gain values are used in Equation (66) to calculate the S/N values listed in Table VII below.

TABLE VII

CALCULATED SIGNAL-TO-NOISE RATIO AT
46 GHz FOR ANTENNA GAINS OF 32.3 dB and 35.3 dB

Range (nmi)	Calculated S/N (dB)	
	32.3 dB Gain	35.3 dB Gain
1	31.6	37.6
2	18.8	24.8
3	11.0	17.0
4	5.3	11.3
5	0.7	6.7
6	-3.2	2.8
7	-6.6	-0.6

Table VII shows that marginal track may be established at a range between four and five nautical miles. This corresponds to intercept ranges of 1 and 2.5 nmi. for warm-up during and before, respectively, track is established.

C. Acquisition Volume

1. Acquisition Range

At this point, several bounds on the acquisition volume are known: (1) the azimuth sector desired by APL is 45° , (2) the target can be handed off to the tracker at a range of four nautical miles from the ship, and (3) all targets remain less than 20° in elevation outside the minimum range of four nmi. The remaining and most critical boundary is the maximum range at which the acquisition system must function so that a target may be relayed to the tracker at the four mile point. This maximum range is given by

$$R_m = R_t + V_t T_s \quad (74)$$

where,

- R_m = maximum acquisition range,
- R_t = track handoff range (4 nmi.),
- V_t = maximum threat radial velocity (2200 ft./sec.),
- T_s = time between first acquisition and track handoff.

T_s may be found from the relation

$$T_s = N_s N_p N_b / \text{PRF} \quad (75)$$

where,

- N_s = desired number of window scans each yielding a detection,
- N_p = number of pulses on target per beamwidth
- N_b = number of beam positions per window,
- PRF = pulse repetition frequency = $c/2R_m$,
- = $0.9c/2R_m$ for some margin,
- c = speed of light.

Substituting these parameters in Equation (74), yields the following relation

$$R_m = R_t + 2V_t N_s N_p N_b R_m / 0.9c \quad (76)$$

Rearranging terms yields a quadratic form for the above equation.

$$R_m = \frac{R_t}{1 - \frac{2V_t N_s N_p N_b}{0.9c}} \quad (77)$$

N_p has been set equal to 6 pulses per beam position as was done in APL's calculations. It is felt that the target should be at or above the detectable level for six (N_s) scans since an operator needs "several" before making a decision. Also, it should be remembered that the combination of multipath and radar cross section fluctuation could cause the signal to drop below the minimum detectable value thereby breaking the sequence of detections. N_b , the number of beam positions per window, is the only parameter as yet unspecified. N_b depends directly on the beamwidth and could be determined immediately if either required gain, scan sector time, or two-target resolution were specified; however, no hard requirements exist at this point. Equation (77) was solved as a function of beamwidth, and the results are shown in Figure 25 for some typical values of V_t and N_s . In this solution of Equation (77), N_b is related to the pencil beamwidth BW by

$$N_b = \frac{45^\circ \times 20^\circ}{(0.6 \text{ BW})^2} \quad (78)$$

Based on the curves of Figure 25, it is seen that the radar should be capable of detecting the threat at a range of ≈ 7 nautical miles.

2. Acquisition Signal-to-Noise Ratio

The received signal-to-noise ratio for the acquisition function can be found from Equation (62) which was used for the tracking case. The factors in this equation may be rearranged so as to solve for the gain required to yield a desired S/N as a function of range.

$$G(\text{dB}) = \frac{1}{2} \left\{ 10 \log_{10} \left[\frac{(4\pi)^3 R^4 \text{KTB}}{P_t \lambda^2 n E(n)} \right] + S_n + 2\alpha R \right. \\ \left. + 2\beta R + L_s + N_f \right\} \quad (79)$$

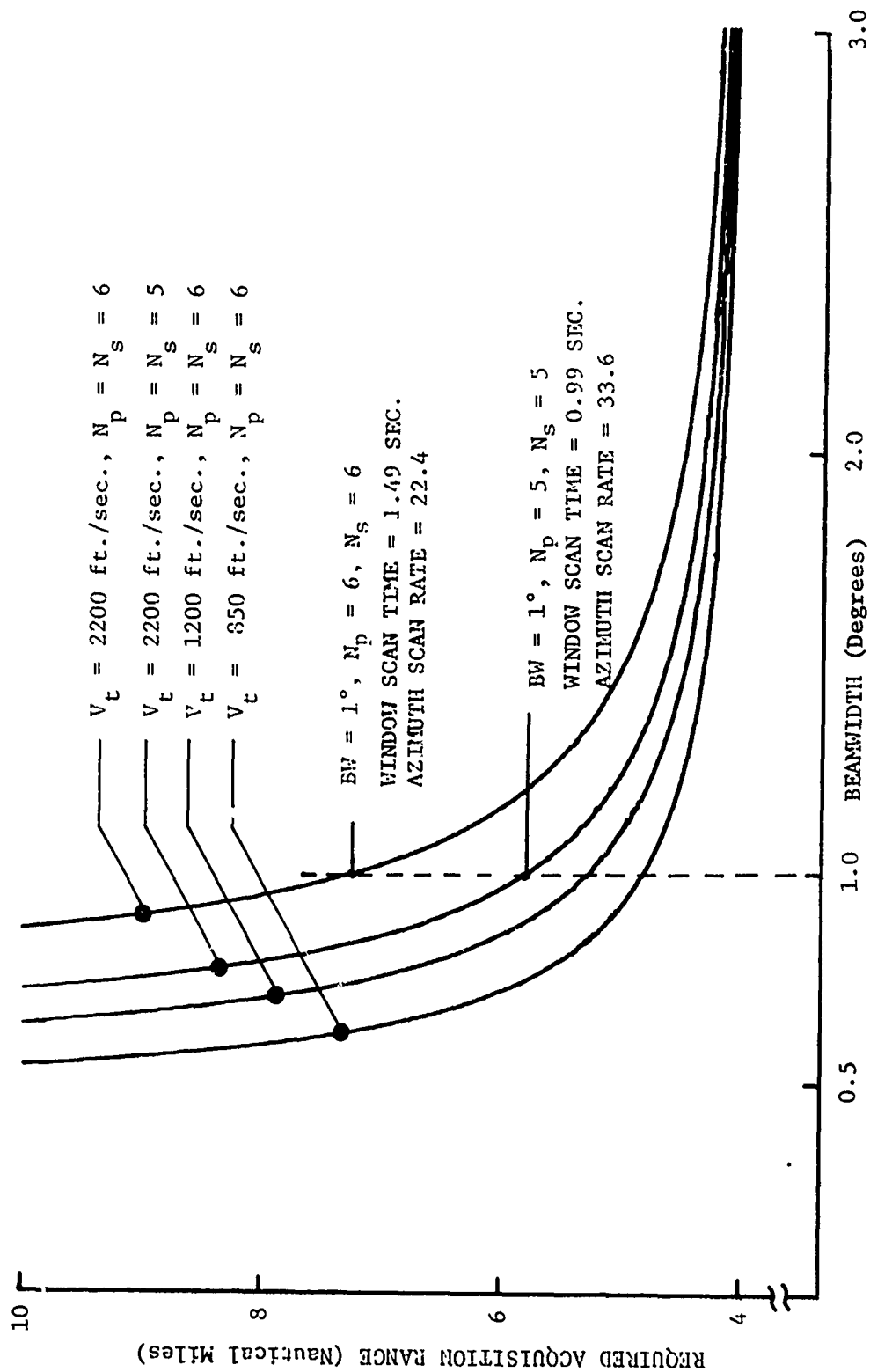


Figure 25. Calculated acquisition range required to obtain the indicated pulses per beamwidth (N_p) and scan observations (N_s) as a function of beamwidth for three different target velocities.

where S_n is the desired ratio and α and β are the one-way atmospheric and rainfall, respectively, attenuation factors and the other factors are as defined in Section IV.B. Equation (79) was evaluated as a function of range for the specific set of parameters in Table VIII and the following set of common parameters.

$$\begin{aligned}\sigma &= 0 \text{ dB} \\ n &= 6 \\ E(n) &= 0.8 \\ B &= 67.8 \text{ dB} \\ KT &= -204 \text{ dB} \\ S_n &= 12 \text{ dB} \\ L_s &= 9 \text{ dB} \\ N_f &= 10 \text{ dB}\end{aligned}$$

The gain required to produce a signal-to-noise ratio at a given range is plotted as a function of range in Figures 26 through 32 for a number of frequencies of interest. This gain was calculated for the cases of both a clear day and moderate rain. The model used for rainfall attenuation was that of Goldstein [7] which was discussed in Section III.C. As is apparent from these curves, the degradation due to rain (i.e., increased gain requirements) becomes increasingly more important at the smaller wavelengths. The gain and consequently the pencil beamwidth and aperture dimensions (Eqs. (67) and (68), respectively) were determined at a range of 8 nmi. from these plots and are listed below.

Frequency (GHz)	Clear Day			4 mm/hr. Rain		
	Gain (dBi)	BW (°)	Aperture Dim. (In.)	Gain (dBi)	BW (°)	Aperture Dim. (In.)
9.3	32.3	4.20	19.7	33.2	3.79	21.8
16.5	37.0	2.45	19.0	41.0	1.54	30.2
23	41.3	1.49	12.4	50.0	.55	60.7
35	41.3	1.49	14.7	59.8	.18	121.9
46	42.3	1.33	12.5	69.4	.06	278.2
70	54.2	.34	32.3			
95	51.9	.44	18.4			

TABLE VIII.

SYSTEM PARAMETERS USED IN CALCULATION
OF ANTENNA GAIN REQUIREMENTS

<u>Frequency (GHz)</u>	<u>Wavelength (Inches)</u>	<u>Peak Pulse Power (kW)</u>	<u>One-Way Atmospheric Attenuation (dB/km)</u>	<u>One-Way Rainfall Attenuation (dB/km)</u>
9.3	1.27	250	0.0092	0.068
16.5	0.72	100	0.0273	0.261
23	0.51	65	0.155	0.590
35	0.34	75	0.0487	1.24
46	0.26	125	0.113	1.83
70	0.169	10	0.415	2.64
95	0.124	8	0.138	3.11

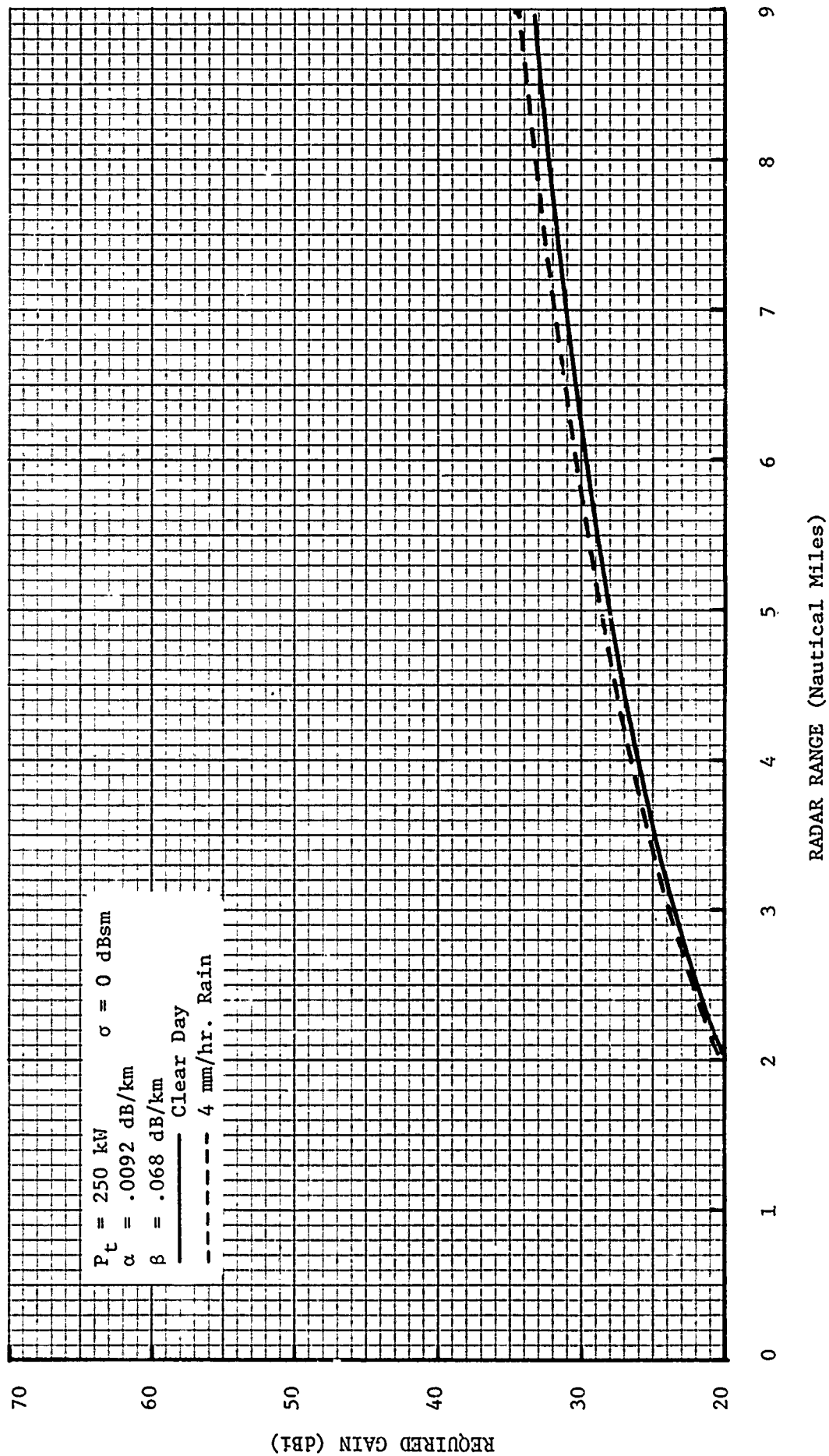


Figure 26. Required gain as a function of range to produce a 12 -dB signal-to-noise ratio from a radar operating at 9.3 GHz for the cases of a clear day and 4 mm/hr of rain.

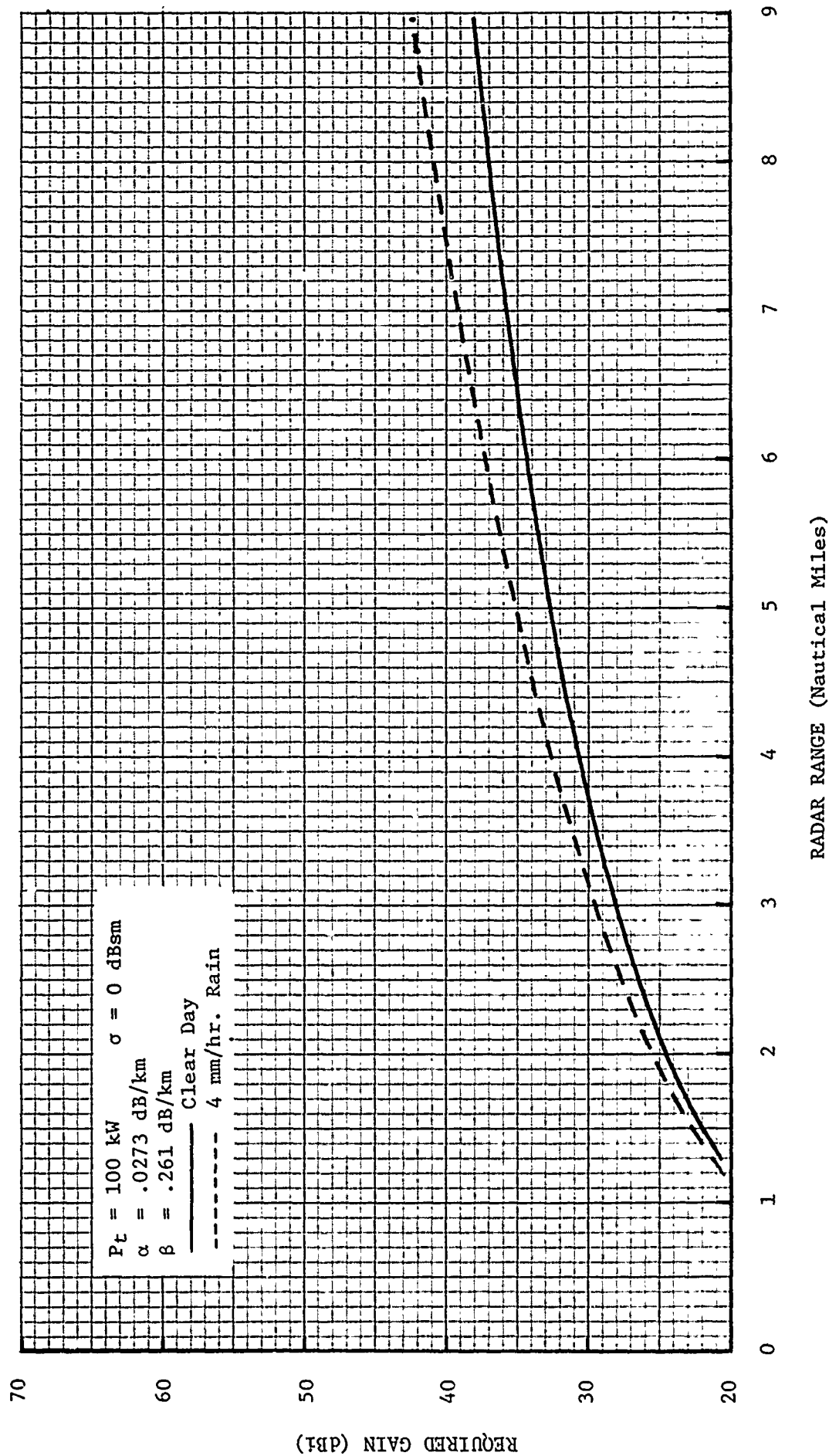


Figure 27. Required gain as a function of range to produce a 12 -dB signal-to-noise ratio from a radar operating at 16.5 GHz for the cases of a clear day and 4 mm/hr of rain.

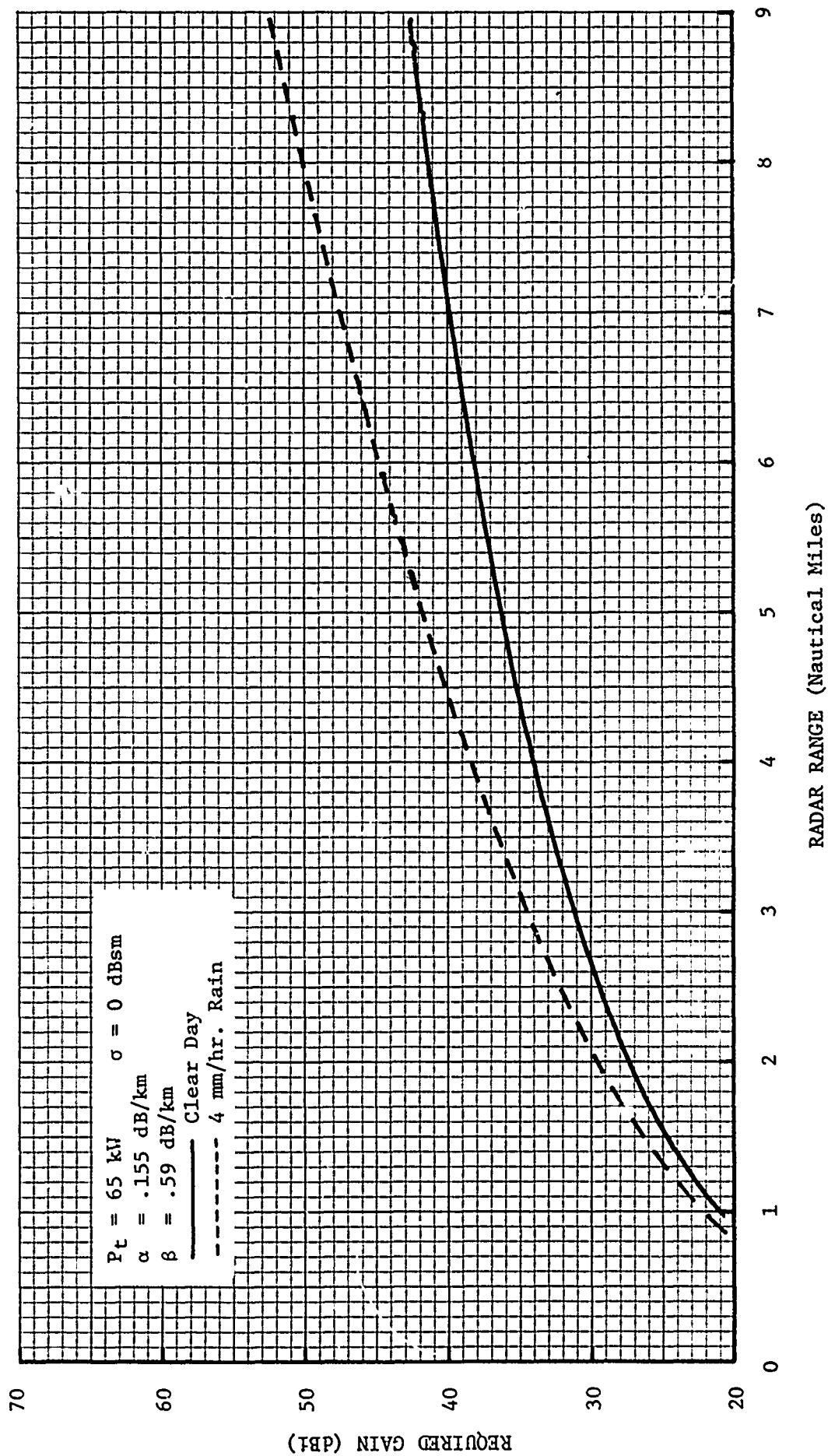


Figure 28. Required gain as a function of range to produce a 12 -dB signal-to-noise ratio from a radar operating at 23 GHz for the cases of a clear day and 4 mm/hr of rain.

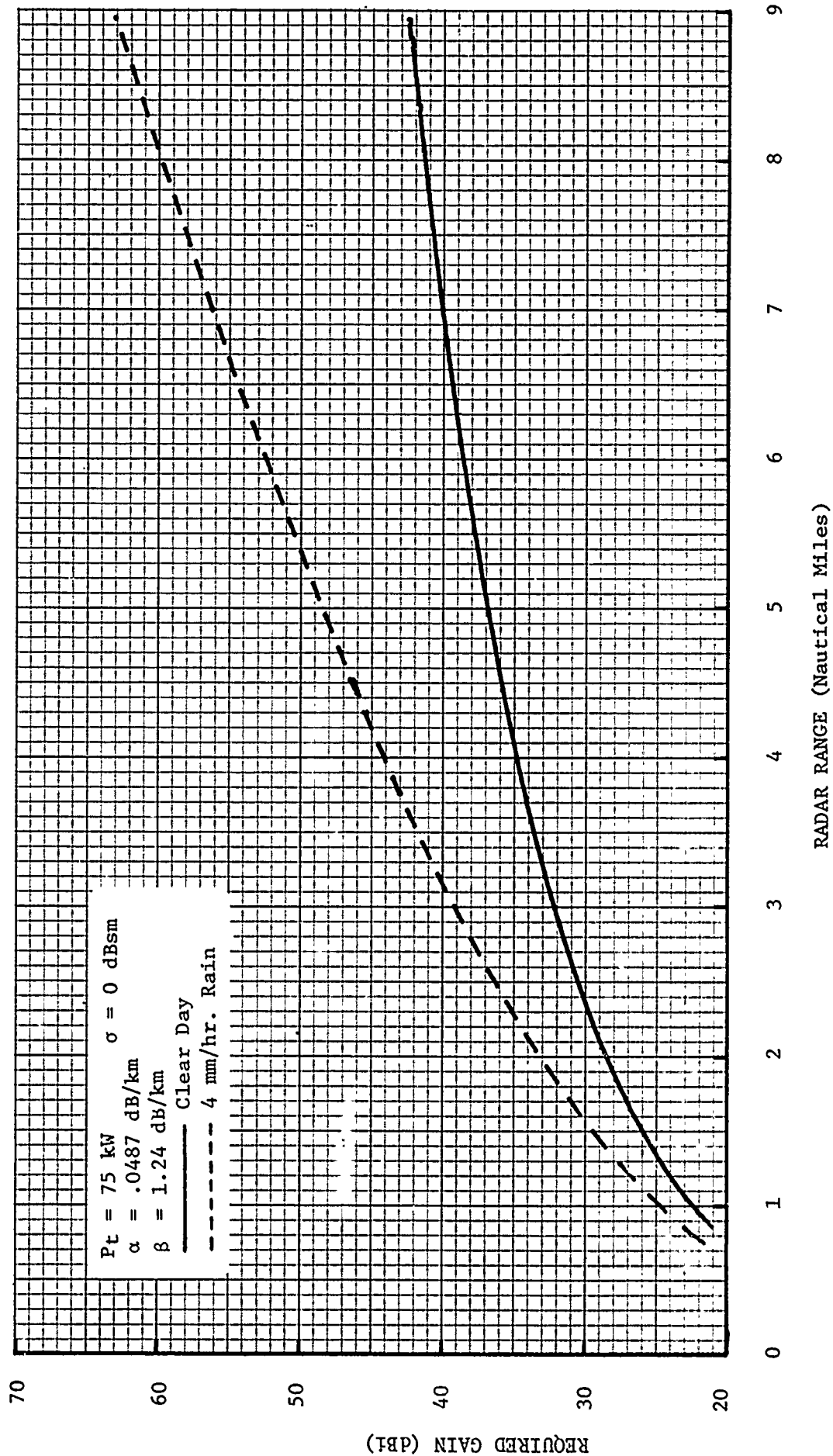


Figure 29. Required gain as a function of range to produce a 12 -dB signal-to-noise ratio from a radar operating at 35 GHz for the cases of a clear day and 4 mm/hr of rain.

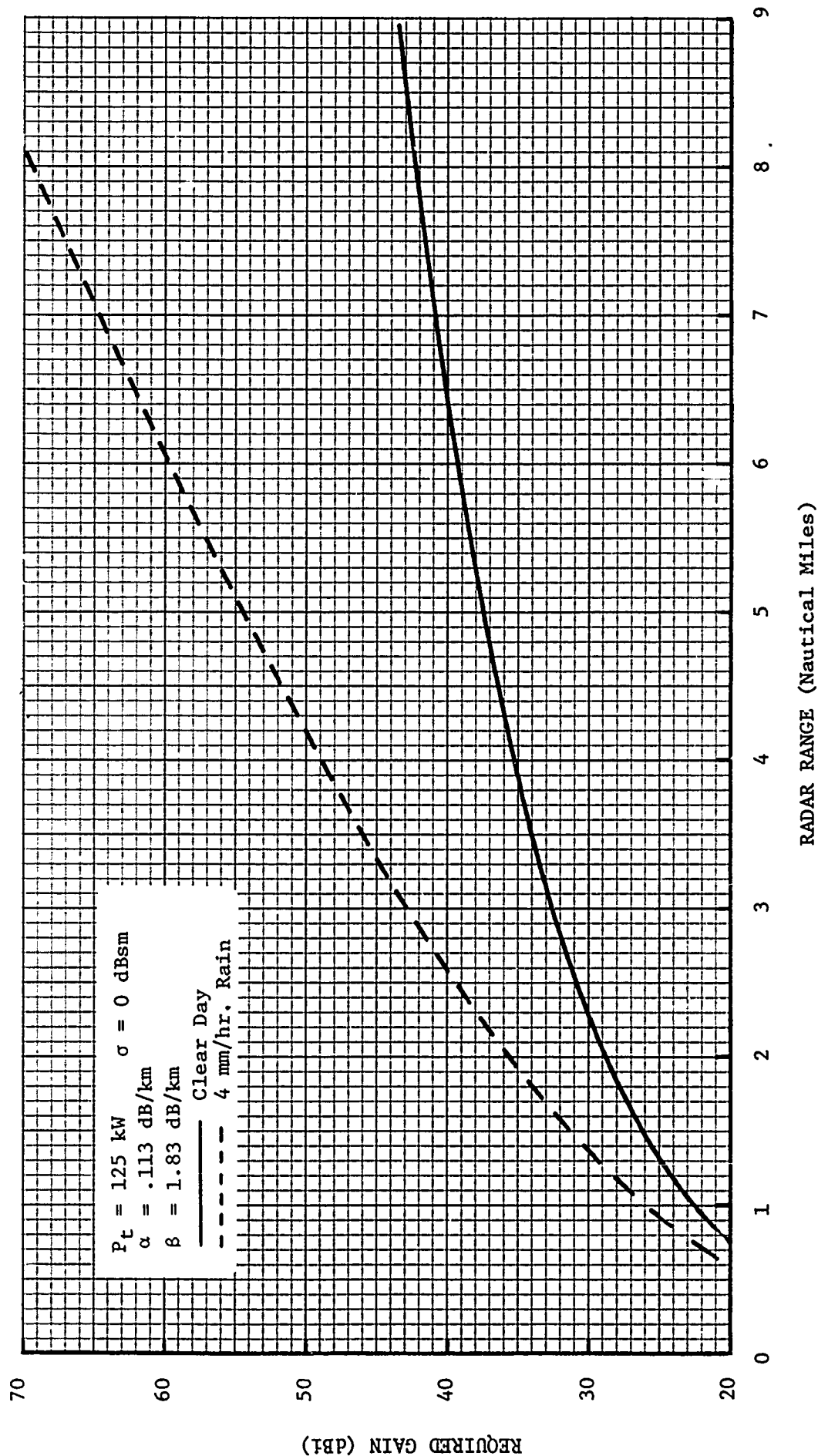


Figure 30. Required gain as a function of range to produce a 12 -dB signal-to-noise ratio from a radar operating at 46 GHz for the cases of a clear day and 4 mm/hr of rain.

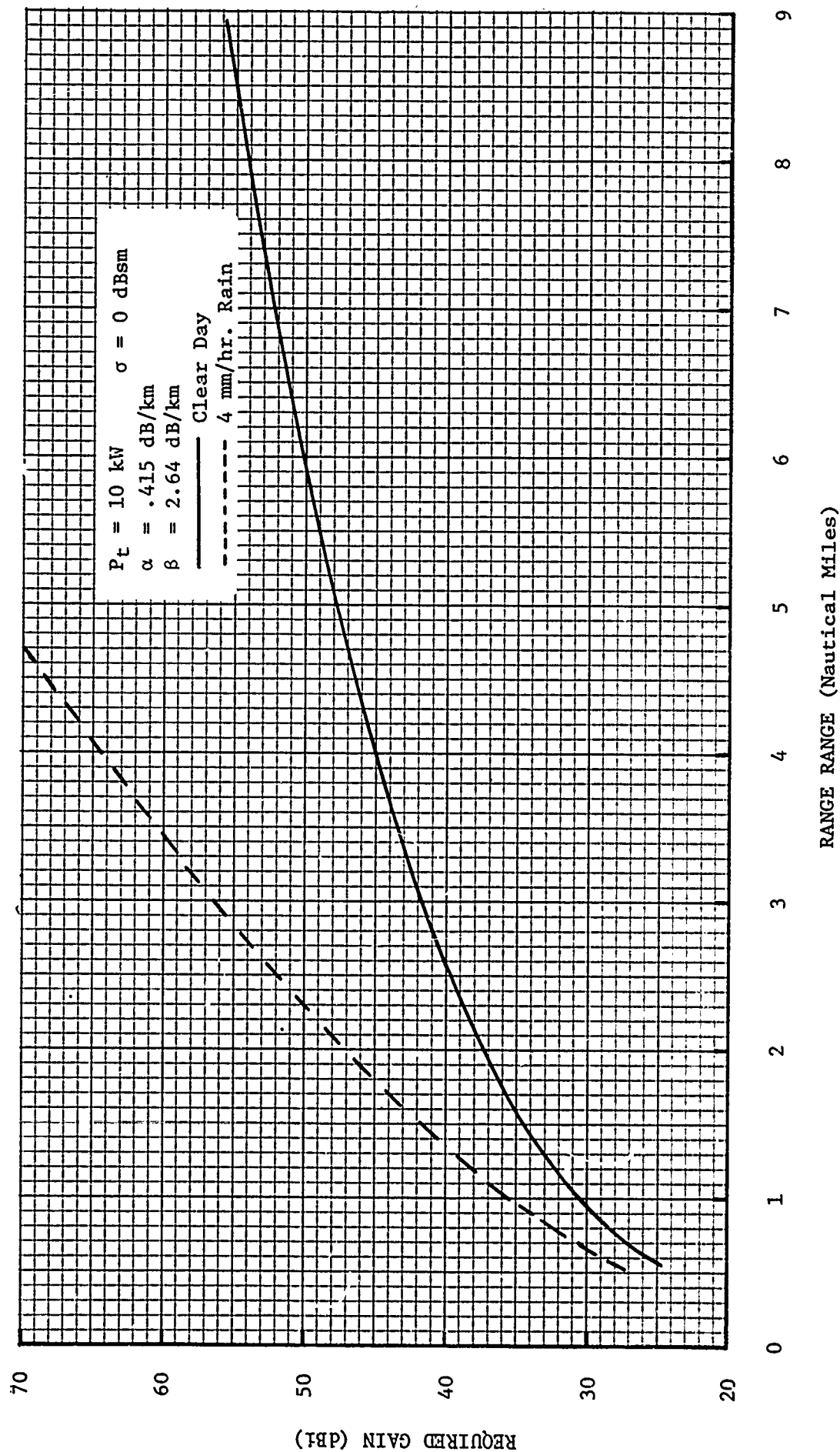


Figure 31. Required gain as a function of range to produce a 12 -dB signal-to-noise ratio from a radar operating at 70 GHz for the cases of a clear day and 4 mm/hr of rain.

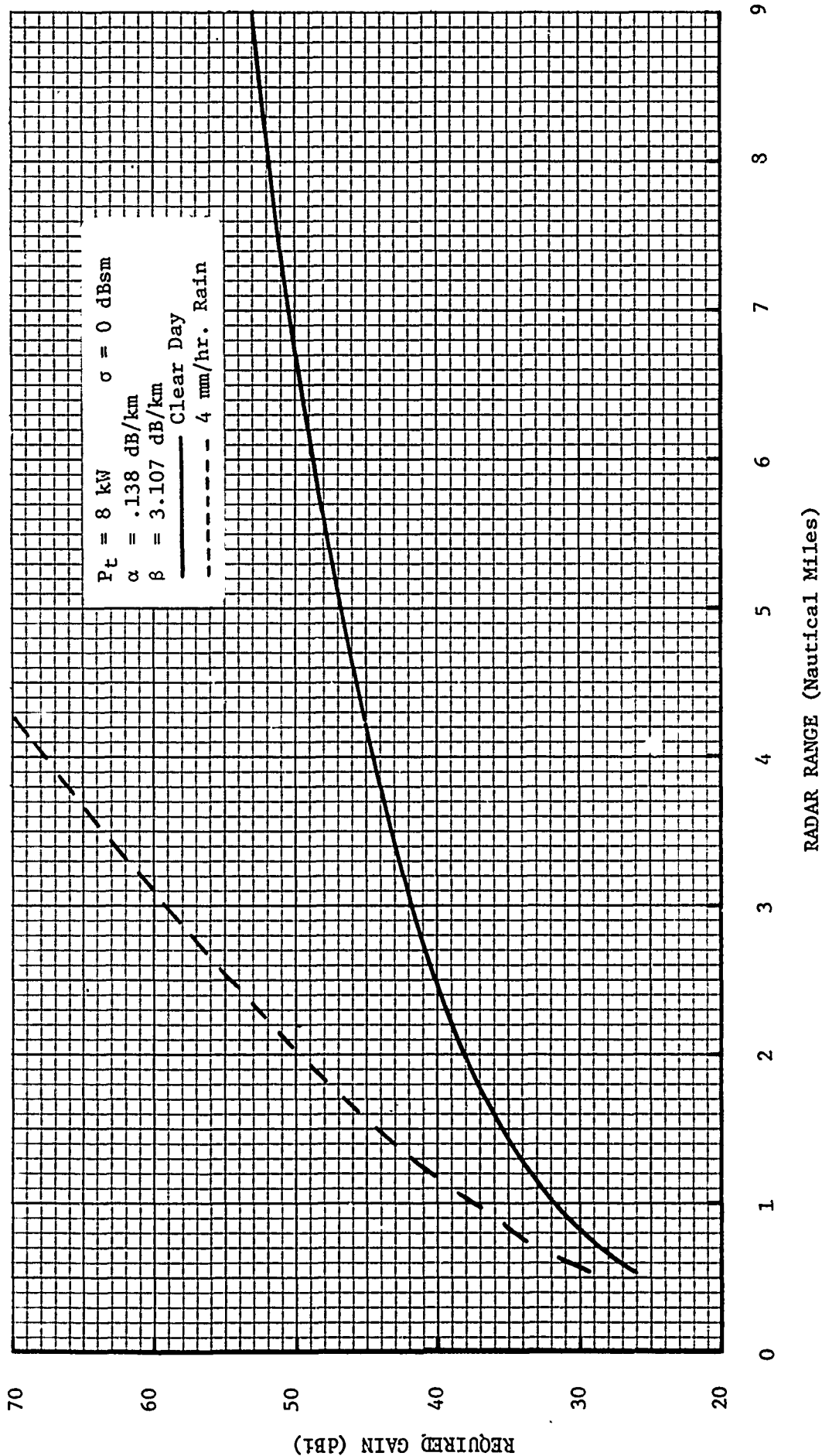


Figure 32. Required gain as a function of range to produce a 12 -dB signal-to-noise ratio from a radar operating at 95 GHz for the cases of a clear day and 4 mm/hr of rain.

V. CANDIDATE ANTENNA CONCEPTS

In this section, several of the basic scanning techniques (e.g., frequency, phase, electromechanical, etc.) are discussed and specific design examples of each are presented.

A. Frequency Scanning

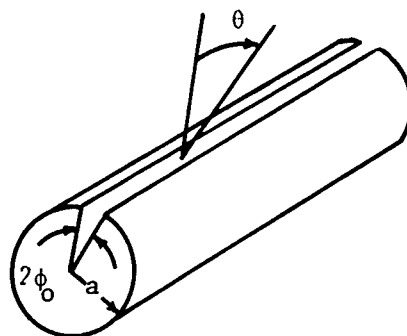
Line-source collimation may be accomplished by interrupting the normal field configuration of a transmission line that is carrying electromagnetic energy. These fields can be interrupted and coupled away from the line in such a manner so that they form a wavefront which is traveling in a desired direction. By appropriate design, the direction of the radiated wavefront may be varied by changing the frequency of the transmitted wave as this corresponds to changing the relative phase between two fixed points. Since transmission lines can usually be made quite small, they can serve as extremely small line sources, and may be arrayed to form very thin planar sources. Typical examples of such line sources are shown in Figure 33. Such frequency scanning line sources may be grouped to achieve single plane scanning of a pencil beam. If the phase of the input energy to each line source is controlled as shown in Figure 34, then the pencil beam may be made to scan independently in two orthogonal planes.

Before discussing the complete frequency scanning antenna, it is desirable to investigate the scanning properties of certain line sources. The line sources considered in this report are of two general forms: (1) continuous slot radiators (Figure 33(a) and (b)), and (2) discrete slot radiators (Figure 33(c) and (d)). It will be shown in the following paragraphs that the continuous slot is not feasible for wide angle scan sectors and that the discrete slot radiator must be meandered (or serpentine) to be applicable.

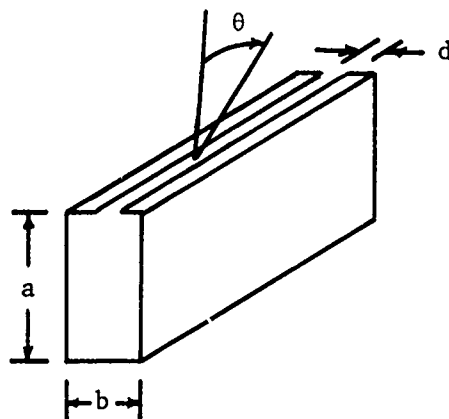
1. Continuous Slotted Circular Waveguide

A circular waveguide (Figure 33(a)) with a continuous slot behaves as a leaky wave antenna. As with all continuous slot radiators, its scan angle is given by:

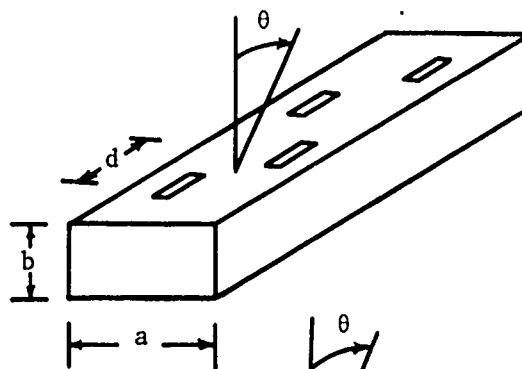
$$\sin \theta \approx \frac{\lambda}{\lambda_g} \quad (80)$$



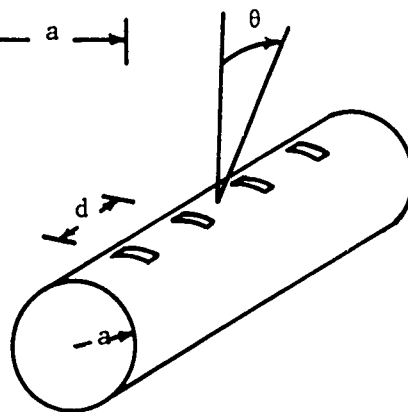
(a) Circular waveguide with continuous slot.



(b) Rectangular waveguide with continuous slot.



(c) Rectangular waveguide with discrete slots.



(d) Circular waveguide with discrete slots.

Figure 33. Conceptual diagram of four frequency scannable slot-type radiators.

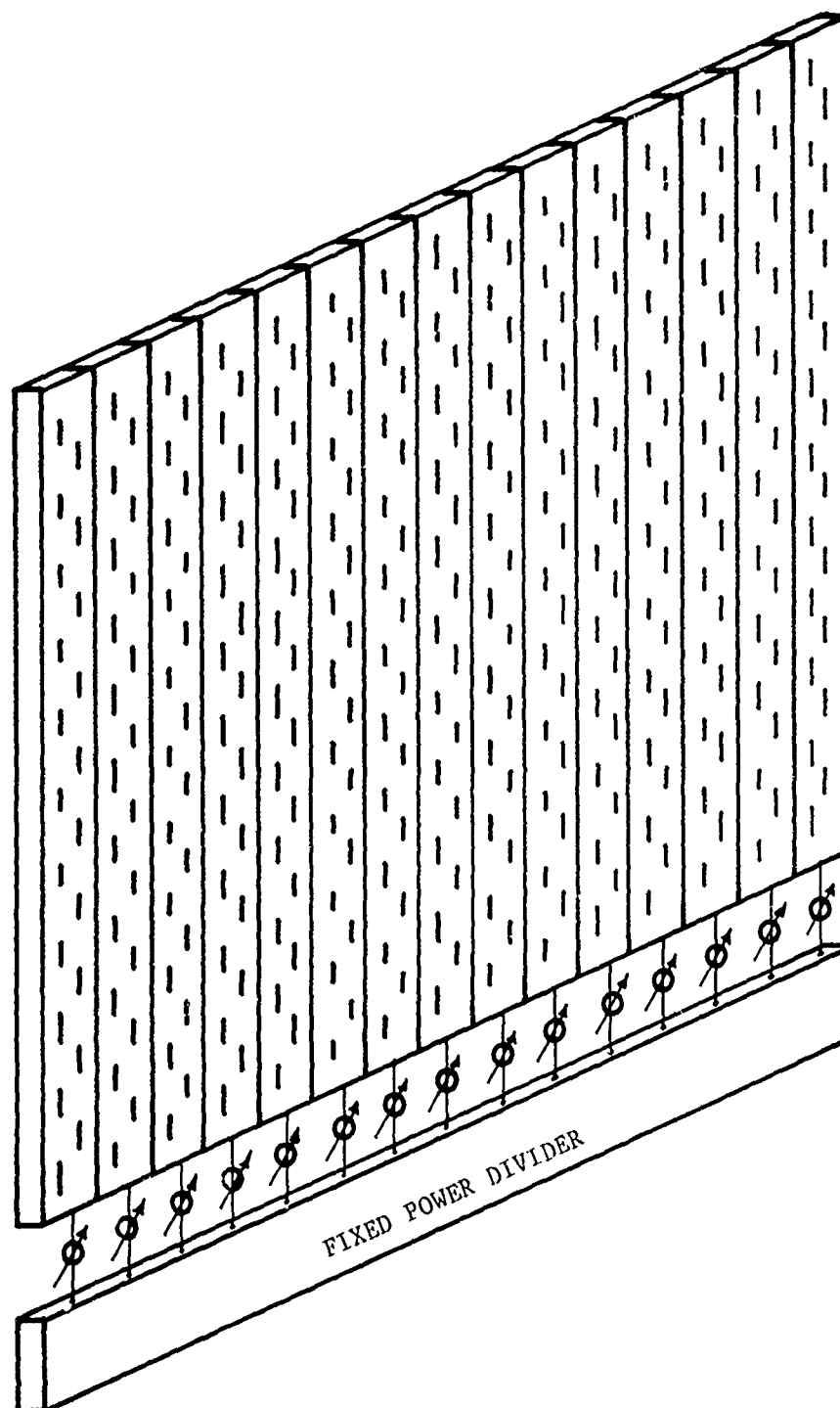


Figure 34. Planar array composed of vertical stack of slotted waveguides. Frequency shifting produces elevation scanning while phase scanning (i.e. phase shifters) controls the beam in azimuth.

where θ is the angle from broadside as shown in Figure 33. The guide wavelength is affected by the slot size and can be found from the following equations [14]:

$$\lambda_g = \frac{2\pi}{k_z} \quad (81)$$

where

$$k_z = \sqrt{k_o^2 - k_p^2} \quad (82)$$

The angle subtended by the slot is $2\phi_o$.

For ϕ_o small:

$$k_p a = k_{po} a + \delta \quad (83)$$

where k_{po} is the value for the unperturbed waveguide and a is the radius of the circular waveguide.

The parameter δ is found by solving the following equation:

$$A\delta^2 + B\delta + C = 0, \quad (84)$$

where

$$A = \left[\frac{H_1''}{H_1'} + \frac{J_1'''}{2J_1''} \right] B - J_1'' H_1' \sum_{\substack{n=0 \\ n \neq 1}}^{\infty} \epsilon_n \frac{J_n'' H_n' + J_n' H_n''}{(J_n' H_n')^2} \left[\frac{\sin n\phi_o}{n} \right]^2, \quad (85)$$

$$B = J_1'' H_1' \sum_{n=0}^{\infty} \frac{\epsilon_n}{J_n' H_n'} \left[\frac{\sin n\phi_o}{n} \right]^2, \quad (86)$$

$$C = \sin^2 \phi_o, \quad (87)$$

$$\epsilon_n = \begin{cases} 1 & \text{for } n = 0 \\ 2 & \text{for } n \neq 0 \end{cases} \quad (88)$$

J_n and H_n are the n^{th} - order Bessel and Hankel (first kind) functions, respectively. In these functions, an argument $k_p a = 1.841$ is implied. The primes denote derivatives with respect to the argument.

The results of the equations given above were computed and plotted by Harrington [15] and are repeated in Figure 35 for WC 38 circular waveguide propagating the dominant TE_{11} mode. The cutoff frequency in this case is 18.46 GHz. Equation (80) was evaluated for values of ϕ_0 equal to 0° , 2.4° , and 15° and the results are shown in Figure 35.

2. Continuous Slotted Rectangular Waveguide

A continuous slot in the narrow wall of a rectangular waveguide behaves as a leaky wave antenna where the scan angle is again given by [14]

$$\sin \theta = \frac{\lambda}{\lambda_g} \quad (89)$$

The guide wavelength can be determined from the following equations:

$$\lambda_g = \frac{2\pi}{\beta_z} \quad (90)$$

and

$$\beta_z = \beta_{z0} - \frac{\pi}{\beta_{z0} a^2} \frac{B}{G^2 + B^2} \quad (91)$$

where β_{z0} is the value for the unperturbed waveguide, $G = \pi b/2a$, and

$$B = \frac{b}{a} \ln \left(\frac{e}{\gamma} \frac{a}{d} \csc \frac{d}{2b} \right) \quad (92)$$

where d is the slot thickness, a and b are the wide and narrow dimensions of the waveguide, $e = 2.713$, and $\gamma = 1.781$.

The scan angle versus frequency is plotted in Figure 36(a) and (b) for various values of slot thickness, for WR 42 and WR 28 waveguide, respectively. The zero-thickness continuous slot scanning characteristics for WR 28, WR 42, and WC 38 are shown for comparison in Figure 37.

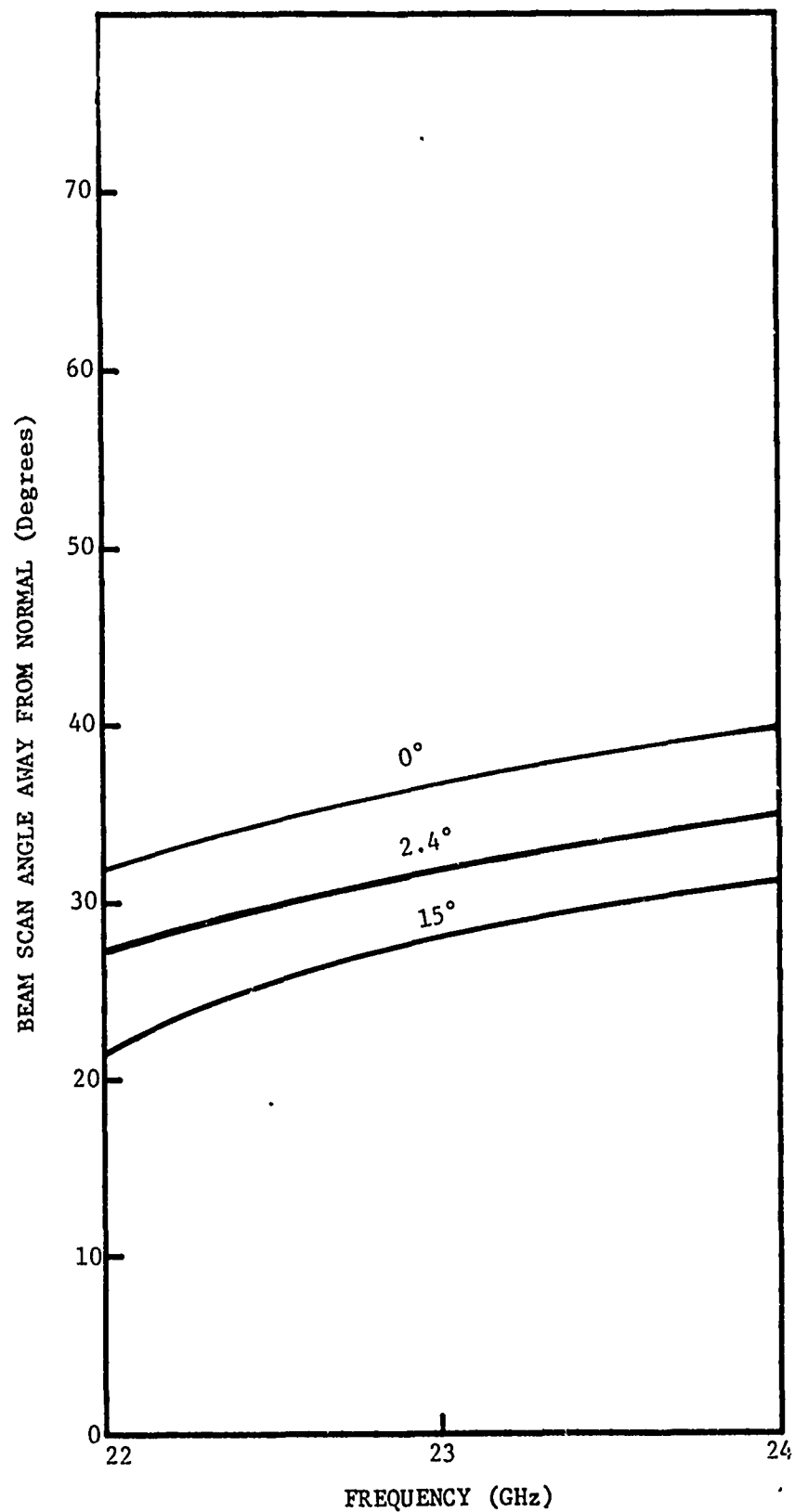


Figure 35. Calculated beam pointing angle as a function of frequency for a circular waveguide (WC 38) with the continuous axial slots shown.

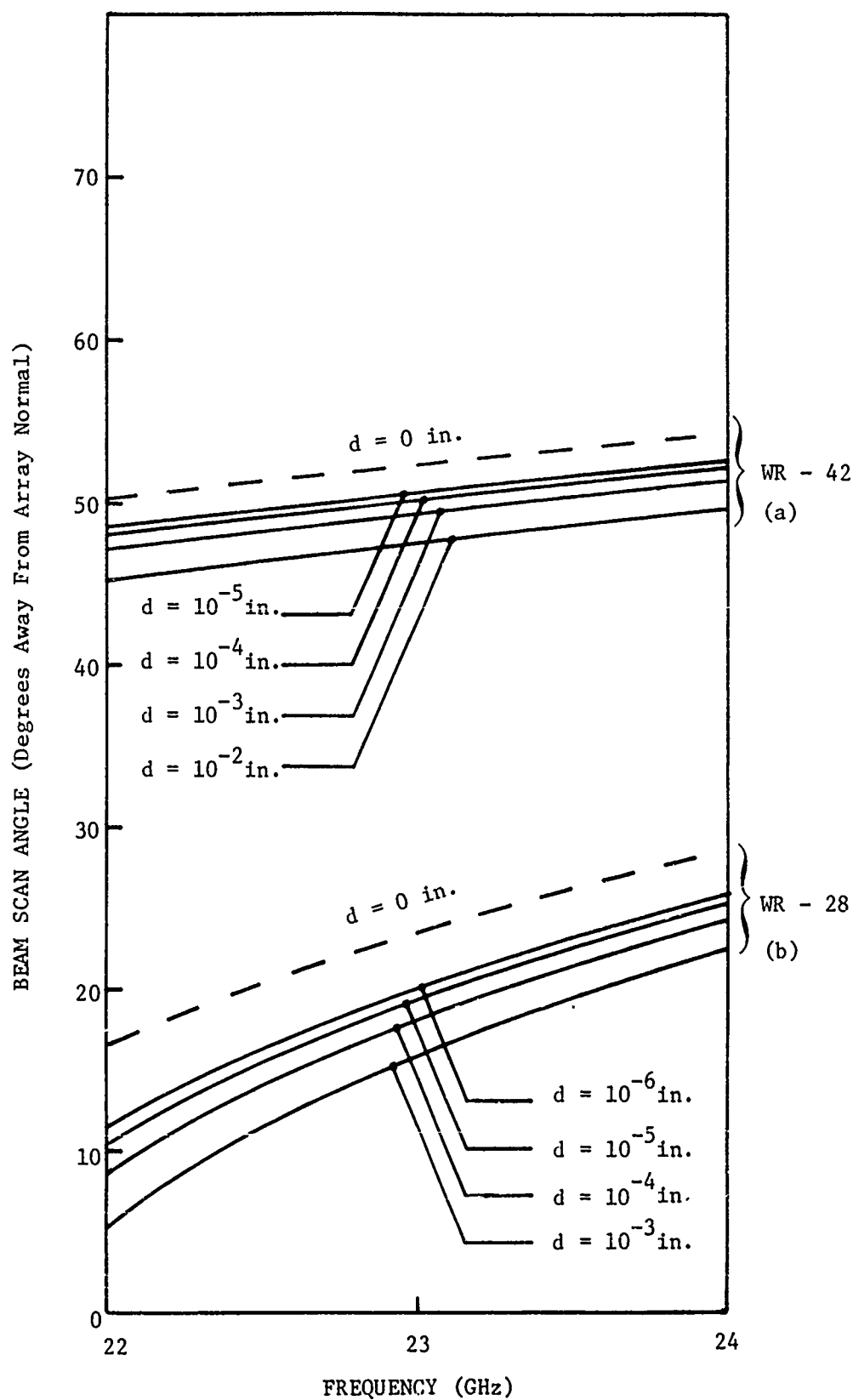


Figure 36. Calculated beam pointing angles for radiation from rectangular WR-28 and WR-42 waveguide with continuous slot in narrow wall.

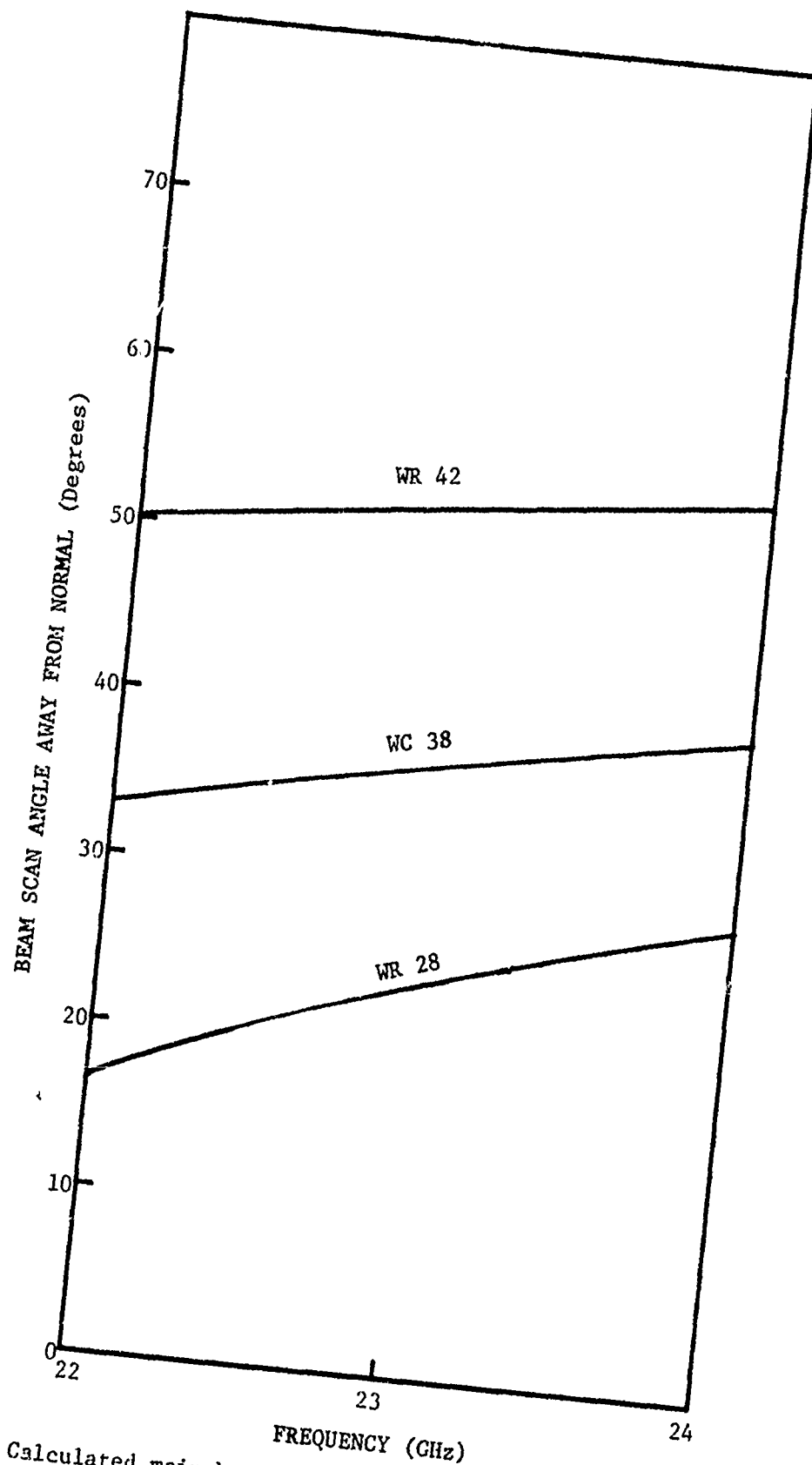


Figure 37. Calculated main beam pointing directions for the three different continuously slotted waveguides (zero slot width) shown.

3. Discrete Slots In Rectangular Waveguide

Due to restrictions on maximum sidelobe levels, polarization, or beam scan angle, often, the continuous radiators discussed in the previous paragraphs are not applicable. The percentage of input energy per unit length which is coupled out of the previously described antennas does not vary with distance along the transmission line; consequently, the aperture illumination has the shape of a decaying exponential which is not commensurate with low sidelobes. In general, it is desirable to have a tapered distribution, that is, one which is very low at each end of the aperture and relatively high in the center. To achieve such an aperture distribution along a transmission line requires that the relative coupling vary from very low at each end to relatively high in the center of the line source. Also, one has much more control over the size and location of the scan sector in the discrete slot case.

The scan angle of an array of half-wave (slot length) slots in the broad wall (alternate positions about center of guide) of a rectangular waveguide is given by

$$\sin \theta = \frac{\lambda}{\lambda_g} - \frac{\lambda}{2d}, \quad (93)$$

where d is the spacing between slot centers. It was found from Equation (93) that the magnitude of the scan sector which could be obtained from reasonable frequency excursions (± 1 GHz in the 23 GHz band, for example) was too small for the present application. This scan sector can be increased by increasing the electrical distance between slots while maintaining the physical distance between the radiators. This can be accomplished by dielectrically loading the guide or by meandering the guide between slots so as to increase the electrical separation. When meandering is allowed, the equation for the scan angle becomes [16]

$$\sin \theta = \frac{L}{d} \left[\frac{\lambda}{\lambda_g} - \frac{\lambda}{2d} \right]. \quad (94)$$

Equation (94) above was plotted for a number of typical meander lengths in Figure 38. Apparently, scan sectors of either 20° or 45° are obtainable with modest frequency excursions.

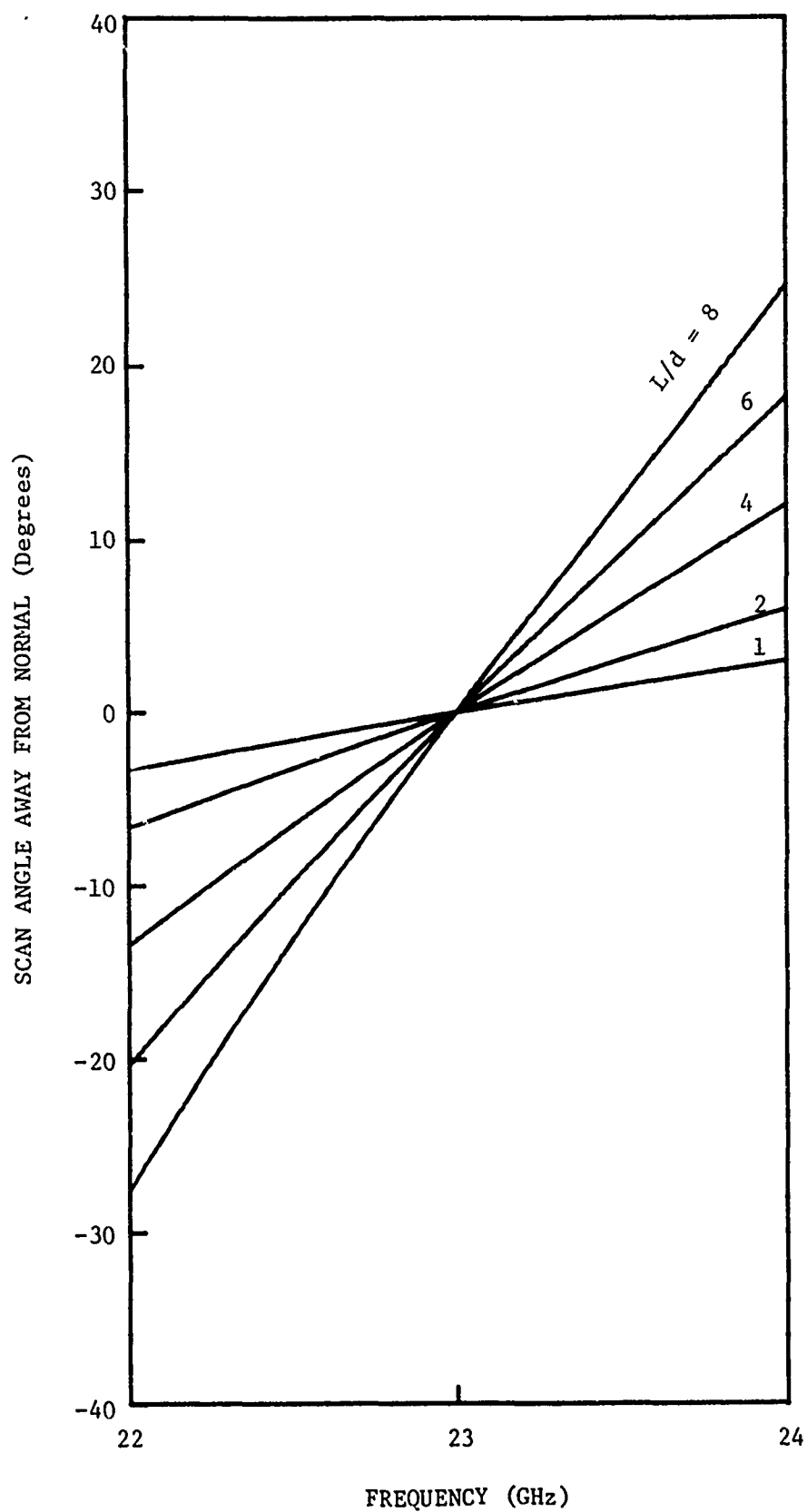


Figure 38. Calculated mainbeam pointing angle as a function of frequency for an array of resonant (23 GHz) slots in the broadwall of a serpentine waveguide.

4. Frequency Scanning System Considerations

A more basic point which should be addressed once it is known that the required sectors can be scanned is the type of system needed to accompany the scanning antenna. Basically, two different system types are available for producing frequency dependent scan: (1) continuous movement of the beam by continuously slewing of the transmitter frequency, and (2) the transmission of a number of discrete frequencies with each corresponding to a given scan angle.

A frequency scanning radar system using Doppler or MTI requires an accurate frequency source and the ability to switch frequencies quickly. One method that could possibly be used to accomplish this is shown in block diagram form in Figure 39. A multiplier converts the oscillator frequency to several different RF frequencies, one corresponding to each desired scan angle. A selector is used to select the specific RF frequency to be transmitted. The oscillator should be crystal controlled and temperature compensated. The selector might be a set of PIN diodes or ferrite switches depending on the frequency. A processor computes the scan angle and controls the selector. The RF output from the selector is amplified by an amplifier chain. The final stage of the amplifier chain would be a high power TWT. The output of the TWT is transmitted to the antenna via a T/R switch. A portion of the RF is coupled from the output of the selector and is mixed with the received signal. In the figure shown there is no IF stage. The RF amplifier would normally be a TWT in this case.

A frequency scanning radar using a magnetron would require a mechanical tuner to adjust the frequency for scanning. According to Skolnik "high-power magnetrons can be mechanically turned over a 5 to 10 percent frequency range routinely, and in some cases as much as 25 percent. Hydraulic tuners allow tuning across the band at rates up to 20 Hz, whereas the best gear tuners allow perhaps 2 Hz. Voice-coil tuners permit 200 Hz tuning rates over a small fraction of the band and roughly 60 Hz over the whole band." The output of the magnetron would be transmitted to the antenna via a T/R switch. The received signal would be amplified in an RF amplifier, which would be a TWT. The RF signal would then be mixed with the local oscillator signal and the output of the mixer

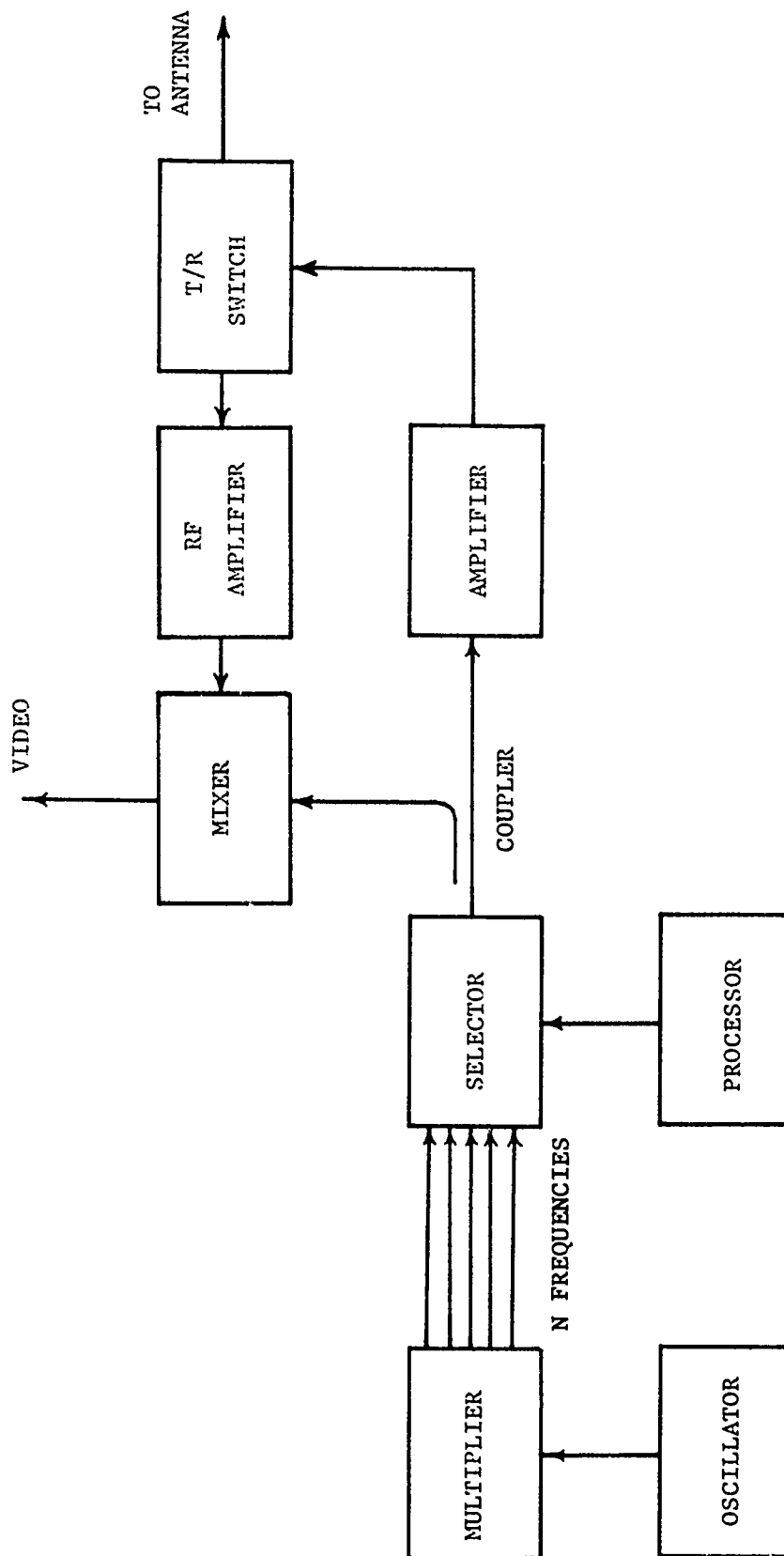


Figure 39. Block diagram of radar system which transmits a number of discrete frequencies with each corresponding to a unique beam pointing angle.

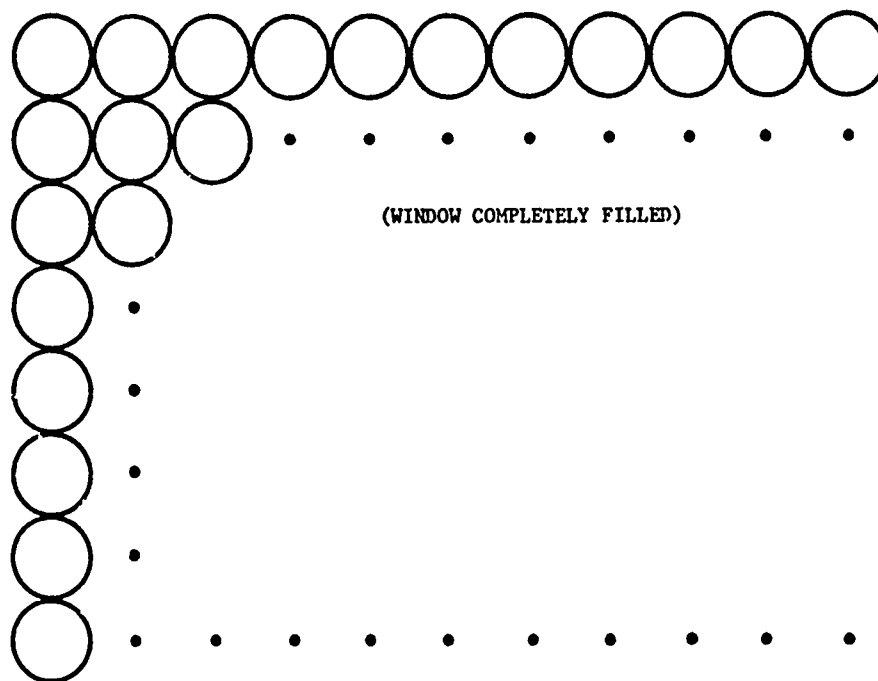
would provide the video signal. The need for a local oscillator which can track the frequency excursions of the magnetron is the greatest obstacle to the development of such a system. This system would probably not be suitable for Doppler measurement because of the mechanical tuning of the magnetron. It is also envisioned that a very complex electro-mechanical feedback system would be required to insure frequency excursion repeatability and correlation between actual and expected scan angle.

B. Electronic Phased Arrays

Electronic phased array is the term which describes a class of antennas having discrete radiators, a power division network, and a collection of electronically actuated phase shifters so that the relative phase of the energy leaving the radiators may be controlled. In general, the phase shifters are adjusted to produce a plane wave traveling in a desired direction; however, phase shifters can also be used for intentional beam spoiling (broadening) or in array feeds for reflectors whereby the apparent phase center location can be varied (for beam scanning) through the phase shifter settings. Two types of single beam phased arrays will be considered here: (1) a planar array capable of scanning a pencil beam in two dimensions, and (2) a scannable line source which achieves the second plane of collimation and scan through another means.

A method for effectively searching a sector of space is through a raster scanning electronic phased array. The beam sequentially moves through the set of discrete beam positions shown in Figure 40. This type of antenna has found wide application for search and tracking radars in the frequency bands up through K_u -band [17,18,19]. However, a few phased array radars have been developed at 23 GHz. Even so components which would be required for such an antenna system at 23 GHz are available from a number of manufacturers. A lesser number are available up to 50 GHz and very few array components exist at 70 and 95 GHz. Hence, array configurations for this system may be considered at 23 GHz.

The system function is to cover a 45° by 20° sector in azimuth and elevation, respectively. Conventionally, a planar phased array using two dimensional phase control has been used for this purpose.



(a) Sequential Illumination of Contiguous Beams

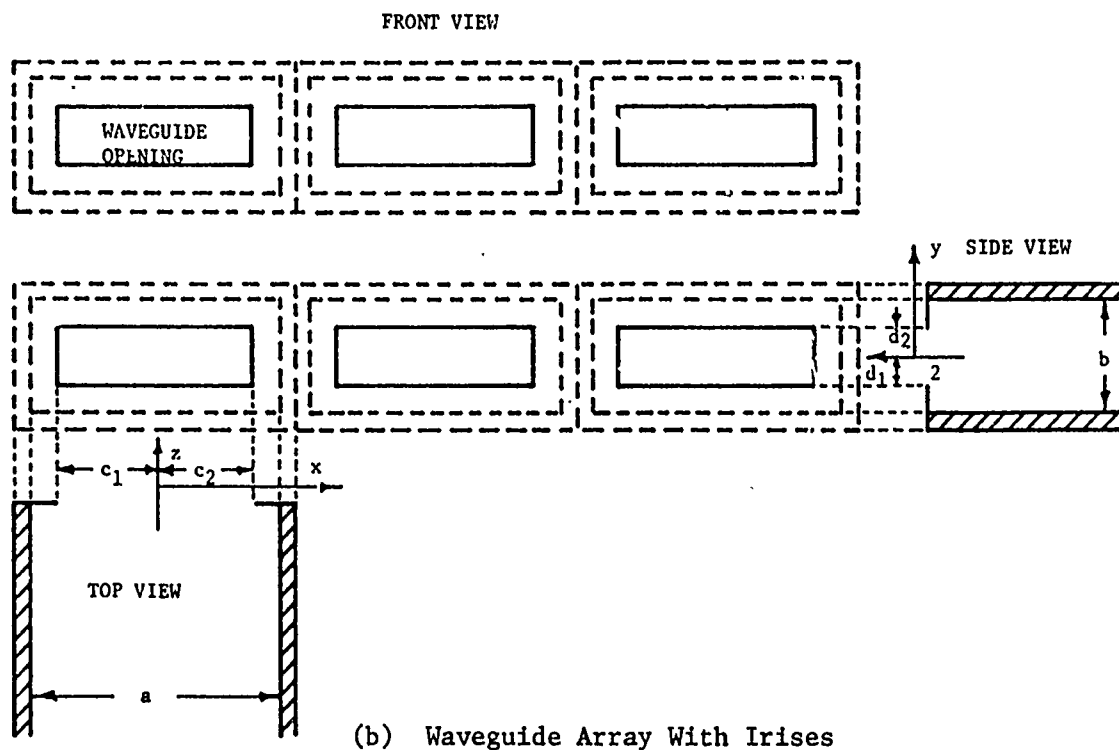


Figure 40. (a) Array of discrete beam positions and (b) array of open-end waveguides containing irises.

The feed system for this kind of an antenna may be either a corporate feed or space feed. Space fed systems are the easiest with which to work, but some loss in the way of reflections is associated with this type. Corporate feeding systems reduce the number of losses due to reflection, but the many feet of waveguide and power dividing junctions may reduce the radiated power. A comparison of these two systems will be made in the following paragraphs.

An orthogonal beam steering system will be considered, and therefore, the planar array matrix will be configured in a rectangular lattice. The array elements will be open-end waveguide. The size of the array will be determined by the beamwidth desired and the array illumination shape. An expression which relates the half power beamwidth to the aperture size, D , for a cosine illumination is given [20] by

$$BW = \frac{68.8\lambda}{D} \quad (95)$$

In the present application, a beamwidth on the order of 1° is desired; consequently,

$$D = 68.8\lambda \quad (96)$$

At 23 GHz the free space wavelength is 0.513 inches which gives a total aperture size of 35.33 inches ($D/d = 70$). This will determine the number of elements required to fill the aperture once the individual radiating elements have been selected.

Whenever an array of waveguide elements is arranged in a rectangular lattice, radiation nulls will exist at certain scan angles off broadside. The reason for this phenomenon is that the reflection coefficient, which is dependent on mutual coupling between waveguide elements, varies with scan angle. When the critical scan angle is approached, the reflection coefficient approaches 1.0. This problem may be alleviated to some extent by altering the waveguide elements in such a way so as to wide-angle impedance match the array system. Several matching schemes have been devised in the past such as dielectric loading [21], corrugated plates [22], and dummy shorted waveguides [23]. These have been successful to some extent but have been proven to be extremely frequency sensitive. An alternative approach utilizing inductive irises at the open end of

the waveguides has been suggested [24]. With this technique, the frequency sensitivity due to critical transmission distances and matching junctions are reduced considerably. An illustration of such a waveguide array is shown in Figure 40.

For scanning a sector of 45° by 20° in azimuth and elevation, respectively, a drastic reduction in the waveguide opening is not required. A 25% iris will reduce radiation null effects, entirely, for these scan angles. In fact they are reduced almost entirely out to scan angles of $\pm 60^\circ$ which relates to an available sector coverage of 120° by 120° . The shift in the resonant null also results in a reduction in the magnitude of the grating lobe (a reduction of about 12 dB). Originally, for an open ended waveguide array grating lobe will appear to scan angles of $\pm 60^\circ$ while the resonant nulls will appear at $\pm 34^\circ$. With inductive irises grating lobes are not a problem at wide scan angles. The array matrix described in Figure 40 is an array with 25% irises. The array dimensions are given therein.

The number of phase shifters required for this system will be equal to the number of radiating elements. It is desirable that the phase shift increment be such that the pencil beam will be shifted so that crossovers between adjacent beam positions will be no lower than the -2 dB level. This corresponds to a beam increment of 0.65° for a 1° beam. The equations [25], [26] which relate the beam increment to the lowest order phase increment for an n-bit phase shifter system are

$$\frac{\Delta\theta}{BW} = \phi_0 \left[\frac{3}{2\pi} \right] \left[\frac{d}{D} \right] \left[1 - \frac{d}{2D} \right], \quad (97)$$

where $\phi_0 = 2\pi/2^n$ is the lowest order phase increment. For a conventional four bit phase shifter where $n = 4$ and $\phi_0 = 2\pi/2^4 = \pi/8$ and, in this case, $d/D = 1/70$, the beam displacement to the first beam increment off broadside is

$$\Delta\theta = 0.01056^\circ \quad (93)$$

for a 1° beamwidth. Therefore, it is seen that an almost continuous

scan of the 45° by 20° sector may be accomplished. The average granularity which relates to the average beam displacement between beam positions is

$$\frac{\overline{\Delta\theta}}{\text{BW}} = \frac{\phi_0}{\pi} \frac{d}{D} = 0.00178. \quad (99)$$

When related to the first beam increment off broadside the average granularity is

$$\frac{\overline{\Delta\theta}}{\Delta\theta} = \frac{(\phi_0/\pi) (d/D)}{\phi_0 (3/2\pi) (d/D) (1-d/2D)} = \frac{2}{3} \cdot \frac{1}{(1-d/2D)} \approx \frac{2}{3}. \quad (100)$$

This implies that the average granularity is approximately two-thirds the first beam increment. Hence, a normal four-bit phase shifter (i.e., phase shifts of $\pi/8, \pi/4, \pi/2, \pi$) may be used for beam steering with essentially no granularity problems.

It has been assumed here that a phase shifter will have to be employed at each element. Other phasing schemes have been developed where phase shifters have been placed in line along the feed system when using series-series feeds, series-parallel feeds, and parallel-series feeds [27]. However, these types of feeding systems usually require a larger number of phase shifters. A parallel corporate feed with individual phase shifters for each element would be the most cost effective configuration from a component price point of view. Each element-phase shifter pair would be fed through a closed waveguide type corporate feed. Each column of waveguide radiators would be fed by a one dimensional corporate feed. In this way a single source will have its energy divided equally between all elements.

A typical corporate feed is made of two-way power dividers in a tree network configuration. Unfortunately, this manner of feeding only becomes easily usable when the antenna system is made-up of 2^n radiating elements. In this system, 70 elements will be fed which will be cosine illuminated. It will be necessary, therefore, to employ two-way, five-way and seven-way power splitters utilizing an E-plane waveguide

multifurcation (Figure 41). This will resemble an E-plane horn with the horn opening supporting the multifurcation. This power splitting network will be designed such that the power at each output will be weighted so that the overall illumination intensity at each element will give a composite cosine illumination. The power is divided uniformly across the E-plane taper and, therefore, may be divided as a function of the ratio of the heights between the waveguide septa. Figure 42 and Figure 43 illustrate five-way and seven-way power dividers, respectively. The total feed system will consist of 994 five-way power dividers, 142 seven-way power dividers and 71 two-way power dividers. The special purpose power dividers could be machined using numerically controlled milling machines and interconnections would be made by standard rectangular waveguide.

It can be seen that a corporate feeding system of this type would be quite involved. The losses resulting from reflections and wall attenuation may be appreciable. They may even reach a point which would render this kind of feed undesirable. A space-fed array may be more acceptable from a simplicity of construction standpoint. This kind of feed system is composed of a pyramidal horn radiator which illuminates a planar receiving array, a planar transmitting array, and electronic phase shifters sandwiched between the arrays (Figure 44). The illumination of the planar surface would be somewhat like a cosine illumination with an array edge illumination of -20 dB. The same 4900 element array as in the corporate fed system would be used here.

Beam steering for the space fed array will be somewhat different than is required for a corporate feeding system. Since the primary pyramidal horn feed radiates energy in the form of a spherical wave, the element phase shifters must serve both to collimate and redirect the incident energy. The conventional corporate fed array does not require this basic collimation since this function is performed by the corporate distribution network [28].

Fixed phase shifters at each element may be added to the system which would compensate for the wavefront phase errors. However, this would be a costly alternative and quite undesirable. The individual element phase shifters could be commanded individually but this would greatly complicate the beam steering algorithm. The approach that should

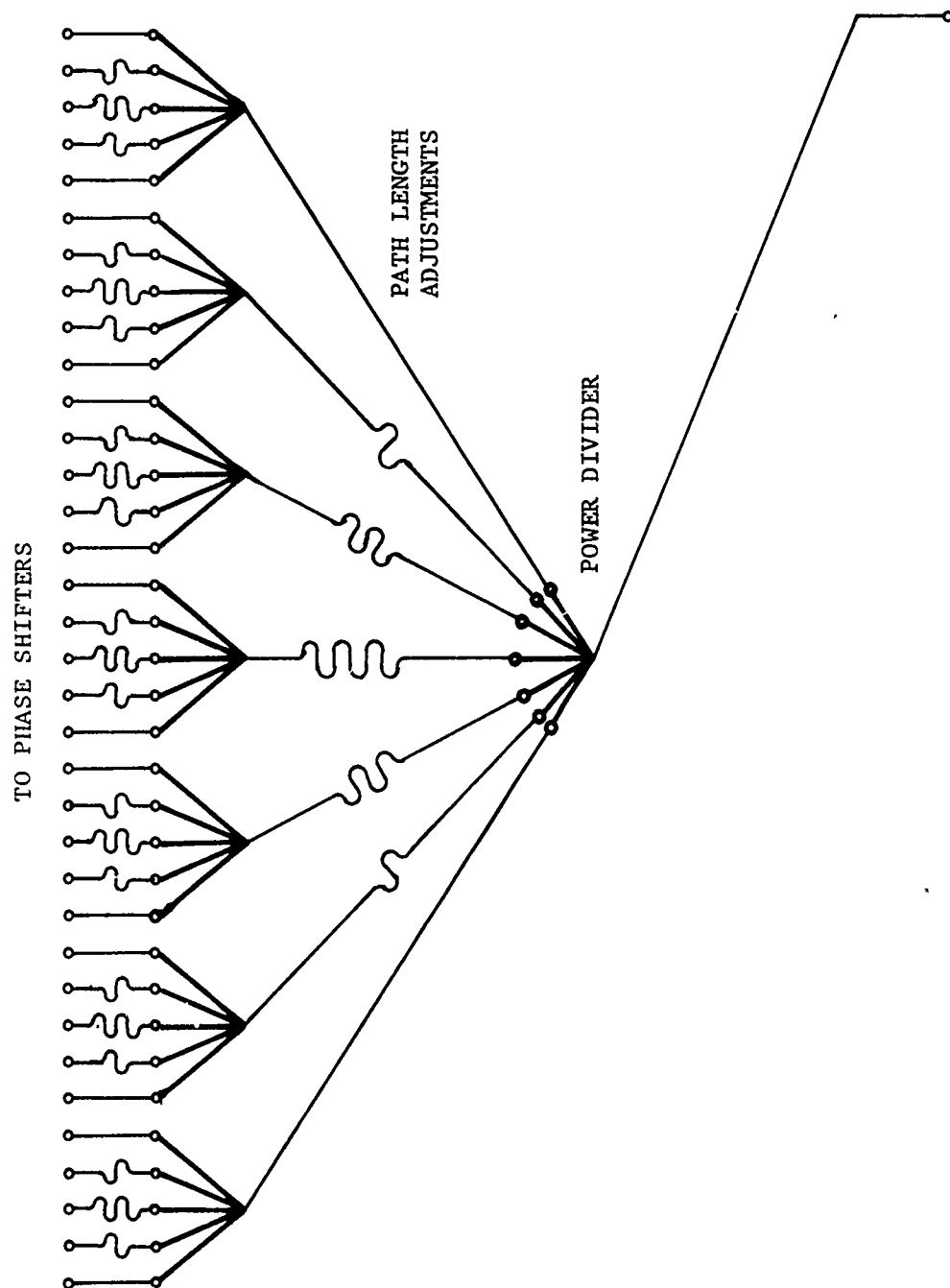


Figure 41. Corporate power division network.

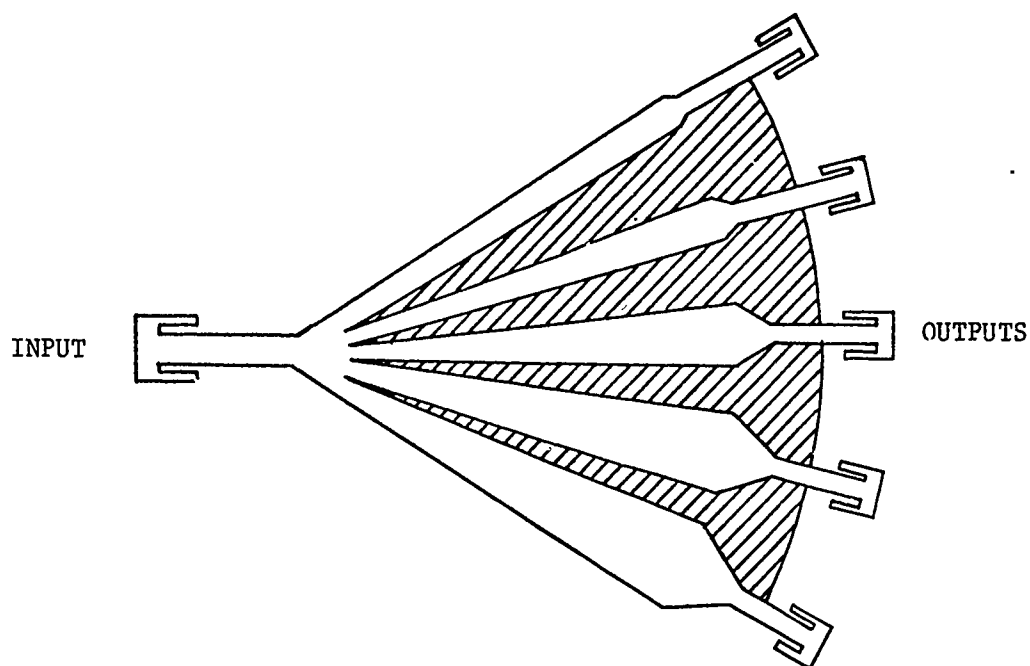


Figure 42. Five-way power divider.

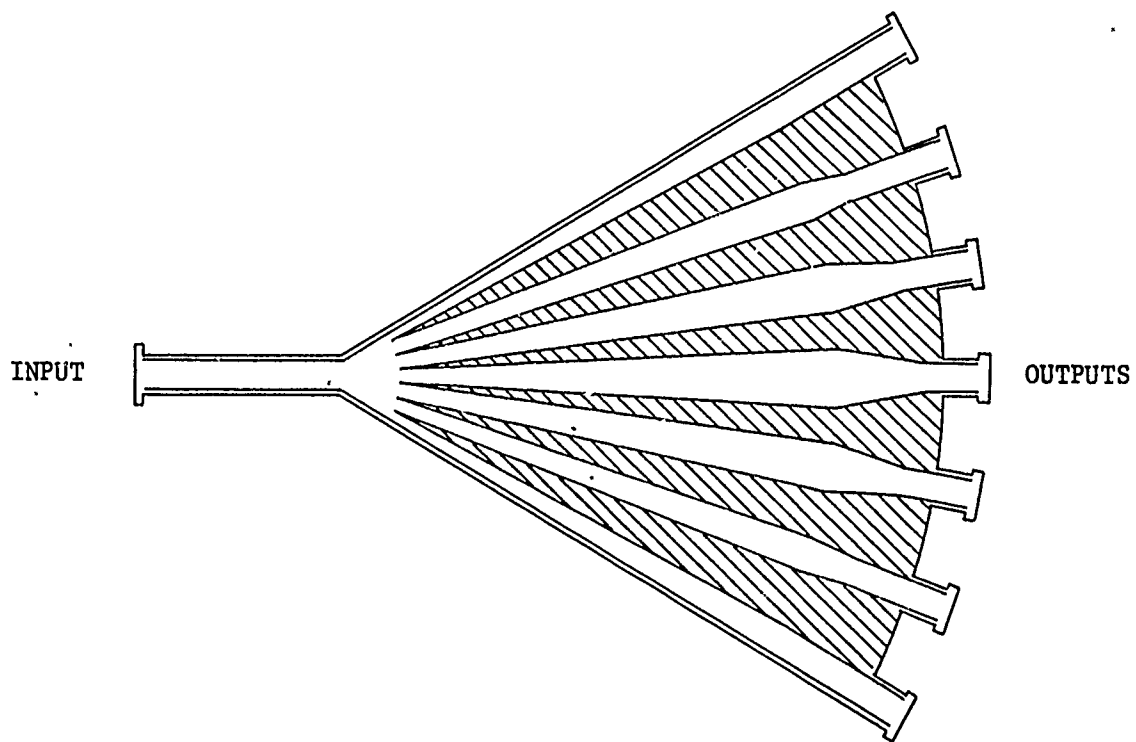
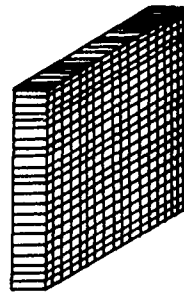


Figure 43. Seven-way power divider.

ARRAY

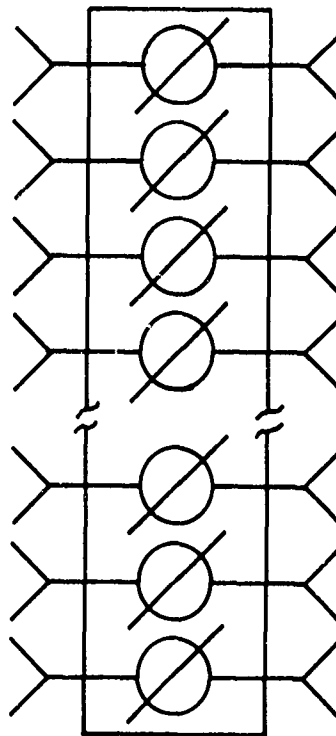


FEED

(a) Total System

PHASE
SHIFTER
BANK

INPUT
ELEMENTS



OUTPUT
ELEMENTS

(b) Array Components

Figure 44. Conceptual diagram of space-fed array

be taken is that beam steering should be performed through row and column commands. The difficulty here is that there is not perfect compensation for wavefront phase errors and some collimation error is introduced. This error results in some gain loss. Gain loss will remain negligible, however, when the focal length to aperture size ratio is kept near unity.

A means of reducing the complexity inherent in a planar electronic phased array is to reduce the system to a linear phased array by using an optical collimator for beam collimation and steering in one of the orthogonal directions. In that direction the collimation function could be performed by a reflector such as a parabolic cylinder while the scanning function would be accomplished by employing a flat splash plate which may be electromechanically dithered. Such an antenna arrangement is shown in Figure 45. The feed, which is the linear phased array, is illustrated by what appears to be a horn. The actual representation of the feed portion of the system is shown in Figure 45(b). The horn radiator is fed by rectangular waveguide. The lines connecting the waveguide horn inputs, the phase-shifters, and the corporate feed, may be either coaxial cables or rectangular waveguides. Beam steering commands are directed to the electronic phase shifters and to the electromechanical positioner which drives the splash plate. This system not only reduces systems complexity, but also greatly reduces cost.

C. Multiple Beam Forming Network

A multiple beam antenna is one having a number of independent beams with each pointing along a different direction and with each having an independently accessible input. Scanning is achieved by sequentially connecting the radar system to the different inputs. In comparing this type of antenna to the single beam electronic phased array discussed in the previous section, it should be noted that: (1) the multiple beam antenna (electronic beam forming network) requires more components such as hybrids and phase shifters, (2) the phase shifters of the multiple beam antenna are fixed as opposed to being responsive to a beam steering computer, and (3) the multiple beams can be completely independent (frequency, prf, etc.).

In the present application a multiple beam forming network can be used to feed a planar phased array or a line source. One method for

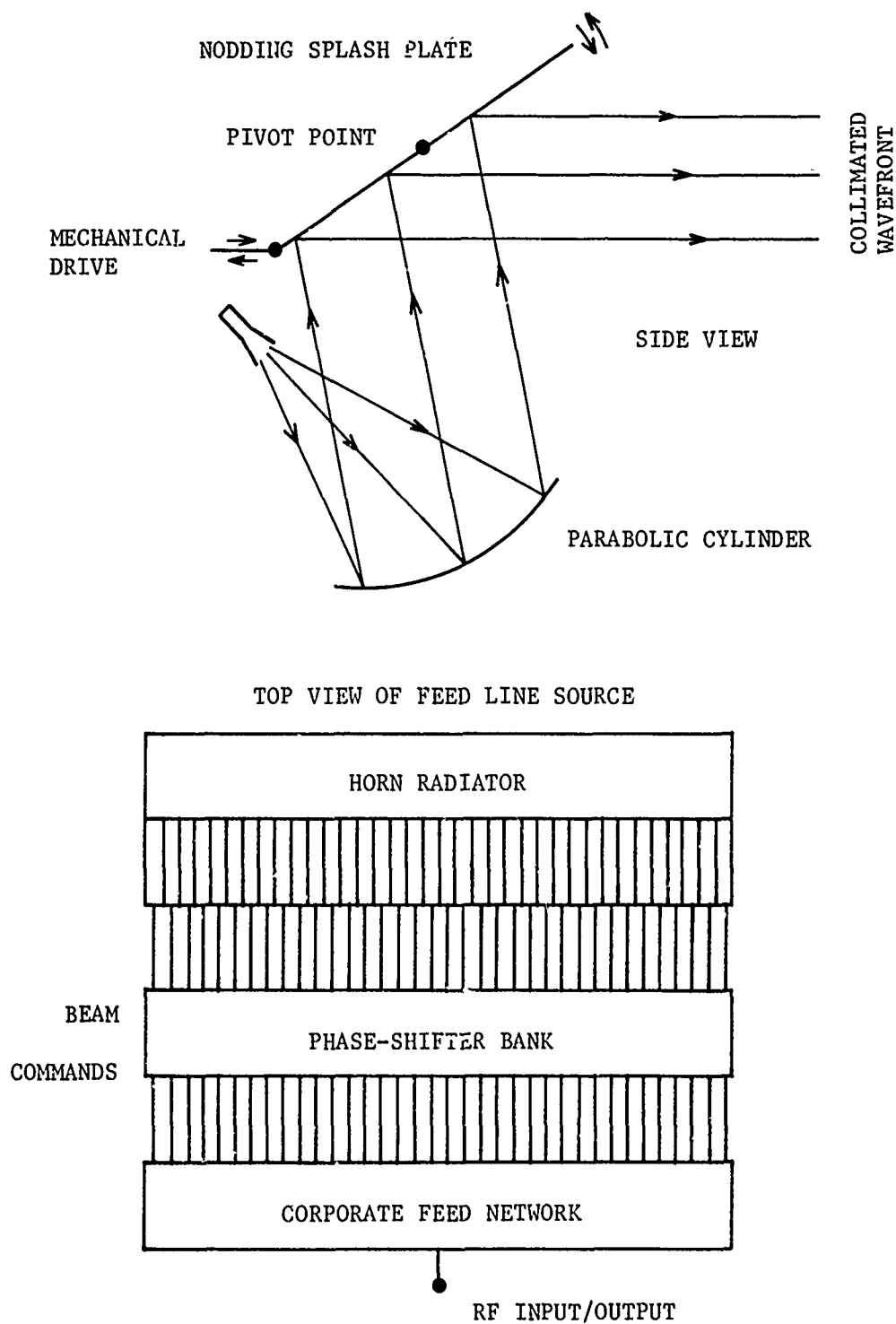


Figure 45. Simplified diagram of two-dimensional pencil-beam scanner utilizing electronic scanning in azimuth and mechanical deflection in elevation.

forming multiple beams would be to use a number of individual beam forming networks to control beam formation in the elevation direction and a separate set of matrices to form beams in the azimuth direction. These may be arranged in a physical matrix as described in the illustration, herein (Figure 46) [29],[30].

The number of outputs in the beam forming network is defined by the number of elements along a linear array which will give the desired half-power beamwidth (on the order of 1° for this application) in the plane of the array elements. The array illumination should be similar to a cosine distribution so that sidelobes may be kept to an acceptable level (possibly -23 dB). These two considerations when coupled place a difficult requirement on the design of the beam forming matrix. Typically, a beam forming network is composed of 2^n inputs and outputs. This corresponds to the formation of 2^n beams. There are ways of feeding an array of $N \neq 2^n$ elements which will still give 2^n beams. The actual beam forming matrix will still consist of 2^n inputs and outputs with an additional circuit between it and the radiating elements. In general, one would probably allow the beamwidth to increase or decrease slightly so that the sector width corresponds to 2^n beams.

The multiple beam forming network is the starting point from which to build the entire feeding system. Its circuitry consists of $N/2 \log_2 (N/2)$ electronic phase controls and $(N/2) \log_2 (N)$ hybrid couplers. In a planar array with cosine illumination the number of elements of $f_o = 23$ GHz will be a matrix of 70×70 elements. The closest number to 70 would be $N = 2^n = 64$ elements. The entire beam forming system will require

$$\left((64)^2 / 2 \right) \log_2 (64)^2 = 24,576 \quad (101)$$

hybrids and

$$\left((64)^2 / 2 \right) \log_2 \left((64)^2 / 2 \right) = 20,480 \quad (102)$$

phase shifters.

A diagram of a multiple beam forming matrix for a linear array is shown in Figure 47, [31]. This illustrates half of the network. Each input

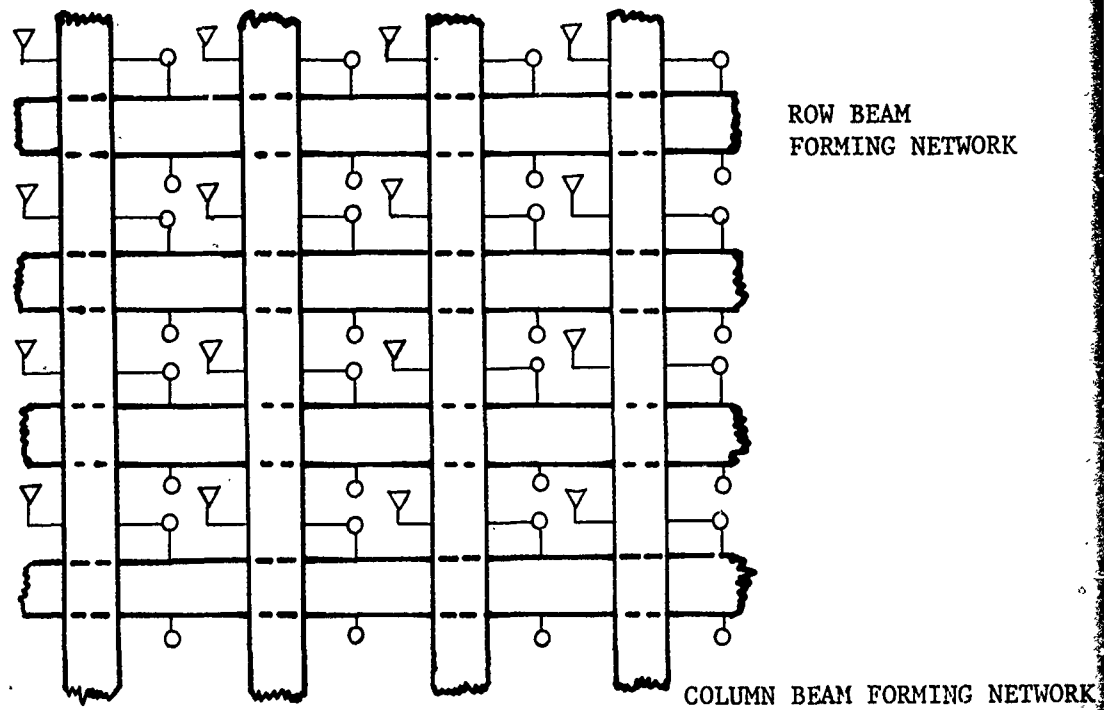


Figure 46. Multiple beam forming matrix for planar array.

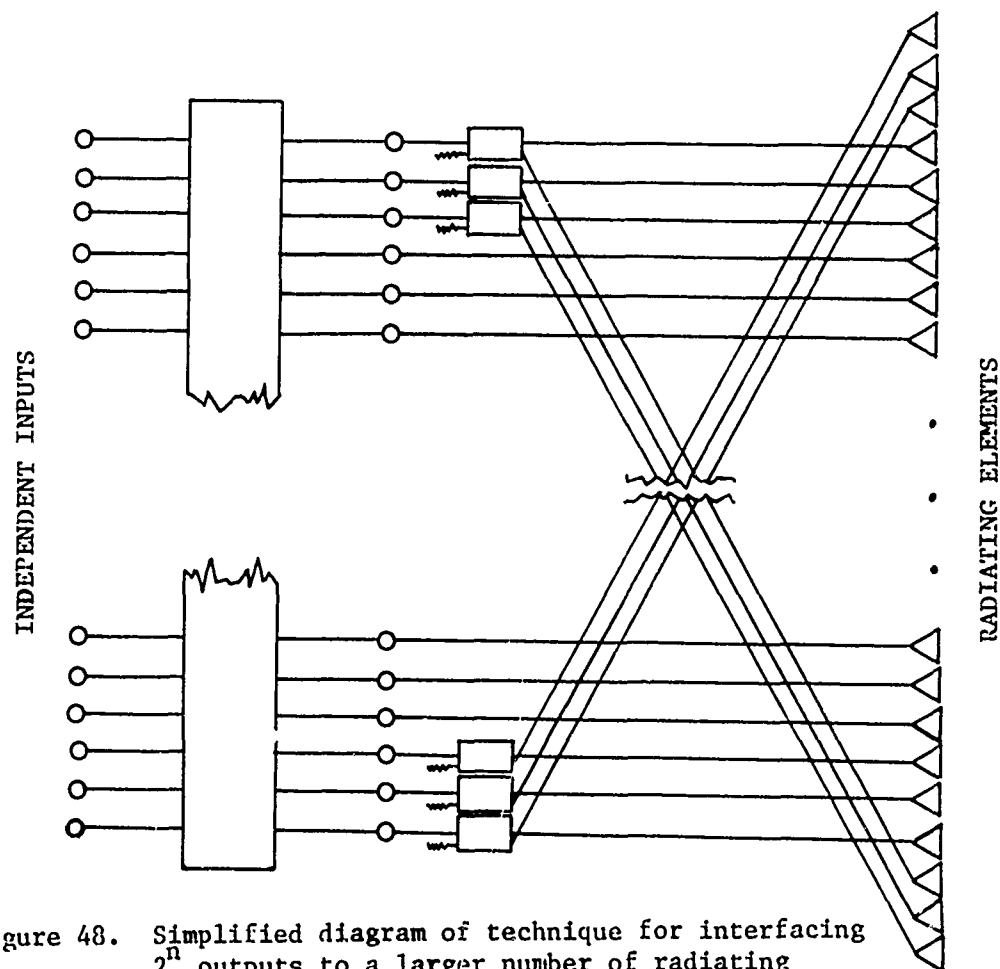


Figure 48. Simplified diagram of technique for interfacing 2^n outputs to a larger number of radiating elements.

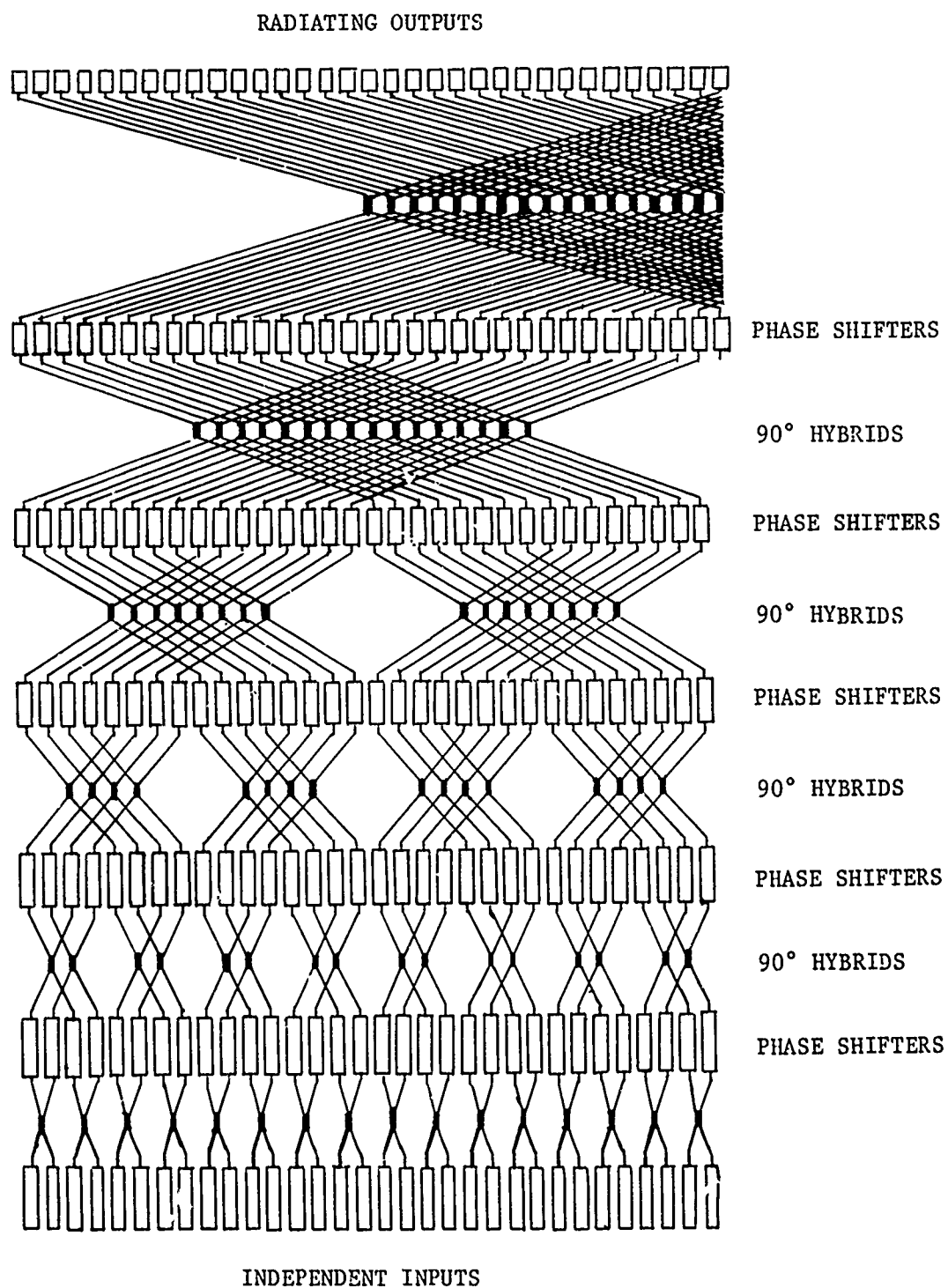


Figure 47. Simplified conceptual diagram of Butler matrix beam forming network.

corresponds to one beam in the output. This will allow each beam pointing direction to be accessed through a switching system rather than having to program a beam steering computer to control digital phase shifters. All phase shift elements are fixed in the multiple beam forming network.

Thus far, a beam forming matrix with 64 inputs and 64 outputs has been described. It is necessary that this network feed 70 antenna ports (along a single array column). Therefore, the existing network's output will have to be altered. Since a cosine illumination is desired, it is obvious that the field intensity of the outside elements must be substantially reduced in comparison to those along the central region of the array. As shown in Figure 48, the three elements on either end of the array column will be fed through an additional circuit of 180° hybrids [32]. The phase shift between adjacent elements in this system can be found from the relation

$$\Psi_p = (p\pi/N)(2 - 1/|p|), \quad (103)$$

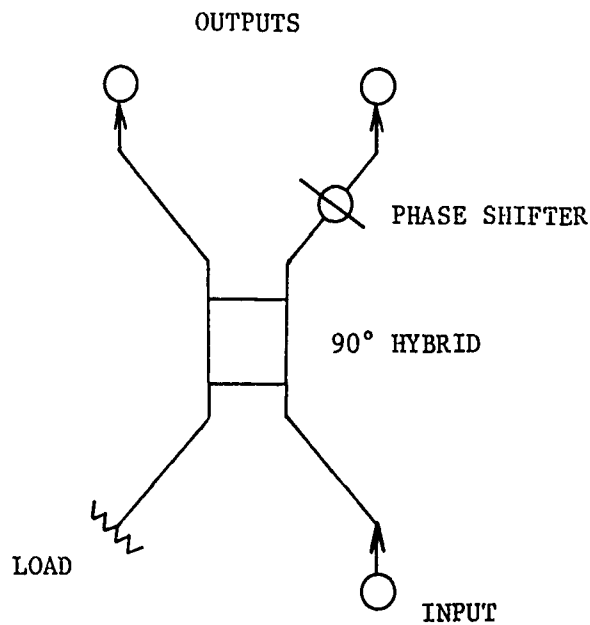
where p is an integer indicating the beam of interest and having values

$$-N/2 \leq p \leq N/2, \quad (104)$$

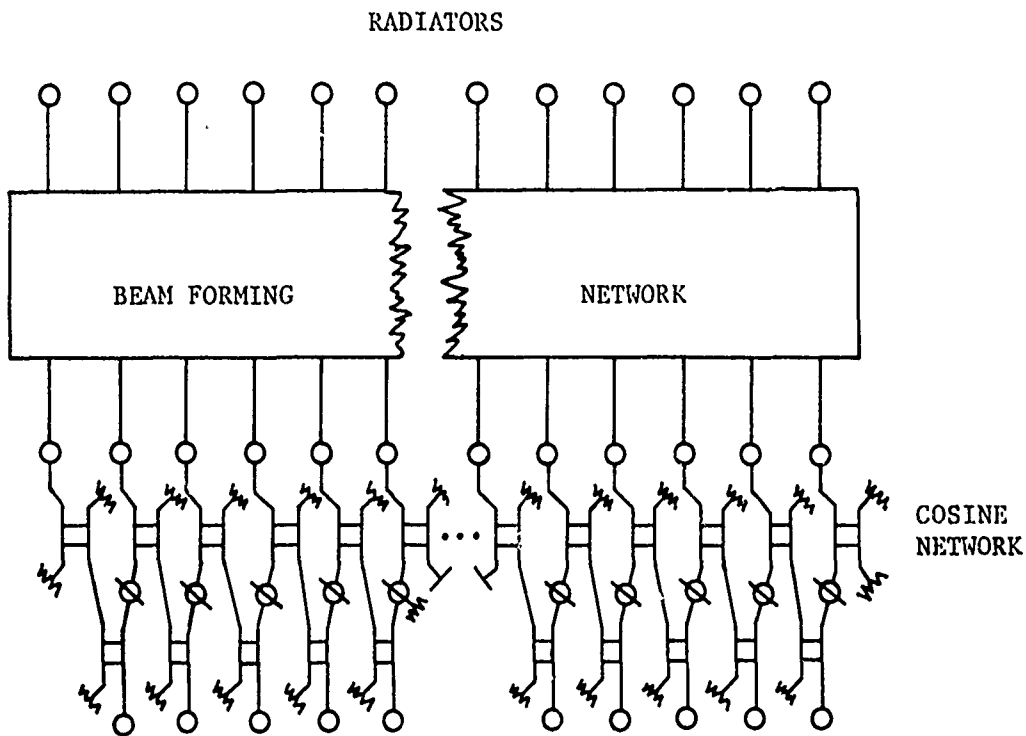
and

$$N/2 = 32. \quad (105)$$

The beaming forming matrix has been designed, and an additional circuit has been described which will match the 64 output beam forming matrix to the 70 element array. It will now be necessary to develop the input circuit which will produce a cosine illumination at the output. The basic building block of this kind of circuit is shown in Figure 49(a). This circuit consists of a 90° hybrid and a phase shifter which is fixed at a value which will give the required phase center relationship between beams to give a composite cosine illumination at its output. The actual input circuit configuration for the 64 input beam forming network is shown in Figure 49 (b). The addition of this circuit reduces the number of cosine beams formed to 63. This reduces the number of



(a) Individual Components



(b) Total Network

Figure 49. Network components for producing cosine aperture illumination.

row beam forming networks to 63. The row beam matrices will reduce 70 outputs to 63 inputs. Hence, an array of 63 by 63 inputs which correspond to a sector of space of 63° by 63° of individual 1° cosine beams. Since a sector of 20° by 45° is desired, one needs access only those inputs which correspond to coverage of that sector [33].

Originally the number of hybrids were calculated for beam forming matrices which would provide uniform illumination to 2^N elements. That number has been increased due to the fact that the additional input and output circuits were added. The addition of the output circuits adds

$$6(N + 6) + 6(N - 1) = 798 \quad (106)$$

when $N = 64$. The addition of the input circuit increases the number of hybrids by

$$(2N - 1) \left[(N + 6) + (N - 1) \right] = 16,891. \quad (107)$$

Due to the fact that the input circuit reduces the number of inputs for the column matrices to 63, one less row matrix is required which reduces the number of hybrids by $N/2 \log_2 N = 192$. The total number of hybrids required for this system is then

$$\begin{aligned} (N^2/2) \log_2(N^2) + 6 \left[(N + 6) + (N - 1) \right] + (2N - 1) \left[(N + 6) + (N - 1) \right] \\ - (N/2) \log_2 N = 42,265 \end{aligned} \quad (108)$$

This alone is a prohibitive factor from a cost and assembly point of view.

The number of phase shifters required for the input circuits may be found by the expression

$$N_i = (N - 1) \left[(N + 6) + (N - 1) \right]. \quad (109)$$

The number required for the matrix circuits is expressed by

$$N_m = (N^2/2) \log_2 (N/2)^2. \quad (110)$$

A number of phase shifters may be subtracted from the total by the same argument as in the previous paragraphs thus requiring one less row control. This reduction in phase shifters may be found from

$$N_r = (N/2) \log_2(N/2). \quad (111)$$

Therefore, the number of phase shifters required is given by

$$N_t = N_m + N_i - N_r = 28,699. \quad (112)$$

The actual price of this type of system would be determined, to a large degree, by the price of these two components. Supposing that at this quantity the price per coupler is \$20, then the total coupler expense would be \$845,300. A nominal price for electronic phase shifter at such large quantities would be \$50 giving a total price of \$1,434,950. This gives a total antenna systems component price of \$2,280,250 + which is an entirely prohibitive figure.

The expense of such a system could be reduced greatly if the planar array could be replaced by a linear array of 70 elements. This array would produce 20 fan beams of 1° beamwidth in the narrow dimension for elevation coverage. The beam forming network would be of the same configuration as that shown in Figure 47, and it would have the same input and output circuitry. The number of hybrids would be reduced to

$$(N/2) \log_2(N) + 6(2N - 1) = 325. \quad (113)$$

The number of phase shifters now required would be

$$(N/2) \log_2(N/2) + (N - 1) = 223. \quad (114)$$

This would reduce the total component price to approximately \$55,000.

The additional hardware required to focus the fan beams in the wide dimension would be a parabolic cylindrical reflector. The result would be a line of pencil beams which could be scanned through the use of a tiltable flat splash plate. This is similar to the scheme illustrated

A number of phase shifters may be subtracted from the total by the same argument as in the previous paragraphs thus requiring one less row control. This reduction in phase shifters may be found from

$$N_r = (N/2) \log_2(N/2). \quad (111)$$

Therefore, the number of phase shifters required is given by

$$N_t = N_m + N_i - N_r = 28,699. \quad (112)$$

The actual price of this type of system would be determined, to a large degree, by the price of these two components. Supposing that at this quantity the price per coupler is \$20, then the total coupler expense would be \$845,300. A nominal price for electronic phase shifter at such large quantities would be \$50 giving a total price of \$1,434,950. This gives a total antenna systems component price of \$2,280,250 + which is an entirely prohibitive figure.

The expense of such a system could be reduced greatly if the planar array could be replaced by a linear array of 70 elements. This array would produce 20 fan beams of 1° beamwidth in the narrow dimension for elevation coverage. The beam forming network would be of the same configuration as that shown in Figure 47, and it would have the same input and output circuitry. The number of hybrids would be reduced to

$$(N/2) \log_2(N) + 6(2N - 1) = 325. \quad (113)$$

The number of phase shifters now required would be

$$(N/2) \log_2(N/2) + (N - 1) = 223. \quad (114)$$

This would reduce the total component price to approximately \$55,000.

The additional hardware required to focus the fan beams in the wide dimension would be a parabolic cylindrical reflector. The result would be a line of pencil beams which could be scanned through the use of a tiltable flat splash plate. This is similar to the scheme illustrated

in section V.B (see Figure 45). All twenty beams could be illuminated simultaneously while scanned in azimuth. Alternatively, all beams could be illuminated sequentially so that a combination of azimuth scanning (through beam switching) and elevation scanning (utilizing the splash plate) would result in a raster scan of the 20° by 45° sector.

D. Rotman Lens

The Rotman lens [33,34] is a beam forming network which is applicable to electromechanical scanning, multiple beam operation, or electronically scanning a single beam. The Rotman lens is one of several types of parallel plate lenses which is of simple construction and is capable of serving as a scannable line source. This lens may be used to scan a single beam over its aperture by switching between inputs, or as a system which will support multiple beams at desired beam positions. The lens utilization is a function of the antenna application. It may be designed to give a perfect focus at three widely separated points along its scan path. There is some degradation of the plane wavefront produced at different feed points away from these foci; however, a high degree of collimation is still possible at these points.

Rotman lens design is defined in part through the use of three coupled equations which are a function of lens geometry (see Figure 50). The lens and associated structure may be specified in a systematic way as follows:

- (1) Since a 1° half power beam width is desired, the aperture dimensions are found from the approximate relationship

$$BW = 65\lambda/D = 1^\circ \quad (115)$$

- (2) A prior knowledge of the desired angle coverage is also specified. This angle coverage (α) expressed in radians is required to define the normalized (with respect to focal length) distance, g , between the rear portion of the lens and the circular focal arc.

$$g = 1 + \alpha^2/2 \quad (116)$$

This normalized distance is the key parameter in the simultaneous equations whose solution gives the normalized lens coordinates.

$$y = \eta(1 - w) \quad (117)$$

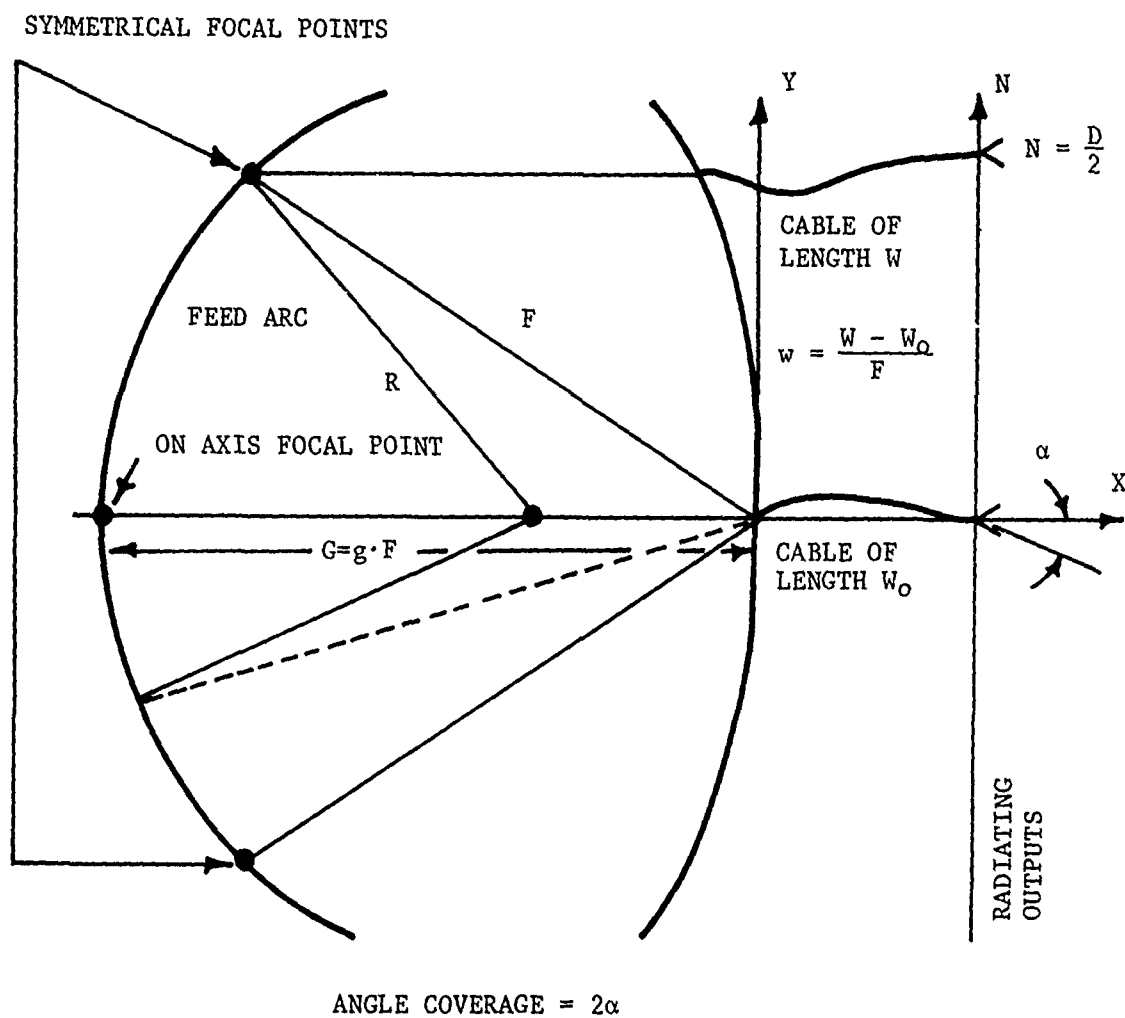


Figure 50. Simplified diagram of Rotman lens geometry.

$$x^2 + y^2 + 2gx = w^2 - 2gw \quad (118)$$

$$aw^2 + bw + c = 0 \quad (119)$$

where,

$$a = (1 - g)^2 / (g - a_o)^2 + \eta^2 - 1 \quad (120)$$

$$b = 2a_o \left(\frac{1 - g}{g - a_o} \right) - \left(\frac{(1 - g)}{(g - a_o)^2} \right) b_o^2 \eta^2 + 2(1 - \eta^2) \quad (121)$$

$$c = \frac{b_o^4 \eta^4}{4(g - a_o)^2} - \frac{b_o^2 \eta^2 a_o}{(g - a_o)} + \eta^2 (1 - b_o^2) \quad (122)$$

$$a_o = \cos \alpha, \quad b_o = \sin \alpha, \quad (123)$$

and the range of η is

$$0 \leq \eta \leq \eta_{\max} \quad (124)$$

where η_{\max} for an optimum lens is known.

- (3) Focal length is a function of the aperture size and must be found so that the normalized lens coordinates can be expressed in measurable units.

$$F = D/2 \eta_{\max} \quad (125)$$

- (4) The radius of the circular focal arc may then be defined.

$$R = (F^2 + G^2 - 2FG \cos \alpha) / (2G - 2F \cos \alpha). \quad (126)$$

The input radiating elements are placed along this arc. This is also the surface along which the three points of perfect focus lie. The two symmetrical off-axis focal points define the extreme edges of the circular focal arc while the on-axis focal point is at the arc center.

- (5) The lens equations may now be solved. Their solution will give the normalized lens coordinates which must be multiplied by the focal length.

After the lens coordinates have been calculated the lens phase error for the off-foci inputs may be determined from the following equation.

$$\Delta\phi = k \Delta L = \frac{2\pi}{\lambda} F \left[(h^2 + x^2 + y^2 + 2hx\cos\theta - 2hy\sin\theta)^{1/2} - h + w + \eta\sin\theta \right] \quad (127)$$

where,

$$h = (1/F) \left[(G-R) \cos\theta + \sqrt{(G-R)^2 \cos^2\theta - G(G-2R)} \right] \quad (128)$$

and θ varies from 0° to α .

The procedure is to choose the lens coordinates such that the phase error is minimized as different points are investigated along the circular focal arc. There will be no phase error at the points of perfect focus. Hence, the intermediate points are those to be scrutinized. This procedure will give the coordinates for an optimum lens for a given aperture size and angle coverage.

In the present antenna requirement, there is need for a sector coverage of $20^\circ \times 45^\circ$ in elevation and azimuth, respectively. The Rotman lens may be used to scan either the azimuth or elevation portion of the sector and some reflecting collimator must be used to scan the orthogonal plane. Several methods of feeding the lens structure are available, and their relative advantages and disadvantages will be discussed. Lens structures with sixteen inputs will be illustrated for discussion purposes; although, actual systems would probably use many more than this.

The first configuration is a lens fed by a single source through a corporate feeding system (Figure 51). The feed system will be interrupted at its division points by electronically controlled switches. Full transmitter power will be applied to each element as that element is switched into the circuit. The element being illuminated will be accessed long enough so that the desired number of pulses from the target will be received, then the switching system will move sequentially to

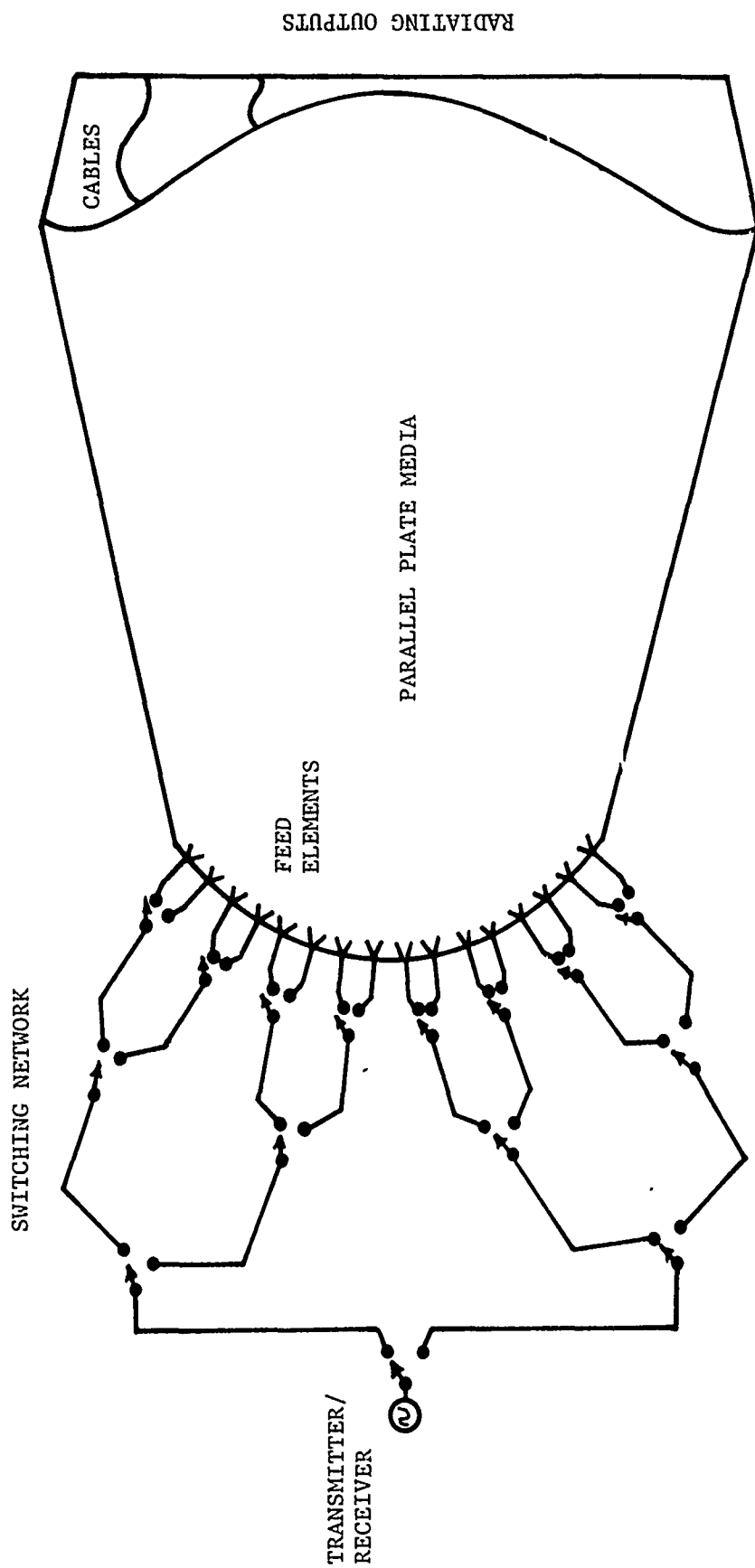


Figure 51. Rotman Lens with electronic switch network for connecting a single transmitter/receiver to each beam port.

the next element. In this way the Rotman lens will be capable of scanning individual beams across the spacial region of interest.

The second Rotman lens feed arrangement utilizes a corporate feed which divides the input power into sixteen equal divisions (Figure 52). Each radiator is illuminated and sixteen beams are formed. The total energy impinging upon a target is reduced radically requiring a source of higher power than in the previous case. Energy reflected from the target will be received from the radiating aperture through circulators used to separate the transmit/receive ports. Intensity levels at each of the receiver ports may be compared to resolve the target direction. This system requires the same number of receivers as beams and has a gain inversely proportional to the number of beams.

A third feeder possibility for the same lens configuration would be to use a separate source for each input radiating element (Figure 53). This would greatly increase the on target power, and as a result, the received signal would be substantially increased. Again, the actual target direction could be defined by comparing the received signal level at each antenna port. The requirement for a number of sources equal to the number of beams is obviously unattractive.

Fourthly, a Rotman lens and a single energy source may be used through the implementation of a mechanically rotating ring switch feed (see Figure 54(b)). The only alteration to the original lens structure would be the individual input devices. This curved input section would correspond to the radius of a small circle (Figure 54(a)) where the arc should be large enough so that the VSWR generated by the arc could be held to a minimum. As the ring switch scans the input, continuous scanning of the desired solid angular region is performed.

Each of the above mentioned designs form fan beams with the narrow width corresponding to the 1° beamwidth required. In the orthogonal plane, a parabolic cylinder may be used to focus the fan beam to a 1° pencil beam. Scanning in the elevation plane may be achieved through the use of a flat "splash plate" which may be mechanically tilted (same principle as depicted in Figure 45(a) and (b)). This method of scanning has been used successfully in other applications and has merit for this system. It is felt that a review of the methods previously mentioned

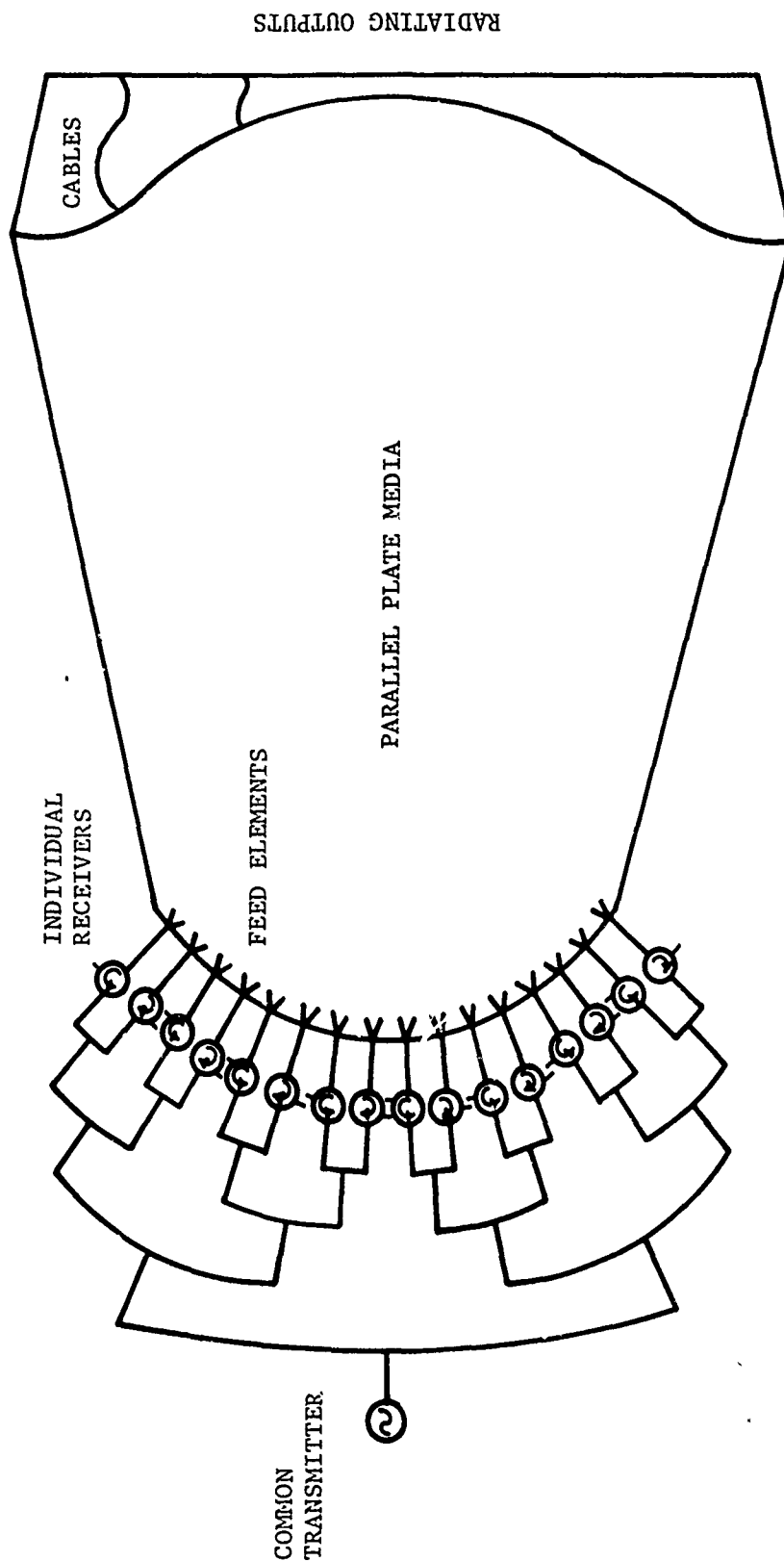


Figure 52. Rotman lens which forms multiple beams on transmit. Target directions are determined by received signal intensity at receiver ports.

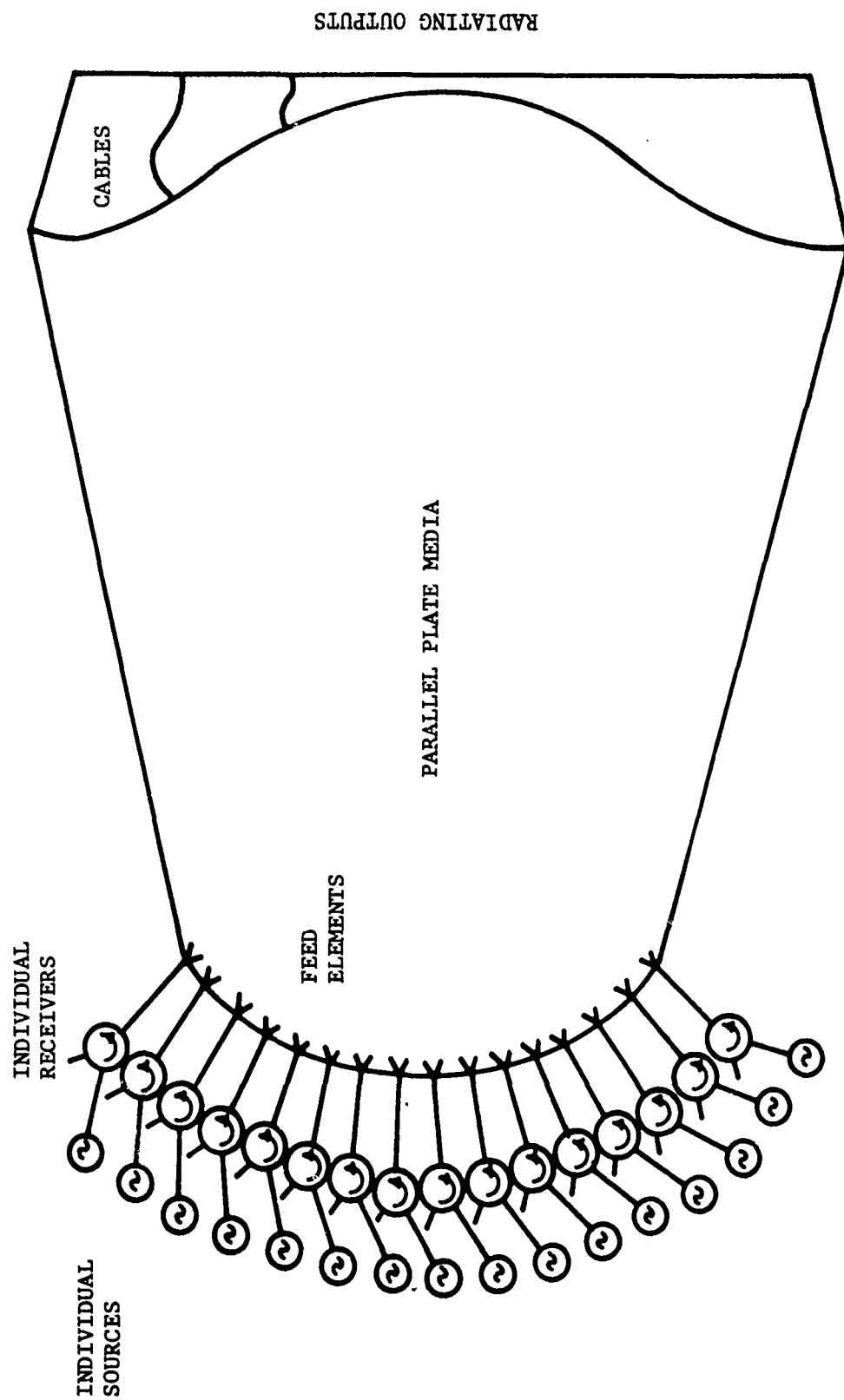
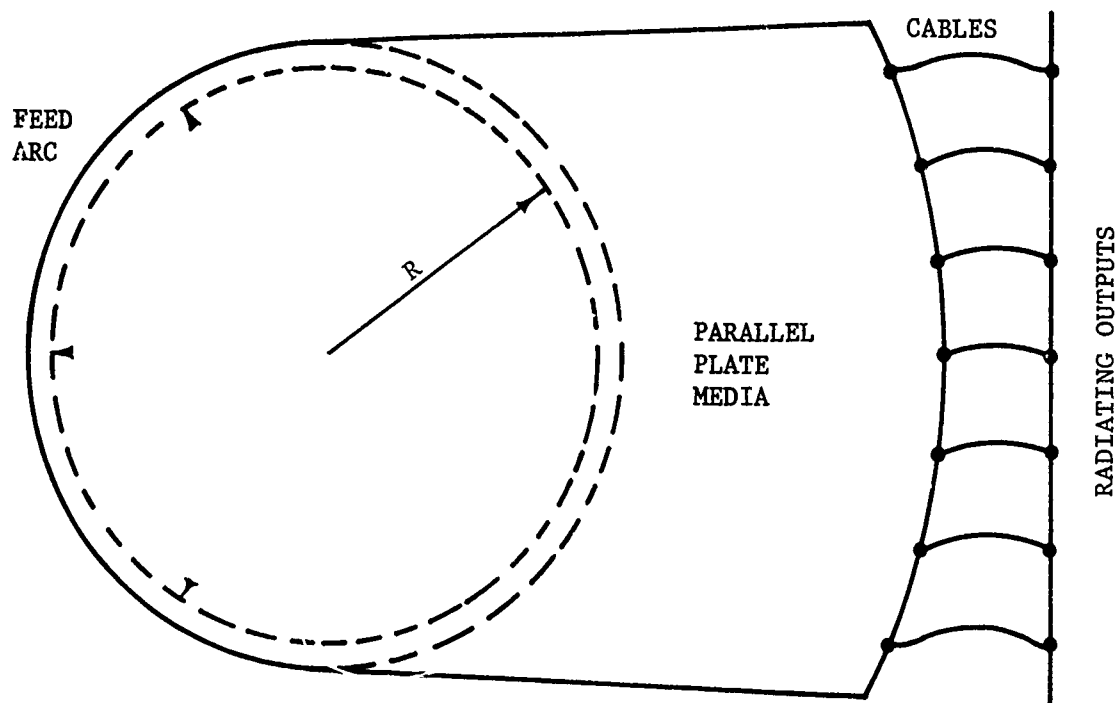
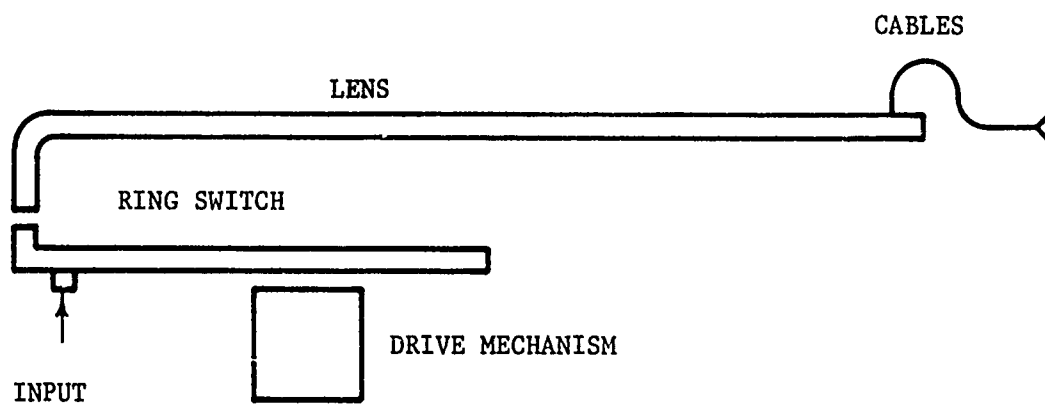


Figure 53. Rotman lens with individual sources for each lens input.



(b) Top view showing ring switch



(a) Side view

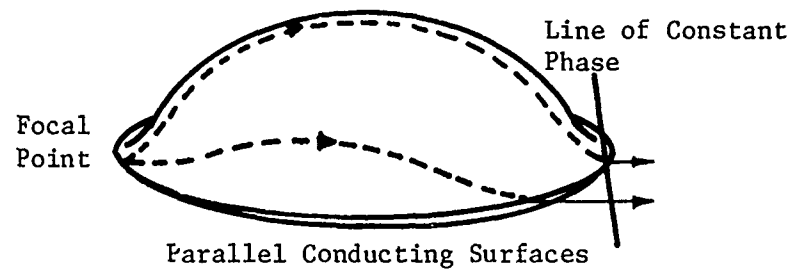
Figure 54. Simplified diagram of Rotman lens fed by ring switch.

would be helpful. The first lens feed configuration is a straight forward means of feeding a Rotman lens which allows one to scan the search sector by moving the beam through discrete positions. The controller for switching would probably have to be a small minicomputer or microcontroller which would require an additional expense to be added to the system cost. The second approach utilizes a corporate feed to transfer the energy from a single source to the lens inputs. The transmit and receive port isolation is accomplished through the use of circulators. This is a less expensive method, however, less energy is radiated in each beam since all beams are illuminated simultaneously. Still concerned with the theme of illuminating all beams at once, method three utilizes an individual source per input. This affords higher on target power but with a much greater expense. Number four is concerned with the idea of feeding the lens with a ring switch feed. This is the most simplified and yet dependable way of feeding the lens. Individual stationary beam positions are not realized, but rather, one beam moves continuously. The chief drawback to the use of the Rotman lens in this application is the anticipated frequency of operation. Unfortunately, this particular lens relies on the use of a set of coaxial cables for phase equalization, and coaxial cables are extremely lossy, small, and difficult to work with at millimeter wavelengths. Consequently, the Rotman should not be considered a candidate above 18 GHz.

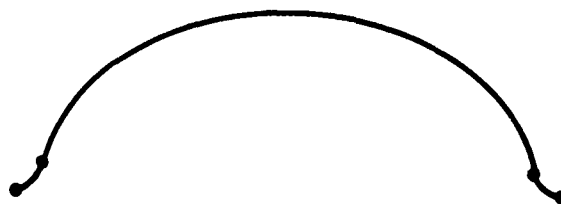
E. Geodesic Luneberg Lens

As stated in the previous section, the Rotman lens is a very simple device since it consists of flat parallel plate and coaxial cable, but the coaxial cable aspect becomes unattractive at frequencies above about 18 GHz. Another parallel plate lens which is slightly more difficult to fabricate but which is suited for operation as high as 95 GHz is the geodesic Luneberg lens.

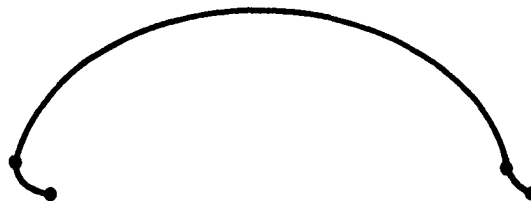
The geodesic Luneberg lens is a waveguide analog of a two-dimensional slice through a Luneberg lens. In essence, it is a rotationally symmetric "hump" in a pair of parallel plates which serves as a phase equalizer for energy propagating over the hump. In fact, any bundle of rays which diverges from a single point on the lens' surface spreads out (as shown in Figure 55) so as to emerge from the other side of the



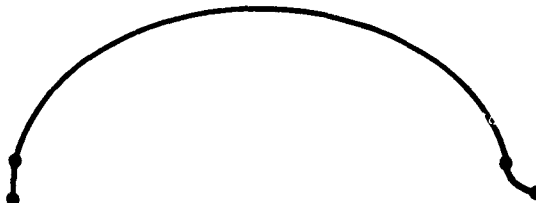
Conceptual diagram of a parallel plate geodesic lens showing two different rays which travel equal path lengths between a point and a line of constant phase.



(a) Tin-Hat



(b) Clam-Shell



(c) Helmet

Figure 55. Section through the center of a geodesic lens illustrating three generic input schemes and their designations.

lens in a line of constant phase. Thus, the geodesic lens offers the ability to form a collimated line source whose direction of propagation varies linearly with the position of a single feed point. The mathematics of the geodesic Luneberg lens are quite rigorous and need not be repeated here; however, the interested reader is referred to Johnson's classical paper on the subject [35]. The input and output lips of the lens may be designed so that the primary energy enters the lens: (1) from the exterior of the lens and perpendicular to its axis of rotation (Tin Hat); (b) interior and perpendicular to this axis (Clam Shell); or (c) parallel to the axis from below (Helmet), as shown in Figures 55(a), (b) and (c), respectively [35].

Even though this device has the capability to scan 360° , this is usually not done, since input (feeds) and output sections (radiators) are attached, thereby lowering the useful sector to sizes on the order of 90° . This situation is illustrated in Figure 56, which depicts the top view of a typical scanning line source system. Note that flat-plate extensions which increase the aperture size with increasing scan angle must be added to the lens to avoid aperture blockage.

One significant aspect of the geodesic lens antenna that has not yet been discussed is a feed which must couple energy to the lens while moving through an arc parallel to and very slightly separated from the lens input contour. Also, a single rotating feed would be active only over the region $\pm \theta$ in Figure 56, thereby creating a very large dead time. Both these problems can be solved by use of a ring switch (see Figure 57) which is a device for sequentially switching energy from a stationary waveguide into a number of circularly moving waveguides each of which is activated as it moves through the feed region. The design of such a switch is a nontrivial task, especially at millimeter wavelengths, since close mechanical tolerances must be maintained to avoid binding, steps must be taken to prevent RF leakage, and passive devices for sequentially activating the feeds must be included. Johnson [36] provides a concise survey of the available designs, along with references where more detailed information may be obtained.

The possible uses of the geodesic lens in radar systems are many; however, it is usually configured as shown in Figure 58, where the

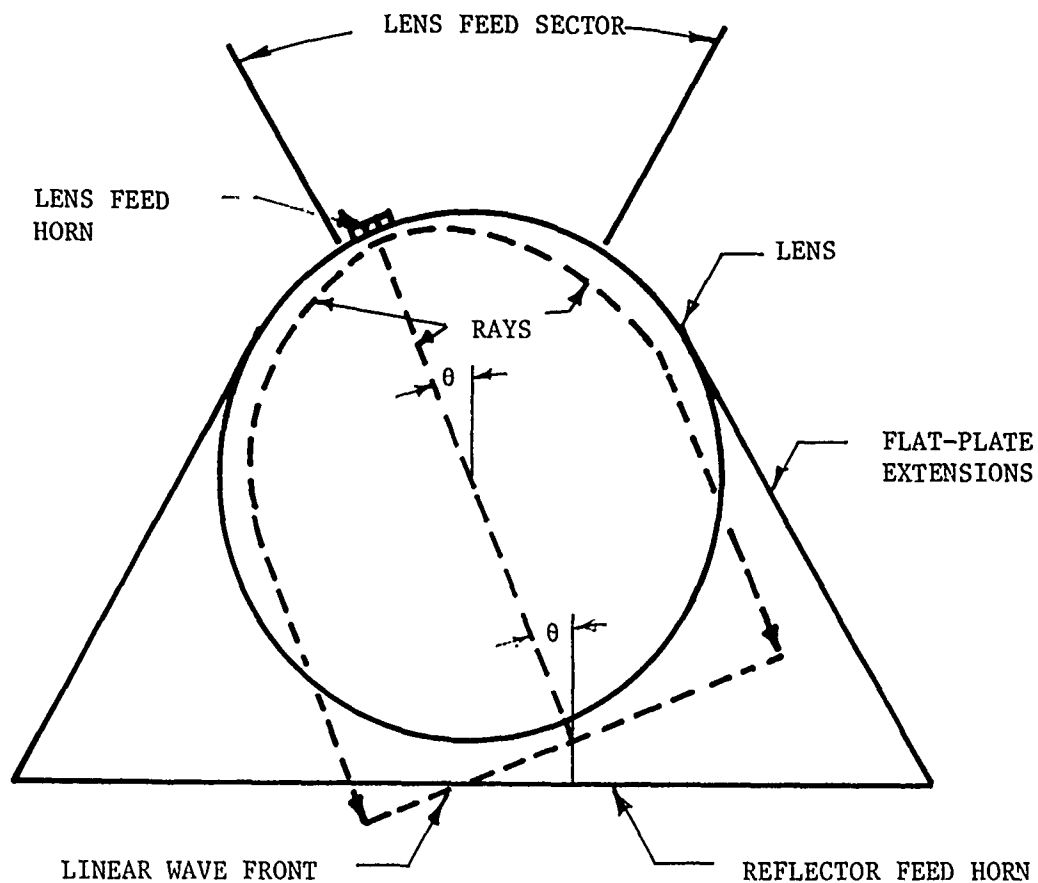


Figure 56. Top view of a geodesic lens showing the ray paths when the feedhorn is displaced by angle θ from the center of the lens feedsector.

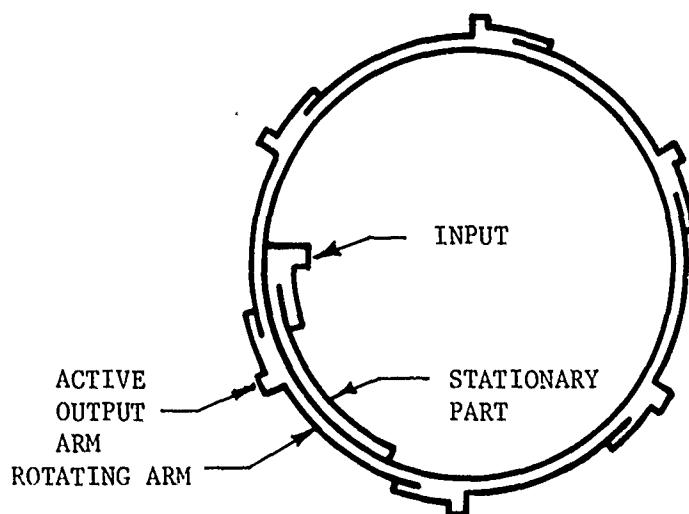


Figure 57. Typical multi-port ring switch used for rapidly scanning a geodesic lens.

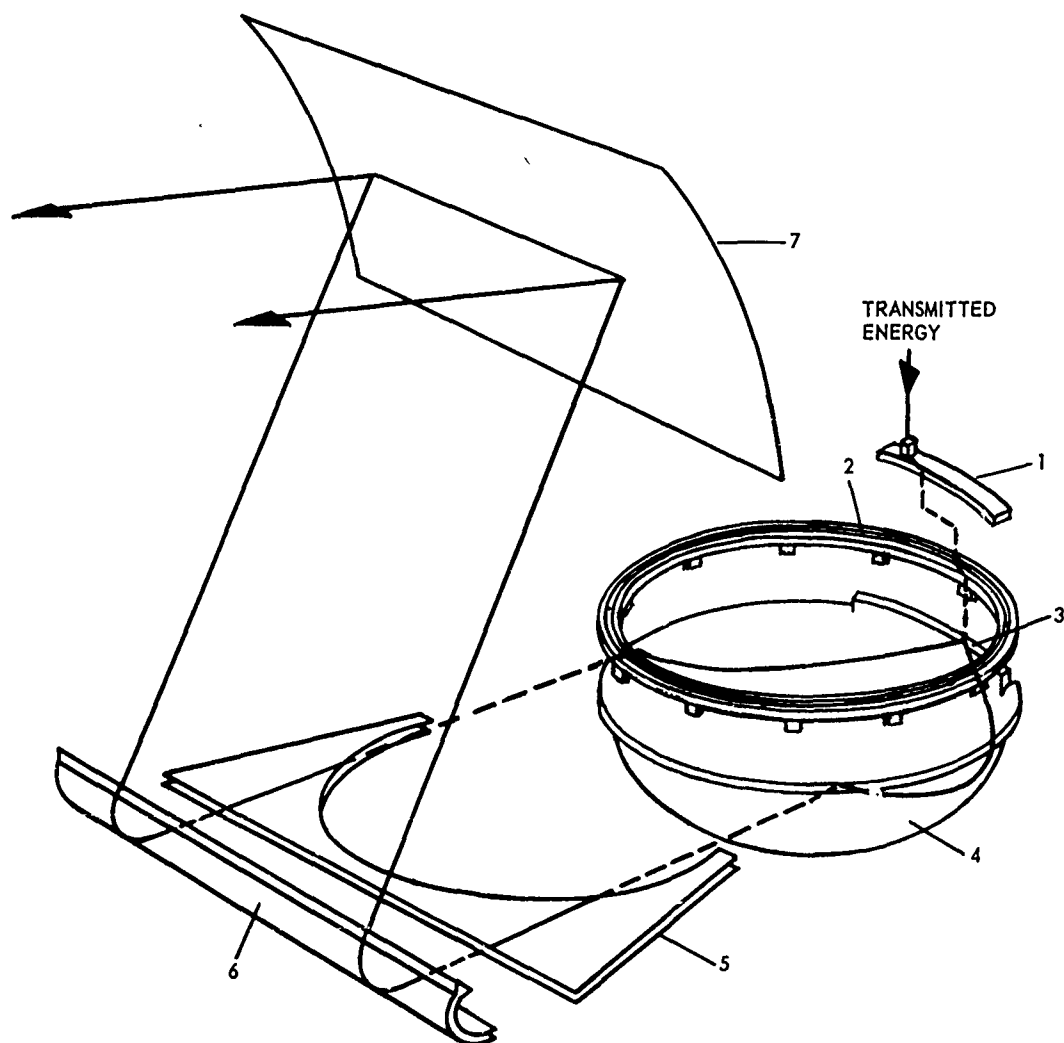
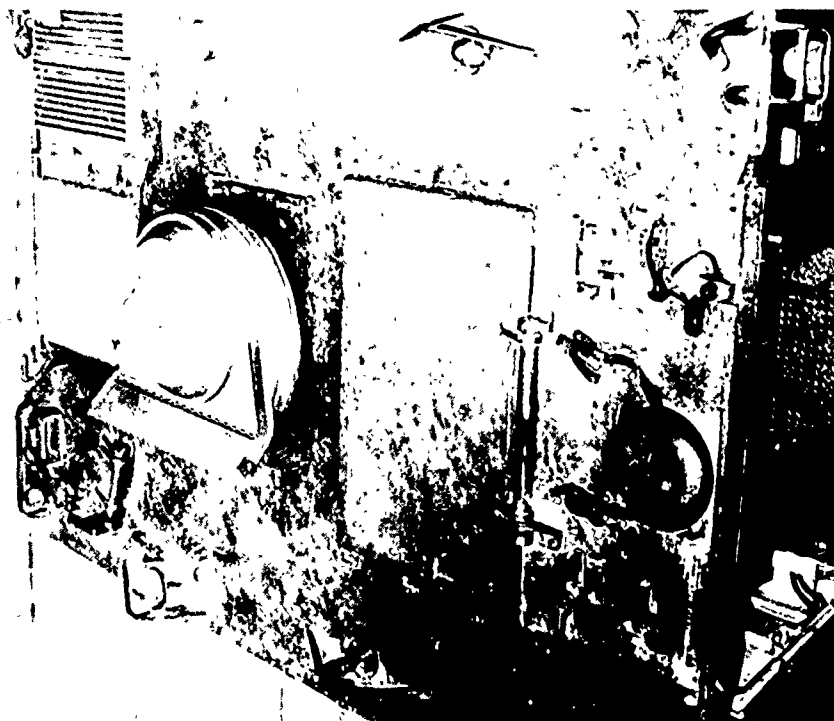


Figure 58. Exploded view of rapid scanning antenna system incorporating geodesic lens, line source horn, and cylindrical reflector.



(b) FORWARD LOOKING



(a) SIDE LOOKING

Figure 59. Armored personnel carrier with rapid scan geodesic lens antenna system showing two positions of lens boresight in its 360° sector.

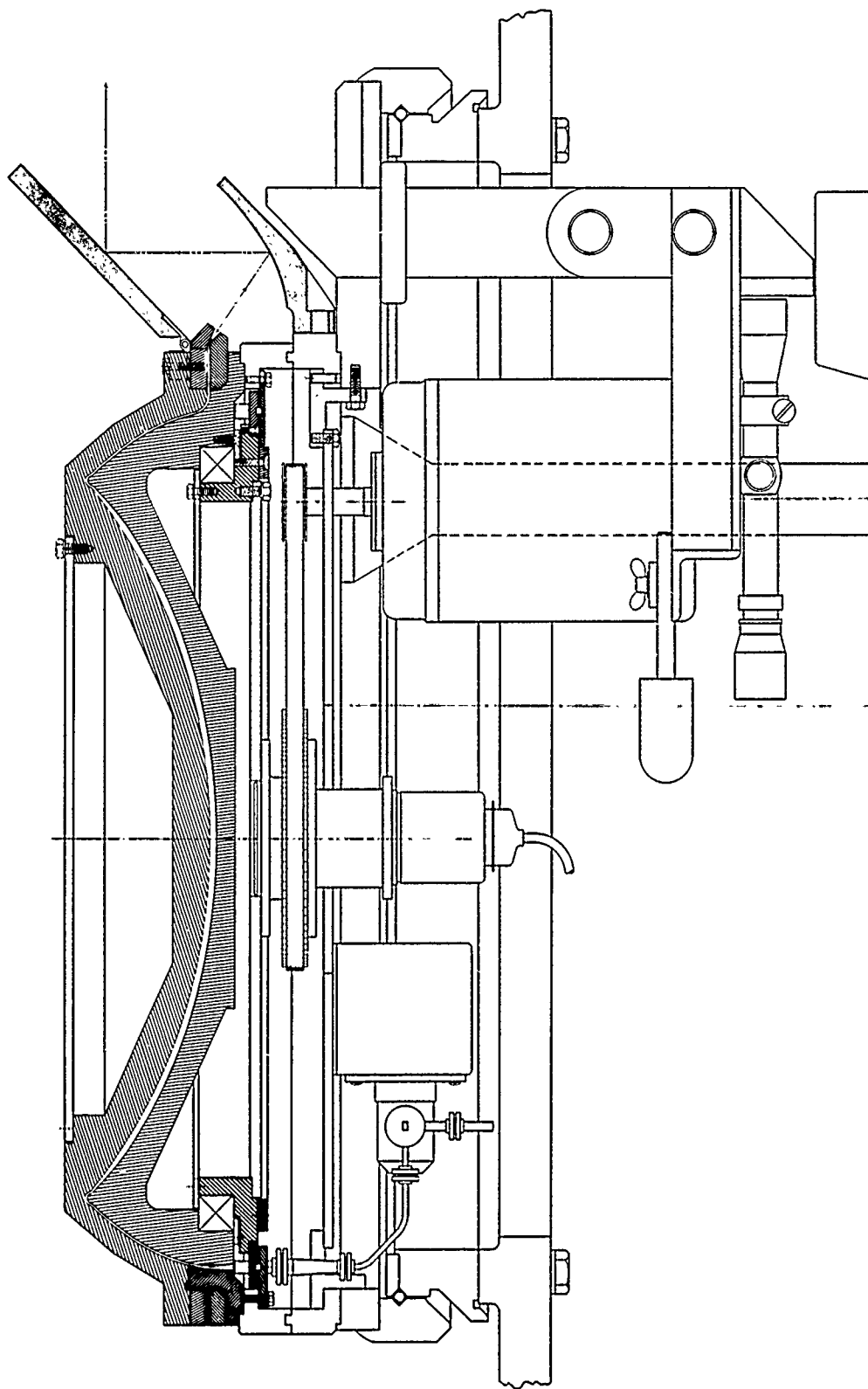


Figure 60. Central section through folded geodesic lens antenna system in 70 - GHz rapid scan radar.

parallel-plate extension to the lens output is curved back in gooseneck fashion, flared to form a line-source horn, and used as a feed for a parabolic cylinder. At millimeter wavelengths, such systems can scan as much as 150 beamwidths - more than an order of magnitude better than single-focal-point optical systems. As noted earlier, the geodesic lens only provides one-dimensional scan; however a scheme will be discussed which generates two-dimensional scan. A system having two plane scan was developed by EES for operation at 70 GHz [37] and installed in the armored personnel carrier shown in Figure 59. Criteria considered in the design of the system were a low-silhouette installation, rapid azimuth scan, adjustment of both the center of the azimuth sector and the elevation angle of the radar beam, and minimum blind area around the vehicle. The low-silhouette requirement dictated an antenna with only azimuth positioning capability, in addition to a new lens design. It was concluded that the best system for providing vertical collimation and beam-tilt adjustment in elevation consisted of a fixed parabolic cylinder illuminated by the line-source lens output horn. The cylinder reflector would then be positioned to direct the collimated $0.5^\circ \times 3.5^\circ$ beam vertically where it was then reflected forward by the tiltable plane reflector or splash plate (see the section through the lens in Figure (60)). The tilt of this secondary reflector, which can be adjusted by the operator, positions the beam in elevation; a 45° tilt of this reflector produces a 0° elevation angle of the beam. Tilting the splash plate by an amount θ scans the beam by an angle 2θ in elevation; consequently, the plate position would have to be dithered only $\pm 5^\circ$ to achieve a 20° scan sector.

It is proposed that a similar concept to that depicted in Figure 60 be utilized for the acquisition scanning antenna. The lens need not be folded for this application since lens height is not critical and folding does introduce a minor phase error in the aperture. As illustrated in Figure 56, the lens flat plate extensions flare at the same angle as the maximum azimuth scan angle ($\pm 22.5^\circ$) thereby increasing the aperture size by an additive factor of

$$D_s = D(\sec \theta + \tan \theta - 1) . \quad (129)$$

Then,

$$D_{\text{total}} = D + D_s = D(\sec \theta + \tan \theta) , \quad (130)$$

Where D is the aperture dimension required to give the desired beamwidth and θ is half the sector width. This flaring, however, ensures that the projected aperture and consequently the beamwidth remain constant as the beam scans. So long as the splash plate is large enough to intercept all of the collimated energy from the parabolic cylinder (even when tilted by an angle β), then the beamwidth will not vary with elevation scan. Table IX below presents a tabulation of calculated azimuth and elevation aperture dimensions (denoted a and b , respectively) needed to produce the beamwidths indicated at the frequencies listed. In this table, the gain and beamwidth are related to the wavelength and aperture dimension according to Equations (67) and (68). The elevation dimension was increased by 10% over the value needed at center of sector to compensate for its nodding motion in the cylinders field and the azimuth dimension was increased by the factor of Equation (129).

TABLE IX
CALCULATED APERTURE DIMENSIONS FOR A
TWO DIMENSIONAL SCANNER AS A
FUNCTION OF FREQUENCY, BEAMWIDTH, AND GAIN

Frequency (GHz)	Aperture Dimension (In.)	Beamwidth/Gain (Degrees/dBi)		
		0.75/47.3	1.0/44.8	1.25/42.8
9.3	a	164.6	123.5	98.8
	b	121	90.8	72.6
16.5	a	92.9	69.7	55.8
	b	68.3	51.2	41.0
23	a	74.3	50.1	40.0
	b	54.6	36.8	29.4
35	a	53.3	32.8	26.3
	b	39.2	24.1	19.3
46	a	35.0	25.0	20.0
	b	25.7	18.4	14.7
70	a	26.7	16.5	13.2
	b	19.6	12.1	9.7
95	a	17.6	12.1	9.7
	b	12.9	8.9	7.1

F. Rockwell Ferrite Scanner

The Rockwell International Corporation of Anaheim, California has developed a very lightweight electronically scanning antenna for use with a battlefield surveillance radar. The antenna is a planar array of slotted waveguides as shown in Figure 61. Each waveguide in this array is fed by a slot in another common waveguide which is oriented at 90° in space to the radiating guides. As energy propagates along the common or feeder waveguide, it is coupled out into the radiating guides which then distribute it to the slots. If the slot spacings in both the feeder and radiating waveguides are chosen judiciously, the energy over the entire array may be collimated so as to give a pencil beam along a given direction. The feeder waveguide contains a ferrite rod along its axis. A single solenoidal wire is wrapped around this feeder waveguide over the entire length so that the application of a DC voltage between the ends of the wire changes the phase delay per unit length of the waveguide. This means that the phase of the energy entering the radiating waveguides is a function of the amplitude of the ferrite drive voltage and that electronic elevation plane scanning can be achieved quite simply. This antenna has been built in the 10 GHz range with a weight on the order of two pounds using lightweight waveguide. The system suffers from the fact that it is inherently lower power than is needed for this application. Also, it is not known at this time whether the concept could be implemented at millimeter wavelengths due to fabrication tolerance considerations.

G. Other Electromechanical Techniques

The electromechanical technique which is felt to be optimum (i.e., geodesic lens with splash plate) has already been presented; however, it is felt that certain other electromechanical schemes warrant discussion.

The rapid scanning (in azimuth) generated by a single beam antenna whose entire structure is rotated rapidly can cover the required azimuth sector and provide the desired gain. The elevation sector coverage presents quite a problem to this design, however. Two dimensional scanning could be achieved by scanning the beam in elevation at a much faster rate than the azimuth rate. The result is a raster scan format with the beam moving from top to bottom instead of from side to side. Such high-speed elevation plane scanning can be achieved through the use of an organ pipe scanner

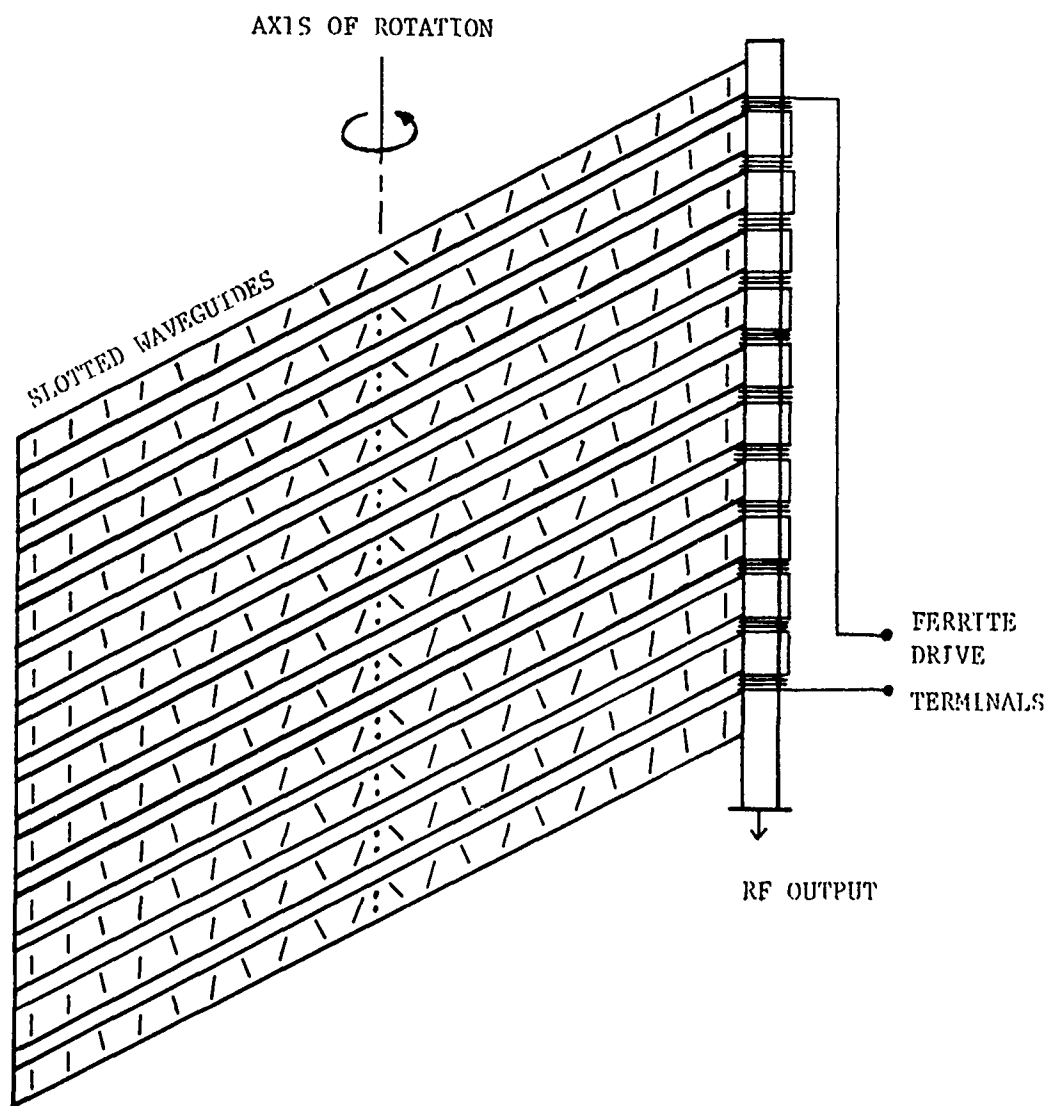
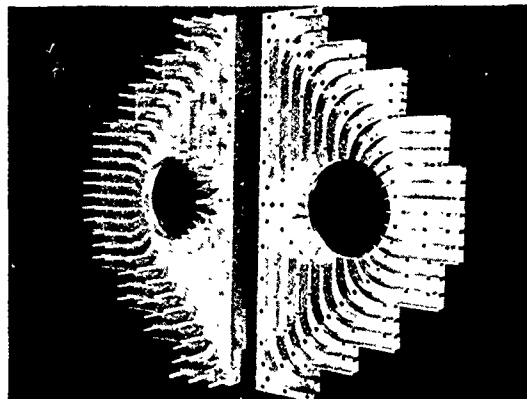


Figure 61. Simplified diagram of Rockwell ferrite scanner.

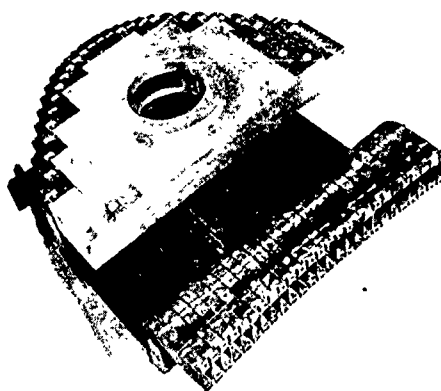
(see Figure 62) which effectively converts the rotational motion of a feed-horn to the linear movement of a phase center across the output horns of the organ pipe. The difficulty arises from the fact that reflector type antennas can be scanned only about ± 4 beamwidths about their focal points before pattern degradation occurs, whereas the present application requires about 20 beamwidths.

The high-speed azimuth rotation of several back-to-back antennas with each pointing at a progressively higher elevation angle produces the same raster format as does the lens/splash plate combination. This approach has two major difficulties: (1) the requirement for twenty beamwidths of elevation scan would dictate twenty separate antennas on a single pedestal and (2) a complex switching network would be required to switch between the different antennas.

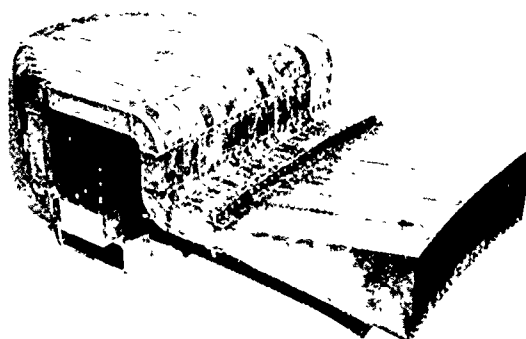
Another technique which is actually a combination of electromechanical and frequency scanning is depicted in Figure 63. Azimuth scan is achieved by a geodesic lens. The output of the lens is fed into an array of slotted vertical waveguides so that frequency shifting causes the pencil beam to scan in elevation. The difficulties associated with frequency scanning were discussed in Section V.A.4; consequently, designs incorporating this principle are not felt to be practical candidates.



(a) MILLED CENTRAL SECTION



(b) CENTRAL SECTIONS WITH INDIVIDUAL WAVEGUIDE CHANNELS



(c) ASSEMBLED SCANNER WITH OUTPUT HORNS

Figure 62. Progressive assembly levels for a typical waveguide organpipe scanner.

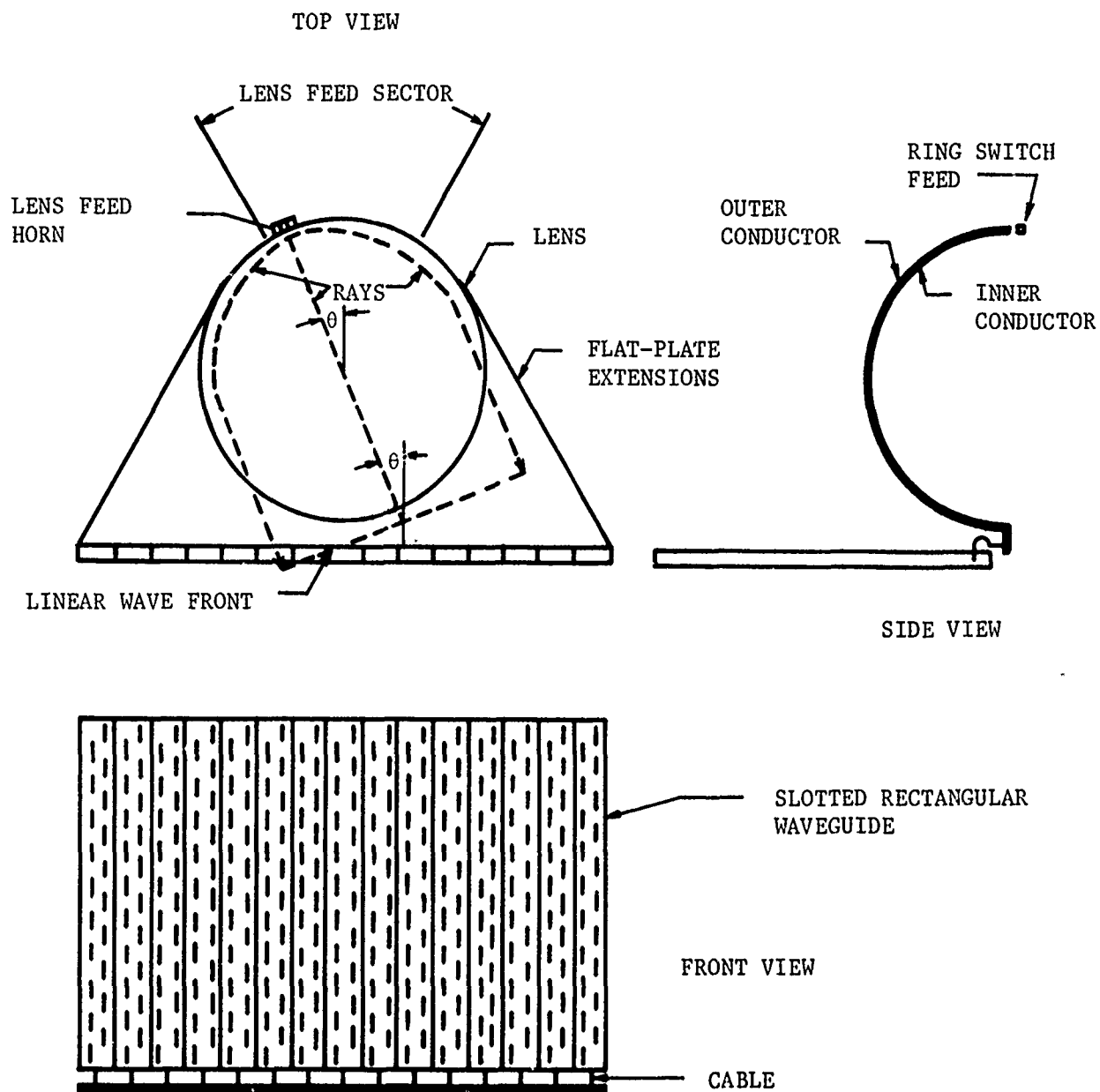


Figure 63. Three views of two dimensional scanner utilizing electromechanical scan in azimuth and frequency scan in elevation.

VI. CONCLUSIONS AND RECOMMENDATIONS

Under APL/JHU Subcontract 600444, the Engineering Experiment Station at Georgia Tech has performed a study for the Applied Physics Laboratory to determine the optimum acquisition antenna configuration for use in a naval short range point defense system. Frequencies having moderate atmospheric absorption properties (i.e., 23 and 46 GHz) were initially considered so as to afford some discrimination against long range standoff jammers. 23 GHz is near the first water vapor absorption line and 46 GHz is the next highest frequency having the same attenuation. Later in the program, several other frequencies including 9.3, 16.5, 35, 70, and 95 GHz were also considered.

It was felt that a more intelligent acquisition antenna selection could be made after several system parameters in this relatively unused portion of the spectrum were investigated. The total system factors which received attention included component availability, environmental effects (multipath, atmospheric absorption, rain attenuation), typical tracker capability, and threat characteristics.

The component survey indicated that high power sources are available over the entire range of frequencies considered; however, peak powers are considerably lower at 70 and 95 GHz than for the frequencies below 60 GHz. The survey also revealed that sufficient components are available to build a wide variety of radar systems at frequencies up through 46 GHz, although phase shifters are still development items at 46 GHz. The available power at 46 GHz is almost twice as great as at 23 GHz (125 kW and 65 kW, respectively) due simply to the fact that the proposed magnetron would be a modified version of a 35 GHz one where there has been considerable activity.

Multipath interference patterns were calculated for several combinations of frequency, wave height, and target height above water, and the results were presented in Figures 3 through 14. Basically, the multipath effect becomes less significant as either the frequency, wave height or target height is increased. The worst case cancellation, for either polarization, which occurs within an eight nautical mile range is listed below for a target height of 50 feet, an rms wave height of 1 foot, and several frequencies of interest.

<u>Frequency (GHz)</u>	<u>Maximum Cancellation Within 8 nmi. (dB)</u>
9.3	10.53
16.5	6.96
23	6.35
35	5.07
46	3.68
70	2.15
95	1.41

It should be noted that these cancellation values actually correspond to one-way antenna gain losses and that significant gain reinforcements are likely at other ranges. Also, it is emphasized that these calculations represent a worst case condition since there is evidence that the scattered signal is similar to incoherent noise and that the dielectric constant of the water decreases at the smaller wavelengths thereby reducing the magnitude of the interference signal.

The absorption analysis validated the known facts that a peak water attenuation occurred near 23 GHz, the more severe oxygen attenuation covers the region around 60 GHz and absorption windows exist in the three areas about these two regions. Both 23 and 46 GHz suffer attenuation between 0.1 and 0.2 dB/km one way depending on the relative humidity.

The effect of rain attenuation on the antenna design was also noted. After noting the results of several measurement programs, the theoretical attenuation curves by Goldstein [7] were chosen as representative and used across the band 9.3 to 95 GHz for uniformity. As is well known, the rain attenuation increases with increasing frequency and rain rate, and this is one of the major differences between 23 and 46 GHz.

A brief system study was performed to specify the requirements on the acquisition antenna. A 45° azimuth scan sector was taken as a strict requirement from the beginning, and a 20° elevation sector was found to be sufficient for all threat targets. Certain threats may achieve elevation angles as high as 45°; however, they do so at ranges where track must already have been initiated anyway. It is therefore necessary that the associated tracker be able to cover a window which is 45° wide in both

azimuth and elevation. It was found during the system study that handoff between acquisition and track should occur at a range of about 4 nmi. The desire to place 5 or 6 pulses on the target per beamwidth and also to see the target on 5 or 6 different scans of the beam lead to the requirement that the acquisition antenna provide sufficient gain to detect a target at a range between 6 and 8 nautical miles depending on the beamwidth chosen. The larger beamwidths require smaller window scan times and therefore smaller acquisition ranges but do not afford sufficient gain. A beamwidth on the order of 1° is felt to be optimum since values smaller than this require extraordinarily long acquisition ranges (see Figure 25).

The effect of rain attenuation at several frequencies was determined by calculating the gain required to produce a 12-dB signal-to-noise ratio as a function of target range for both a clear day and moderate (4 mm/hr.) rain. It was found that rain attenuation places unreasonable gain requirements on systems operating above 16.5 GHz. The question which must then be answered is: "Is one willing to accept severely limited system performance in rain so as to utilize a frequency which provides jammer protection and corresponds to small antenna dimensions?" If the answer is affirmative, since rain occurs only a small percentage of the time, then 46 GHz is recommended as the operating frequency since it provides clear-weather performance equal to that of 23 GHz while requiring only one-fourth the aperture area. The signal-to-noise ratio for a 46 GHz system having a 1° beam (44.8 dBi gain) was evaluated as a function of target range and is shown in Figure 64 for both a clear day and moderate rain.

Several different antenna concepts were considered for this application. These concepts were discussed in detail in Section V, and those discussions will be summarized here.

The beam scanning which results from varying the operating frequency of a leaky wave type radiator was investigated. The radiators investigated included continuous slots in both circular and rectangular waveguide and discrete slots in both straight and meandered rectangular waveguide. For the continuous slot case, it was found that for a given radiator type (i.e., WR-28 waveguide) one has little or not control over the scan sector location and that the scan sector widths obtainable over a reasonable

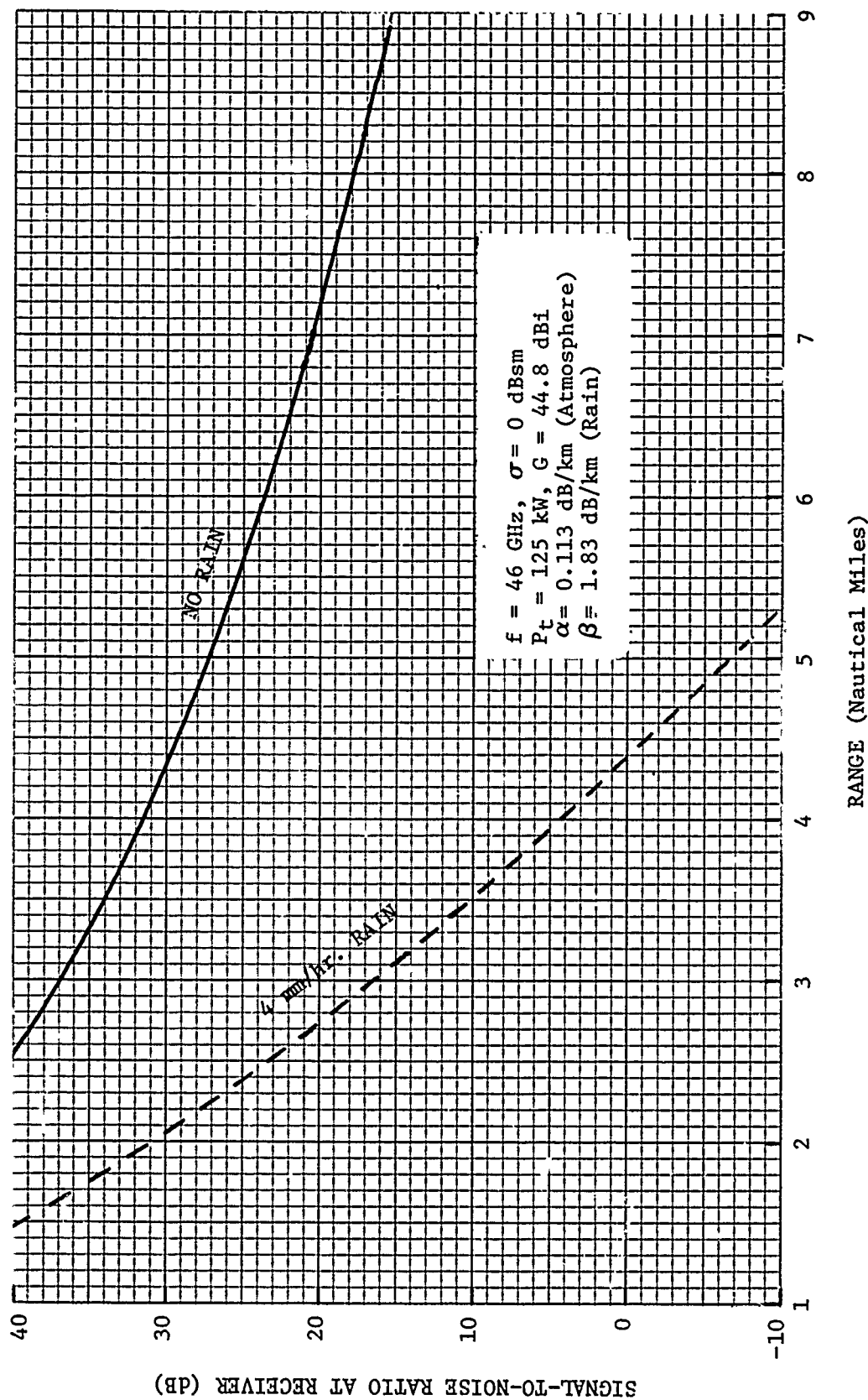


Figure 64. Calculated signal-to-noise ratio at the receiver for a 46 GHz radar illuminating a 1 square meter target at the range indicated. Radar antenna has a 1° beamwidth (Gain = 44.8 dBi).

bandwidth are not sufficient for this application. In the discrete slot case, one has control over the sector location through slot spacing but the sector size is still too small. The meander line radiator does allow one to trade frequency excursion for radiator complexity and hence obtain large scan sectors. Bandwidth is not a meaningful measure for frequency scanning systems since a frequency choice automatically connotes a beam pointing angle. A more basic problem is the total system required to accompany the antenna. Electromechanical methods for rapidly controlling magnetron frequencies are clumsy and inaccurate while millimeter-wave TWT's (for amplifying a number of low power discrete frequencies) are expensive and short lived. Frequency scanning techniques were then disregarded.

Several aspects of electronic phased arrays were then considered, and it was found that at least one design had merit at 23 GHz. The concept was an electronically steerable line source feeding a parabolic cylinder whose beam points vertically. This beam is then redirected by a planar 45° nodding splash plate. The beam is scanned electronically in azimuth while it is deflected in elevation by an angle which is twice the angular deviation from 45° of the splash plate. This concept is felt to be feasible at 23 but not at 46 GHz due to a lack of component development there. In particular, phase shifter switching time at 46 is approximately twenty times that at 23 GHz. The array bandwidth is of course a function of bandwidth of the components used. Some components can be as broadband as the basic waveguide while others such as dipole radiation can be as narrowband as 2%.

Multiple beam forming networks were considered but were found to be cost prohibitive. The reason for this is that they provide capability which is not needed, namely the ability to look along several directions at once. Multiple beam forming networks can be quite broadband but are susceptible to the same element limitations as the phased array.

Two lens, the Rotman and the geodesic Luneberg, were also considered. These two devices actually can be considered to be multiple beam forming networks since they produce a focused scanned beam for each input. They are more attractive than their electronic counterparts since they achieve collimation purely through transmission line path equalization as opposed to hybrids and phase shifters. The Rotman lens is constructed wholly

from flat paralalled plate and coaxial cable, while the geodesic is a non-planar surface of revolution in parallel plate media. The use of coaxial cables makes the Rotman unattractive at millimeter wavelengths whereas the geodesic has been successfully implemented at 70 GHz and is extremely broadband. The concept recommended is a geodesic lens/ring switch feeding a parabolic cylinder pointing vertically and a planar splash plate which nods about 45° (see Figure 65). The ring switch scan speed (azimuth) would need to be 23 Hz while the plate nodding rate should be 0.67 Hz to be commensurate with the maximum range, 1° beam, and time on the fastest target. Table IX shows that such an antenna concept would require a projected aperture of 25 by 18.4 inches in azimuth and elevation, respectively. A flat plate having these projected dimensions could be nodded in elevation quite easily by either hydraulic or electromechanical means.

Three other electromechanical schemes were given brief consideration, but the wide scan sectors in both plane precluded them. A novel ferrite scanner was also discussed, but it is not applicable at the required frequency and power levels.

A detailed engineering design must be performed before an accurate cost estimate can be made; however, based on experience with previous similar systems, it is felt that the recommended antenna would have a first time development cost (exclusive of basic engineering design and stationary platform) of approximately \$150,000 and a large quantity per item cost of \$60,000. The corresponding costs for a 23 GHz line source phased array feeding the parabolic cylinder and splash plate would be very close to the lens configuration. A cost estimate was not formulated for a 46 GHz phased array or the other designs discussed in this report since they are not practical candidates.

It is strongly recommended that a detailed engineering design be performed for the recommended concept. Such a design should include the lens surface, ring switch feed, azimuth and elevation drive concepts, structural design commensurate with shipboard operation, and environmental protection. It is particularly important that the nodding mechanism and

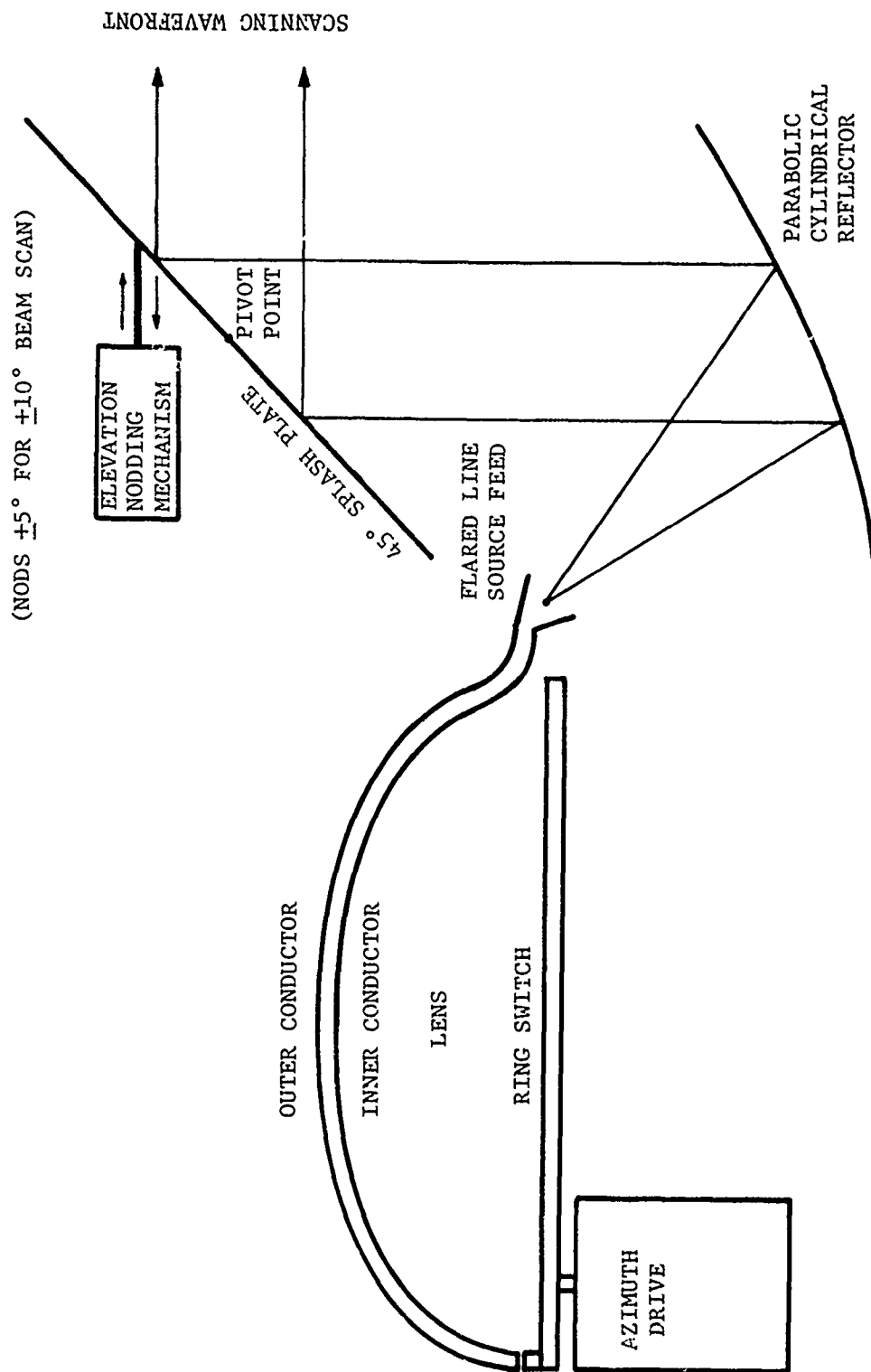


Figure 65. Elevation section of recommended antenna concept.

plate not be subjected to high winds; therefore, a strong radome is recommended. Due to the low angle nature of the threat, a stationary platform is also needed and should receive attention.

REFERENCES

1. R. J. Schmelzer, "Total Molecular Absorption in the Atmosphere from Frequencies below 380 kmc," LMSC Report No. 895084; March 1961. AD 256896.
2. R. D. Hayes "Total Atmospheric Attenuation at Millimeter Wavelengths," Doctoral Thesis, Georgia Institute of Technology, June 1964.
3. M. L. Meeks, "Atmospheric Emission and Opacity of Millimeter Wavelengths Due to Oxygen," Journal of Geophysical Research, Vol. 66, p. 3749; November 1961.
4. H. H. Theissing and P. J. Caplan, "Atmospheric Attenuation of Solar Millimeter Wave Radiation," Journal of Applied Physics, Vol. 27, p. 538; May 1956.
5. S. J. Dudzinsky, Jr., "Atmospheric Effects On Terrestrial MM-Wave Communications," Microwave Journal, December 1975, pp. 39-56.
6. J. W. and D. Ryde, "Attenuation of Centimetre and Millimetre Waves By Rain, Hail, Fog, and Clouds," GEC Report No. 8670, May 1945.
7. H. Goldstein, "Attenuation By Condensed Water," Propagation of Short Radio Waves, M.I.T. Radiation Laboratory Series, published by Boston Technical Publishers, 1964, Chapter 8, pp. 671-692.
8. "Multi-Environment Active RF Seeker (MARFS) For Helicopter Fire and Forget," Phase I Final Report, Martin Marietta Corporation, Report No. OR 14049, January 1976.
9. J. de Bettencourt, Appendix to Raytheon internal report (title unknown), April 1972.
10. K. L. Koester, L. Kosowsky, J. F. Sparacio, Appendices A,B,C to Norden Report (title unknown) to BRL, 7 August 1972. Based on data from Hogg, Crane, SRI, Kerr, and Ryde and Ryde. Appendices transmitted through private communications between Victor Richards, formerly of BRL, and R. D. Hayes of Georgia Tech.
11. Richards and Kammerer, "Rain Backscatter Measurements and Theory at Millimeter Wavelengths," BRL Report R1838, 1975.
12. N. C. Currie, F. B. Dyer, and R. D. Hayes, "Analysis of Radar Rain Return At Frequencies of 9.375, 35, 70, and 95 GHz," Final Technical Report on Contract DAAA-25-73-C-0256, Georgia Institute of Technology, February 1975, AD A007254.
13. C. A. Young, "Background Notes For Antenna Study" APL/JHU Internal Memo F30-75-236, 19 August 1975.

14. T. Tamir, "Leaky Wave Antennas," Antenna Theory, Part II, Edited by Collin and Zucker, McGraw Hill, New York, 1969, Chap. 20.
15. R. F. Harrington, "Propagation along a Slotted Cylinder," Journal of Applied Physics, Vol. 24, Number 11, November 1953, pp. 1366-1371.
16. N. A. Begovich, "Frequency Scanning," Microwave Scanning Antennas, Vol. III, edited by R. C. Hansen, Academic Press, New York, 1966, p. 138.
17. M. I. Skolnik, "Survey of Phased Array Accomplishments and Requirements for Navy Ships," Phased Array Antenna, ARTECH House, Inc., Dedham, Massachusetts, pp. 15-20, 1972.
18. J. F. Rippin, Jr., "Survey of Airborne Phased Array Antennas," Phased Array Antennas, ARTECH House, Inc., Dedham, Massachusetts, pp. 21-29, 1972.
19. W. H. Kummer and A. Kampinsky, "Phased Array Antennas for Applications on Spacecraft," Phased Array Antennas, ARTECH House, Inc., Dedham, Massachusetts, pp. 30-42, 1972.
20. H. Jasik, "Fundamentals of Antennas," Antenna Engineering Handbook, p. 2-26, 1961.
21. S. W. Lee and R. Mittra, "Radiation from a Dielectric-Loaded Waveguide," IEEE Transactions on Antennas and Propagation, AP-16, pp. 513-519, September 1968.
22. E. C. DuFort, "A Design Procedure for Matching Volumetrically Scanned Waveguide Arrays," Proceedings of the IEEE, Vol. 56, pp. 1851-1860, December 1968.
23. A. Hessel and H. Knittel, "A Loaded Ground Plane for the Elimination of Blindness in a Phased-Array Antenna," 1969 IEEE G-AP International Symposium Digest, pp. 163-169.
24. S. W. Lee and W. R. Jones, "On the Suppression of Radiation Nulls and Broadband Impedance Matching of Rectangular Waveguide Phased Arrays," IEEE Transactions on Antennas and Propagation, AP-19, pp. 41-51, January 1971.
25. J. Frank and J. Ruze, "Beam Steering Increments for a Phased Array," IEEE Transactions on Antennas and Propagation, pp. 820-821, November 1967.
26. B. R. Hatcher, "Granularity of Beam Positions in Digital Phased Arrays," Proceedings of the IEEE, Vol. 56, No. 11, November 1968.
27. W. H. Kummer, "Feeding and Phase Scanning," Microwave Scanning Antennas, edited by R. C. Hansen, Vol. III, Chapter 1, Academic Press, 1966.

28. B. R. Hatcher, "Collimation of Row-and-Column Steered Phased Arrays," Proceedings of the IEEE, Vol. 56, No. 11, November 1968.
29. J. Butler and R. Lowe, "Beam-Forming Matrix Simplifies Design of Electronically Scanned Antennas," Microwaves, pp. 170-173, April 1961.
30. J. Gobert, "A General Synthesis Procedure for Beam-Forming Matrices," Frequenz, pp. 364-367, December 1970.
31. H. J. Moody, "The Systematic Design of the Butler Matrix," IEEE Transactions on Antenna and Propagation, pp. 786-788, November 1964.
32. H. E. Foster and R. E. Hiatt, "Butler Network Extension to any Number of Antenna Ports," IEEE Transactions on Antennas and Propagation, pp. 818-820, November 1970.
33. W. Rotman and R. F. Turner, "Wide-Angle Microwave Lens for Line Source Applications," IEEE Transactions on Antennas and Propagation, pp. 623-632, November 1963.
34. D. Archer, "Lens-Fed Multiple-Beam Arrays," Microwave Journal, pp. 37-42, October 1975.
35. R. C. Johnson, "The Geodesic Luneberg Lens," Microwave Journal, Vol. 5, August 1962, p. 76.
36. R. C. Johnson, "Optical Scanners," Microwave Scanning Antennas, edited by R. C. Hansen, Vol. I, Academic Press, 1966.
37. R. M. Goodman, Jr. and F. B. Dyer, "Millimeter Wave Radar," Final Report on Contract DA-49-186-AMC-275(A), Georgia Institute of Technology, Atlanta, Georgia, 29 February 1968.

Unclassified

SECURITY CLASSIFICATION OF THIS PAGE (When Data Entered)

REPORT DOCUMENTATION PAGE		READ INSTRUCTIONS BEFORE COMPLETING FORM										
1. REPORT NUMBER	2. GOVT ACCESSION NO.	3. RECIPIENT'S CATALOG NUMBER										
4. TITLE (and Subtitle) Rapid-Scan Antenna Study for Naval Short-Range Self-Defense Missile System.		5. TYPE OF REPORT & PERIOD COVERED Final Technical Nov. 1975-April 1976										
		6. PERFORMING ORG. REPORT NUMBER EES/GIT A-1794-F										
7. AUTHOR(s) J. W. Cofer, Jr., R. M. Goodman, Jr., and L. D. Sikes		8. CONTRACT OR GRANT NUMBER(s) APL/JHU Subcontract 600444										
9. PERFORMING ORGANIZATION NAME AND ADDRESS Engineering Experiment Station Georgia Institute of Technology Atlanta, Georgia 30332		10. PROGRAM ELEMENT, PROJECT, TASK AREA & WORK UNIT NUMBERS										
11. CONTROLLING OFFICE NAME AND ADDRESS The Johns Hopkins University Applied Physics Laboratory Johns Hopkins Rd., Laurel, Maryland 20810		12. REPORT DATE April 1976										
		13. NUMBER OF PAGES 133 + xiii										
14. MONITORING AGENCY NAME & ADDRESS (if different from Controlling Office)		15. SECURITY CLASS. (of this report) Unclassified										
		15a. DECLASSIFICATION/DOWNGRADING SCHEDULE N/A										
16. DISTRIBUTION STATEMENT (of this Report) Approved for public release; distribution unlimited.												
17. DISTRIBUTION STATEMENT (of the abstract entered in Block 20, if different from Report)												
18. SUPPLEMENTARY NOTES												
19. KEY WORDS (Continue on reverse side if necessary and identify by block number) <table border="0"> <tr> <td>Millimeter-wave Components</td> <td>Geodesic Lenses</td> </tr> <tr> <td>Multipath Interference</td> <td>Frequency Scanning</td> </tr> <tr> <td>Atmospheric Absorption</td> <td>Multiple Beam Antennas</td> </tr> <tr> <td>Rain Attenuation</td> <td>Phased Arrays</td> </tr> <tr> <td>Millimeter-wave Scanning Antennas</td> <td>Millimeter-wave Signal/Noise</td> </tr> </table>			Millimeter-wave Components	Geodesic Lenses	Multipath Interference	Frequency Scanning	Atmospheric Absorption	Multiple Beam Antennas	Rain Attenuation	Phased Arrays	Millimeter-wave Scanning Antennas	Millimeter-wave Signal/Noise
Millimeter-wave Components	Geodesic Lenses											
Multipath Interference	Frequency Scanning											
Atmospheric Absorption	Multiple Beam Antennas											
Rain Attenuation	Phased Arrays											
Millimeter-wave Scanning Antennas	Millimeter-wave Signal/Noise											
20. ABSTRACT (Continue on reverse side if necessary and identify by block number) <p>Under APL/JHU Subcontract 600444, the Engineering Experiment Station at the Georgia Institute of Technology performed a conceptual study of millimeter-wave scanning antennas which might be applicable to the acquisition problem of a naval point defense system. The study covered such related areas as component availability, increased antenna requirements due to multipath, atmospheric absorption, and rain attenuation, and scan speed and format needed to acquire the targets of interest. Gain requirements were derived on the basis of acceptable signal-to-noise ratios at the desired range using</p>												

Unclassified

SECURITY CLASSIFICATION OF THIS PAGE(When Data Entered)

20. Abstract continued

commercially available power sources. Performance degradation due to rainfall was calculated at several frequencies between 9.3 and 95 GHz. 46 GHz was chosen as the operating frequency due to antenna size and signal-to-noise ratio. Several scanning antenna techniques including frequency scanning, electronic phased arrays, multiple beam forming networks, electromechanical techniques and several hybrid approaches were considered. An electromechanical technique utilizing a geodesic lens, line source feed, parabolic cylinder, and nodding planar splash plate was chosen as the optimum candidate due to the factors of component availability, cost, scan speed, and frequency of operation.